

Search for long-lived supersymmetry in final states with jets and missing energy in the CMS detector

Christian Laner Ogilvy
Imperial College London
Department of Physics

A thesis submitted to Imperial College London
for the degree of Doctor of Philosophy

Abstract

The abstract.

Declaration

Declaration. Say what I worked on.

Christian Laner

Acknowledgements

Thank you to everyone.

Contents

1. Introduction	1
2. Theory and motivation	2
2.1. The standard model of particle physics	2
2.1.1. Fundamental fermions	2
2.1.2. Fundamental bosons	3
2.2. Beyond the standard model	3
2.3. Dark matter	4
2.4. Supersymmetry	4
2.5. Exotic long-lived particles	5
2.5.1. Split supersymmetry	5
2.6. Simplified models	6
2.7. Status of searches for supersymmetry and long-lived particles . . .	6
3. Experimental setup	8
3.1. The Large Hadron Collider	8
3.2. The Compact Muon Solenoid	8
3.2.1. Tracker	9
3.2.2. Electromagnetic calorimeter	9
3.2.3. Hadronic calorimeter	9
3.2.4. Muon system	10
3.2.5. Magnet	10
3.2.6. Trigger and data acquisition	10
3.3. Event reconstruction	11
3.3.1. Tracks and vertices	11
3.3.2. Electrons and photons	11
3.3.3. Muons	11
3.3.4. Particle flow algorithm	12
3.3.5. Jets	12

3.3.6. Energy sums and missing energy	13
3.4. Simulation	13
4. Search strategy	14
4.1. Physics objects	16
4.2. Baseline selection	19
4.3. Standard model backgrounds	21
4.3.1. Electroweak processes	22
4.3.2. QCD processes	23
4.4. QCD background rejection	24
4.4.1. The α_T variable	25
4.4.2. The $\Delta\phi_{\min}^*$ variable	27
4.4.3. The \cancel{H}_T/E_T variable	28
4.5. Event selection	29
4.5.1. Signal region	30
4.5.2. Control regions	31
4.6. Event categorisation	33
4.7. Trigger	37
4.7.1. Signal and control region triggers	38
4.7.2. Trigger efficiency	40
4.8. Data sets and simulation samples	41
4.8.1. Data sets	43
4.8.2. Simulation samples	43
4.9. Corrections to simulation	45
4.9.1. Pileup	45
4.9.2. Jet energy	45
4.9.3. b-tagging	45
4.9.4. Lepton identification, isolation and triggering	47
4.9.5. Trigger	51
4.9.6. Theoretical calculation of V+jets production	51
4.9.7. Initial state radiation in $t\bar{t}$ events	52
4.9.8. Cross-sections	52
4.9.9. Statistical precision at large n_b	53
4.10. Estimation of electroweak background processes	55
4.10.1. The n_{jet}, n_b and H_T dimensions	55
4.10.2. The \cancel{H}_T dimension	57

4.11. Estimation of QCD background processes	58
4.12. Uncertainties on background estimation	60
4.12.1. Uncertainties derived from variations in simulation	62
4.12.2. Uncertainties derived from data-driven closure tests	67
4.12.3. Uncertainties on the \cancel{H}_T distribution	70
5. Results and interpretation	71
5.1. Characterisation of long-lived gluino models	71
5.2. Uncertainties on signal model simulation	72
5.3. Statistical model	75
5.4. Comparison of expected background and observed data	78
5.5. Procedure for setting limits on signal models	79
5.6. Limits on long-lived supersymmetry	83
6. Conclusion	90
A. Appendix: Search strategy	91
A.1. Uncertainties on transfer factors derived from variations in simulation	91
B. Appendix: Results and interpretation	101
B.1. Comparison of expected background and observed data	101
B.2. Results under likelihood fit to signal and control regions	109
B.3. Nuisance parameters	112
Bibliography	118
List of figures	121
List of tables	128

Chapter 1.

Introduction

Fancy introduction to particle physics, DM, SUSY, LLPs.

Dark matter is a hypothetical form of matter which constitutes about 27% of the total energy content of the universe [1]. Its nature is unknown and its presence has so far only been inferred indirectly through its gravitational effects. Large efforts by the astrophysical and particle physics communities are being made on searches for the elusive dark matter.

Mention previous results somewhere (haven't found SUSY/DM/BSM/anything new since Higgs boson).

First LL interpretation of search for prompt np /susy with no specific optics for LL. say why this is interesting/important (benchmark for future LL searches, see where sensitivity to LL currently lies - surprisingly already quite sensitive)

Chapter 2 will describe the theoretical foundations and motivations for this search. Chapter 3 will do bla, etc.

Chapter 2.

Theory and motivation

Some introductory paragraph. We will begin by looking at the SM. Then bla and finally bla. I wouldn't have so much SM math - brief intro to SM (each term in Lagrangian) and then move on to BSM (DM, SUSY, LL, simplified models, current limits). Theory and motivation (15%) (15 pages – 2 pages per bullet below)

2.1. The standard model of particle physics

3 pages. Brief intro to SM - see Marco-Andrea two pages. If have time/space/botheredness, mention SM Lagrangian and $SU_3 \times SU_2 \times U_1$. QED and QCD.

The Standard Model (SM) is a quantum field theory which describes the fundamental particles (quarks, leptons, gauge bosons and Higgs boson) and their interactions (electromagnetic, weak nuclear and strong nuclear). Fermions (half-integer spin, matter) and bosons (integer spin, force carriers).

SM particles summarised in Table. We will describe in the following subsections. Table summarising all SM particles with their mass and charge (Marco-Andrea, Adam, Nick).

2.1.1. Fundamental fermions

Quarks (6) and leptons (6), generations, charges, interactions.

2.1.2. Fundamental bosons

Quanta of gauge fields. Mediators of em, weak, strong interactions. Describe each interaction in turn. Gravity not included in SM. Ranges. Which particles feel each force.

Electroweak symmetry breaking. Higgs boson (scalar, spin 0). Discovered in 2012 (final piece of SM).

2.2. Beyond the standard model

1.5 pages. Problems with the standard model. Tapper slides. MA and AE.

The SM has been well tested experimentally and has been found to describe very accurately a wide range of physical phenomena. However, it does not incorporate the gravitational force, account for neutrino oscillations or explain the matter-antimatter asymmetry in the universe. There are also theoretical concerns about the lack of unification of forces at the Grand Unified Theory (GUT) scale as well as the hierarchy problem, whereby higher order loop corrections to the mass of the Higgs boson lead to a divergence in its mass unless a large amount of 'un-natural' fine tuning is introduced. Finally, and most relevant to this discussion, no particle in the SM is a viable candidate for dark matter. The SM is therefore thought to be an effective theory which is only valid at low energies and a more complete model at larger energy scales must exist. Gravitational force, Planck scale

Neutrino masses

Dark matter. Makes up large proportion of universe. Lots of evidence. No particle in SM is DM candidate. Discussed in more detail in Sec. 2.3. Or if chapter ends up being too long summarise and merge that section into here (maybe make a subsection)

Higgs mass/hierarchy problem

Gauge coupling unification

Matter-antimatter asymmetry

2.3. Dark matter

DELETE - DARK MATTER NO LONGER IN THESIS.

1-1.5 pages. More details on DM (evidence, WIMP miracle, cosmology) (borrow from my reports)

Evidence – see my report.

The most favoured DM candidate is a non-baryonic, weakly interacting massive particle (WIMP) which is stable and electrically neutral [8]. WIMPs fall into the category of cold dark matter, meaning that they were non-relativistic at the time of freeze-out and hence lead to the large scale structures observed in the universe today. Their weak interaction cross section also results in the correct relic abundance required to explain the present dark matter content of the universe (the “WIMP miracle”).

Searching for DM (report): DD, ID, collider (complimentary).

2.4. Supersymmetry

1.5-2 pages. SUSY theory (borrow from RA1/kostas theses and RA1 papers). MA and AE.

Poincare group, additional symmetry between bosons and fermions. Broken symmetry. Solves hierarchy problem, unification, DM.

MSSM is simplest version of SUSY (minimal particles). 105 parameters. Table of MSSM particles (MA). R-parity. Relationship with DM – LSP/neutralino is DM candidate. stop naturalness?

A theoretically well motivated extension to the Standard Model is supersymmetry (SUSY) [6, 7], which introduces a new spacetime symmetry between fermions and bosons. Essentially, for every fundamental particle there exists a supersymmetric partner with spin differing by $\frac{1}{2}$. Fermions and bosons enter the mass correction calculation of the Higgs boson with opposite signs, so if the mass difference between SM particles and their superpartners is not too large (ab 1 TeV), an incomplete cancellation between the two leads to the naturally small Higgs boson mass. Thus,

supersymmetry can provide a solution to the hierarchy problem of the Standard Model. Furthermore, the strong, weak and electromagnetic couplings are found to converge at the GUT scale, thus providing a solution to the unification problem as well. Finally, most supersymmetric theories predict a particle candidate for dark matter, as explained in the next section.

R-parity is a quantity defined such that Standard Model and supersymmetric particles are assigned $PR = +1$ and $PR = -1$, respectively. If R-parity is conserved, the lightest supersymmetric particle (LSP) cannot decay and thus is stable. If it is neutral, this LSP satisfies the WIMP criteria. The LSP is usually assumed to be the neutralino, a superposition of the superpartners of the Higgs boson and gauge bosons. Other dark matter candidates include the axion and the lightest Kaluza-Klein particle (LKP) arising from solutions to the strong CP problem and theories of extra spatial dimensions, respectively.

2.5. Exotic long-lived particles

1 page.

Many BSM theories predict long-lived particles. There are examples in the SM (give examples). They travel some distance before decaying. Could be within or outside the detector. Decay length follows an exponential distribution (give pdf). define τ . Width is inverse of lifetime.

Briefly describe MSSM (NLSP), GMSB, hidden valleys, RPV SUSY.

slide 2: • RPV SUSY • Stealth SUSY • Split SUSY • WIMP Baryogenesis • Neutral Naturalness • Axions • Right Handed Neutrinos • Many more...

DMLL useful presentation (eg slide 11)

2.5.1. Split supersymmetry

LLP thesis 4.2.4 and paper. SUSY broken near unification scale. Squarks decoupled to very high scale. Gluinos are long-lived. Coloured. Must decay via highly virtual squarks. Lifetime larger than hadronisation scale (ps?). Gluinos form R-hadrons

(so-called because of non-trivial R-parity) (can be mesons, baryons or gluinoballs).
Can change charge through nuclear interactions.

2.6. Simplified models

1.5 pages. Motivation for simplified models (see 3 reasons in OB LLDM, too many parameters in MSSM. CMSSM not model-independent).

General SUSY signature at LHC: Pair production, strong interaction dominant at LHC (squarks and gluinos), decay to SM particles and LSP, large mass hence large MET (briefly describe MET - momentum imbalance due to LSP not being detected).

Only one decay considered, other particles at much higher scale.

These are the simplified models that are used in this thesis to interpret the results in this thesis.

3 params: two masses and lifetime. The long-lived particle's lifetime is a parameter of the model. Consider life distances (lifetimes) from $c\tau = 1 \text{ um}$ ($\tau = x \text{ ns}$) to 100 m ($\tau = y \text{ ns}$), plus prompt and stable.

T1qqqq and T1qqqqLL (split SUSY): here consider (long-lived) gluino pair production, each decays to two (light) quarks and an LSP. As gluino lifetime goes to 0 recover prompt model.

Interaction of R-hadron with detector material not simulated (won't have an effect on our analysis/not the purpose of our analysis – see paper). If necessary, describe cloud model, and percentages of gluinoball etc (and/or describe in simulation section).

Feynman diagram of T1qqqqLL

2.7. Status of searches for supersymmetry and long-lived particles

Current DM/SUSY limits (CMS/ATLAS and briefly compare to DD, mention X GeV limits on mediator/DM/gluino/LSP), very constrained hence look for LL

signatures, we think we've excluded X GeV gluinos but that's not true if they're LL. Mono-X but monojet strongest constraints.

Current LL limits (CMS/ATLAS). Many possible types of striking signatures – displaced leptons/photons/jets, disappearing/kinked tracks, stopped particles, etc. Not many with MET, first LL interpretation of prompt analysis (as long as decays within tracker can still reconstruct with standard algorithms, plus ISR), briefly mention complementarity (sensitive to whole range of lifetime, sub-cm and all mass splittings).

see llp thesis and workshop

LL: see paper (refs 36-46).

Chapter 3.

Experimental setup

20-25 pages. Intro to chapter.

3.1. The Large Hadron Collider

CERN and LHC. Franco-Swiss border. 26 km. x km underground. Largest and most powerful. Collider physics. Luminosity (instantaneous/integrated) and cross section formulas (Marco-Andrea/Pesaresi). Used to search for new physics and discover Higgs boson. Need very high energy to produce high mass particles and search for new physics (cf \sqrt{s} vs $\sqrt{s_{\text{com}}}$). (Compare to ep collider and fixed target). Proton-proton (and ion) collisions. Bunch spacing, number of bunches, number of protons per bunch (Marco-Andrea table). ATLAS, CMS, LHCb, ALICE. Accelerator complex: hydrogen, LINAC, PS, SPS, etc (show diagram). Centre of mass energy. Pileup (formula/estimate using inelastic \sqrt{s} ?). Minimum bias.

Diagram of accelerator complex.

History of Run1, shutdown, Run 2. Amount of data delivered.

Describe run, fill, lumi section, instantaneous luminosity values.

3.2. The Compact Muon Solenoid

One of two multipurpose detectors. Used to search for new physics and discover Higgs boson.

Hermetic coverage. Overview of subdetectors. Magnet strength.

Diagram.

Coordinate system. Pseudorapidity.

3.2.1. Tracker

How tracker works, ie electron-hole pairs (see Adam and MSci report). High radiation environment. Little material.

Pixel tracker.

Silicon strip tracker.

TOB, TEC, etc. Their positions/extents.

Diagram of layout.

Momentum resolution, tracking efficiency, spatial resolution.

3.2.2. Electromagnetic calorimeter

Designed to detect electrons and photons. Lead tungstate crystals.

EB. EE. Preshower.

Diagram of layout.

How ECAL works (ECAL shower, bremsstrahlung and pair production - see Adam and APP MSci course.)

Resolution formula $(a+b+c)$.

3.2.3. Hadronic calorimeter

Designed to detect hadrons/jets. Brass and scintillating plastic. Photodiodes. HF. Fibres.

HB. HE. HO. HF

Diagram of layout.

How HCAL works (hadronic showers produce scintillation light - see Adam and APP MSci course.)

Resolution formula.

3.2.4. Muon system

Adam: As muons are heavier than electrons, they are minimally ionising and lose little energy through bremsstrahlung. They therefore mostly pass through the ECAL and HCAL. As muons are a key component of many electroweak decays, CMS has a dedicated muon system interleaved with the iron return yoke surrounding the solenoid.

DT (MB), CSC (ME), RPC.

Diagram of layout.

Momentum resolution 1%.

3.2.5. Magnet

Just one or two short paragraphs. See Marco-Andrea, Citron, Baber.

3.2.6. Trigger and data acquisition

40 MHz.

L1 trigger.

HLT.

Computing tiers.

L1 trigger upgrade and my service work?

Not sure yet. Look at Adam, Matt, Jad.

3.3. Event reconstruction

Intro: need to put together the things observed in the detector to reconstruct the objects.

Object reconstruction/identification (requires revision). Tag and probe. vertexing/tracking, btagging, PF, antikt. PU subtraction, isolation, cross-cleaning. MC corrections (JECs, PU, btagging, lepton ID, etc.).

Mention objects/working points used in analysis as you go along. Maybe summary table like Matt. Actually maybe include this in analysis chapter (see Adam).

3.3.1. Tracks and vertices

Combinatorial track finder (CTF), Kalman filter.

Primary vertex. PU vertices. Secondary/displaced vertices (b quarks) found in subsequent levels of reconstruction.

Efficiencies.

Isolated tracks? (when talking about analysis objects).

3.3.2. Electrons and photons

3.3.3. Muons

Global and tracker muons.

Define relative and mini-isolation. Define pileup subtraction - effective rho area, delta beta? (have a dedicate section like adam)

$\rho \cdot A_{\text{eff}}$, where ρ is the median of the transverse energy density per unit area in the event [26] and A_{eff} is the area of the isolation region weighted by a factor that takes into account the dependence of the pileup transverse energy density on pseudorapidity. The effective areas have been determined in gamma + jet events.

3.3.4. Particle flow algorithm

Need to decide where to put this. Not clear on the connection between object reconstruction and particle flow. Resources: Particle Flow paper, Particle Flow summary.

The tracks are extrapolated through the calorimeters, if they fall within the boundaries of one or several clusters, the clusters are associated to the track. The set of track and cluster(s) constitute a charged hadron and the building bricks are not considered anymore in the rest of the algorithm. The muons are identified beforehand so that their track does not give rise to a charged hadron. The electrons are more difficult to deal with. Indeed, due to the frequent Bremsstrahlung photon emission, a specific track reconstruction [3] is needed as well as a dedicated treatment to properly attach the photon clusters to the electron and avoid energy double counting. Once all the tracks are treated, the remaining clusters result in photons in case of the electromagnetic calorimeter (ECAL) and neutral hadrons in the hadron calorimeter (HCAL). Once all the deposits

3.3.5. Jets

Briefly describe what a jet is (hadronisation, tight cone of particles [MA]). antikt algorithm. Infrared and collinear safe. Inputs are PF candidates. Pileup subtraction (not just here but for all objects).

Correcting the energy of jets

JECs. JER?

b-tagging

Identification of jets originating from bottom quarks.

see btagging CMSDAS Introduction.pdf eg slide 11 how eff varies with pt and eta, ROC curves, etc.

3.3.6. Energy sums and missing energy

Define HT, MHT and MET. At some point (maybe near the beginning) explain why we use the transverse plane (initial momentum is zero, whereas it isn't in the longitudinal plane).

Neutrinos do not interact in particle detectors, and therefore escape undetected. Their presence can be inferred by the momentum imbalance of the visible particles in an event. (this should be mentioned in overview of analysis in intro chapter).

Type-1 corrections.

3.4. Simulation

MADGRAPH5 [1] POWHEG [2] PYTHIA8 [3] GEANT4 [4]

Chapter 4.

Search strategy

This chapter describes the analysis strategy of a search for physics beyond the standard model in proton-proton collisions at a centre of mass energy of 13 TeV. The search is performed in final states containing missing transverse momentum and at least one jet.

The search is designed to have sensitivity to a wide range of new physics models that involve the production of a weakly interacting particle (WIMP), such as dark matter or the lightest supersymmetric particle. The search has been optimised for signatures in which the WIMP is produced from prompt decays at the primary collision vertex. However, as will be discussed in Chap. 5, the search is also sensitive to signatures in which the WIMP is produced at a displaced vertex following the decay of a long-lived particle.

In the proton-proton collisions, the net momentum of the colliding partons in the plane transverse to the beam direction is effectively zero, whereas the longitudinal momentum is not necessarily so. In order to conserve momentum, the outgoing particles produced in the collision must therefore have an overall transverse momentum of zero. As WIMPs do not interact with the detector material, the measured net transverse momentum in the event will be non-zero. This non-zero “missing transverse momentum” is the key signature of such particles. In addition, at a hadron collider such as the LHC, the dominant production is via the strong interaction, and hence jets are readily produced either in association with the WIMP, or as initial or final state radiation (ISR, FSR). For these two reasons the search is performed in final states containing jets and missing energy. The requirement of at least one jet is needed for the missing momentum to be defined and for the event to

be triggered. A hadronic final state is ensured by vetoing events containing leptons or photons.

A missing energy signature is not unique to WIMPs, however, and is also present in certain standard model processes. Neutrinos (produced in the decays of Z and W bosons, for example) are also weakly interacting and undetectable at CMS. It is also possible for particles to be over or under-measured, thereby introducing a “fake” momentum imbalance. This type of background arising from energy mis-measurements is suppressed as much as possible (to $<1\%$ of the total background) using dedicated variables. The remaining standard model background (that involving neutrinos) must be estimated as precisely as possible, using a combination of theory calculations, simulation, and calibrations in data. One can then look for a statistically significant excess in the data above the expected amount of standard model background that would be an indication of physics beyond the standard model.

In order to maximise the sensitivity to a wide range of BSM physics scenarios, all of which may manifest themselves in topologically slightly different ways in the detector, the candidate signal events (which form part of the *signal region*) are categorised according to four variables: the total jet energy, the missing jet energy, the number of jets, and the number of b-tagged jets. Two *control regions* are defined, labelled $\mu + \text{jets}$ and $\mu\mu + \text{jets}$, that are analogous to the signal region but are enriched by selection of muons in the W and Z background processes, respectively, and are employed in the background estimation.

Similar searches for supersymmetry have been performed in Runs 1 and 2 of the LHC, at centre of mass energies of 7, 8 and 13 TeV, and for a range of integrated luminosities. These can be found in Refs. [5–9]. These searches are used as a basis for the analysis described in this thesis, which uses 13.9 fb^{-1} of data at $\sqrt{s} = 13 \text{ TeV}$. A series of developments and optimisations have been made in order to adapt the analysis for the higher centre of mass energy and larger amount of data collected. In addition, the interpretation in the context of long-lived particles is a novelty to this search.

4.1. Physics objects

This section provides the definitions of the various physics objects employed in the search. Each object is reconstructed using the algorithms described in Sec. 3.3, and each algorithm has parameters that can be tuned in order to provide a desired balance between identification efficiency and fake rate. Jets and energy sums form a key component in the search and are required in both the signal and control regions. Electrons, photons and isolated tracks are vetoed in both the signal and regions. Muons are vetoed in the signal region and are required in the control regions. A summary of the kinematic requirements discussed in this section on these physics objects is provided in Tab. 4.1.

Object	Selection or veto	p_T (> GeV)	$ \eta $ (<)
Jet	Selection (signal and control regions)	40	2.4
Muon	Selection (control region)	30	2.1
	Veto (signal region)	10	2.4
Electron	Veto (signal and control regions)	10	2.4
Photon	Veto (signal and control regions)	25	2.4
Isolated track	Veto (signal and control regions)	10	2.4

Table 4.1.: The p_T and η thresholds for physics objects that are used to either select events or veto them.

Jets

Jets are reconstructed by clustering Particle Flow candidates using the anti- k_T algorithm with a distance parameter of 0.4. Charged PF candidates that originate from pileup vertices are not included. The four-momentum of a jet is defined to be the vector sum of the four-momenta of all clustered constituents. Corrections to the energies of the resulting jets are applied as described in Sec. 3.3.5.

Several loose requirements on the jet constituents are imposed in order to avoid spurious jets originating from noise in the calorimeters. These requirements include a minimum number of charged constituents and a minimum fraction of the jet energy attributed to charged hadrons, as well as an upper bound on neutral hadron, photon, and electron contributions. The requirements are summarised in Tab. 4.2.

Table 4.2.: Quality requirements imposed on the constituents of jets.

Variable	Requirement	
$ \eta < 3$		
Neutral hadron energy fraction	< 0.99	
Neutral electromagnetic energy fraction	< 0.99	
Number of constituents	> 1	
Charged hadron energy fraction	> 0	(only for $ \eta < 2.4$)
Charged electromagnetic energy fraction	< 0.99	(only for $ \eta < 2.4$)
Number of charged constituents	> 0	(only for $ \eta < 2.4$)
$ \eta > 3.0$		
Neutral electromagnetic energy fraction	< 0.90	
Number of neutral constituents	> 10	

Jets in the event are assigned a probability of having originated from a bottom quark by the b-tagging algorithm described in Sec. 3.3.5. A jet in the analysis is considered to be b-tagged if its probability is larger than 0.8484. This value results in a b-tagging efficiency of $\sim 60\%$, as well as a mis-tagging rate of $\sim 10\%$ for charm quarks and $\sim 1\%$ for up, down, strange, and gluon quarks.

The jets employed in the analysis have transverse momenta and pseudorapidities satisfying $p_T > 40$ GeV and $|\eta| < 2.4$. The p_T threshold is chosen to avoid jets originating from pileup vertices.

Muons

The muons considered for event vetoing in the signal region are required to be reconstructed as either global or tracker muons. The efficiency for this is $\sim 98\%$. The contribution to the muon energy from pileup tracks is subtracted using the effective area correction. A mini-isolation requirement of $I_{\text{mini}}^{\text{rel}} < 0.2$ is imposed that aids in identifying muons from the decays of boosted top quarks.

In the control regions, global muons are selected. Additional quality criteria are required in order to enhance the purity of prompt W and Z boson decays. These include a minimum goodness of fit of the corresponding track, and a minimum number of hits in the muon chambers – this helps to suppress fake muons resulting from *hadron punch-through*, that is high energy hadron shower remnants that pene-

trate the calorimeters and reach the muon chambers. A minimum number of hits in the tracker is required to provide an accurate measurement of the momentum. The muon track is also required to be compatible with having originated from the primary vertex – this suppresses the potential background from cosmic muons and muons produced at a pileup vertex. The effective area pileup correction is applied. The relative isolation quantity is required to be $I^{\text{rel}} < 0.15$.

Muons in the control regions are required to satisfy $p_T > 30$ GeV and $|\eta| < 2.1$, while events in the signal region are vetoed if they contain any muons with $p_T > 10$ GeV and $|\eta| < 2.4$.

Photons

Events containing photons are vetoed in both the signal and control regions. The isolation of a photon is measured with respect to charged hadrons, neutral hadrons, and other photons within a $\Delta\eta - \Delta\phi$ cone of size 0.3. These three isolation variables are required to be below certain thresholds. An upper bound is also imposed on the ratio of the photon's energy deposited in the HCAL and the ECAL, which can be non-zero in the case of leakage of the electromagnetic shower. The shape of the shower as measured by the distribution of energy deposits in the ECAL crystals is used as a further discriminator. The photon identification efficiency following these requirements is $\sim 71\%$. The effects of pileup are mitigated using the effective area corrections.

Photons in the signal region satisfying $p_T > 25$ GeV and $|\eta| < 2.5$ are used to veto such events.

Electrons

The electrons considered for vetoing in the signal region are identified according to requirements on the shape of the electromagnetic shower, the ratio of energy deposits in the HCAL and ECAL, the number of hits in the tracker, and the track's impact parameter. These requirements provide an identification efficiency of $\sim 90\%$, and are effective at avoiding spurious electrons (such as jets misidentified as electrons) and electrons produced from photon conversions. Effective area pileup corrections and a mini-isolation requirement of $I_{\text{mini}}^{\text{rel}} < 0.1$ are applied.

Events in the signal region are vetoed if they contain electrons with $p_T > 10$ GeV and $|\eta| < 2.4$.

Isolated tracks

Events containing isolated tracks are vetoed in the signal and control regions as discussed in Sec. 4.5. An isolated track is defined to be a charged PF candidate that originates from the primary vertex and has a relative isolation (computed with respect to other charged PF candidates within a cone of size $\Delta R = 0.3$) of $I^{\text{rel}} < 0.1$.

Events in the signal region are vetoed if they contain an isolated track with $p_T > 10$ GeV and $|\eta| < 2.4$.

Energy sums

The H_T and \cancel{H}_T variables are defined, respectively, as the scalar sum and the magnitude of the negative vector sum of the transverse energy of all jets in the event satisfying $p_T > 40$ GeV and $|\eta| < 2.4$.

The missing transverse energy E_T is computed as the magnitude of the negative vector sum of the transverse energy of all PF candidates in the event. The jet energy corrections described in Sec.X are propagated as a correction to the E_T value [FIXME]. This variable is used in the definition of the M_T and \cancel{H}_T/E_T variables as described in Secs. 4.5 and 4.4.

4.2. Baseline selection

This section describes a set of baseline selections and filters that are used to ensure a final state with significant hadronic activity and genuine missing energy that is typical of the SUSY processes being searched for. These are summarised, along with the full set of selections described in Sec. 4.5, in Tab. 4.3.

Events in the signal region containing muons or electrons are vetoed. This mainly suppresses the $W + \text{jets}$ background process in which the W boson decays semileptonically, resulting in missing energy and a lepton in the final state. In case the

lepton is not identified as such but its track is reconstructed, events are vetoed if they contain an isolated track. This veto also helps to reject single prong decays of tau leptons. As a final requirement to ensure an all-jet final state, events containing photons are also vetoed.

At least one jet in the event is required to have a transverse momentum $p_T > 100$ GeV. The jet energy sums must satisfy $H_T > 200$ GeV and $\cancel{H}_T > 200$. These two thresholds are chosen to be as low as possible in order to maximise the acceptance of the search across a wide range of the SUSY mass parameter space, while simultaneously maintaining a reasonable trigger rate and efficiency. The trigger strategy will be discussed further in Sec. 4.7.

Missing energy is not only caused by undetectable or misreconstructed particles produced in the proton-proton collisions. Spurious \cancel{E}_T can also be induced by effects related to detector malfunctions and beam dynamics. These effects include spurious energy in the HCAL due to electronics noise and particle interactions with the instrumentation, missed energy in the ECAL due to dead cells, anomalous high amplitude pulses in certain ECAL endcap supercrystals, and beam halo particles. Beam halo refers to the showers of particles, including pions, neutrons and muons, that are produced when beam protons collide with residual gas particles in the LHC vacuum chambers or with the beam collimators. These beam halo particles can deposit energy in the calorimeters and CSCs of the muon system along lines parallel to the beam direction. Events affected by these spurious \cancel{E}_T sources are identified and vetoed using dedicated algorithms as described in Ref. [10]. These algorithms take advantage of various features related to geometrical patterns, pulse shapes and timing information. The impact of these filters on signal acceptance is negligible.

The beam halo filter, however, only targets halo muons, and is ineffective against calorimeter deposits from halo hadrons. These types of events are straightforwardly recognised, as shown in Fig. 4.1. The highest p_T jet in the event usually appears at ϕ values of 0 and π as this corresponds to the plane of the LHC ring in which the proton beams are steered, and will have a contribution from charged hadrons close to zero because of the lack of tracker hits. To suppress these beam halo events, events are rejected if the leading jet has a charged hadron energy fraction $f_{CH} < 0.1$.

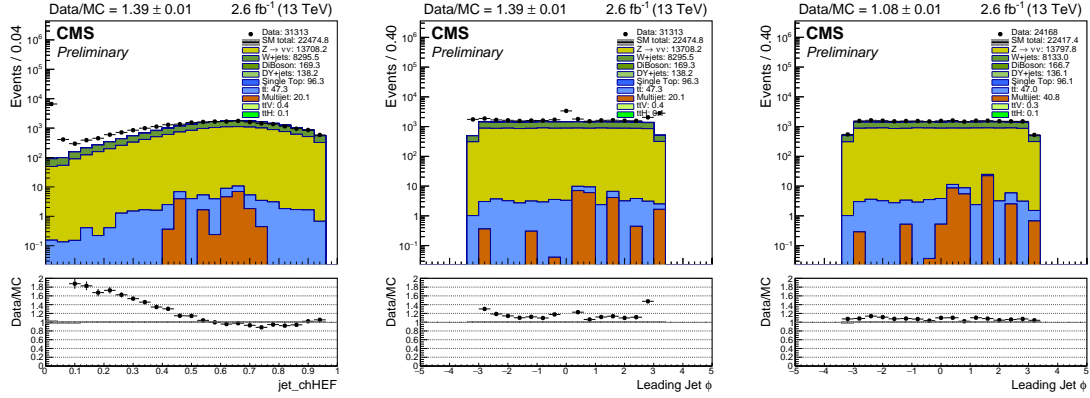


Figure 4.1.: The leading jet’s charged hadron energy fraction (left) and ϕ direction before (centre) and after (right) applying a requirement of $f_{CH} > 0.1$. The large excess in data at f_{CH} values close to zero and $\phi = 0$ and π is consistent with beam halo effects, and is effectively suppressed by the f_{CH} requirement.

As a further safeguard against noise and misreconstruction issues, events that contain a jet that fails the identification requirements outlined in Sec. 4.1 are not considered.

Finally within the set of baseline selections, events are vetoed if there are any jets with a pseudorapidity of $|\eta| > 2.4$. This threshold corresponds to the extent of the tracker and hence ensures well reconstructed jets and a better resolution of the energy sums. This requirement also has the added benefit of rejecting a larger proportion of background, particularly QCD multijet processes, compared to signal processes, which tend to have more central jets.

4.3. Standard model backgrounds

The baseline selections described in the previous section select events with significant hadronic activity and missing energy, as desired. However, a large number of standard model events still remain. These include processes (labelled electroweak background processes) with ‘genuine’ missing energy in the final state due to neutrinos, as well as QCD multijet processes with ‘fake’ missing energy in the final state due to jet energy mismeasurements.

4.3.1. Electroweak processes

The dominant electroweak background process (comprising $\sim 50\%$ of the signal region background events) is the production of a Z boson in association with jets, with the Z boson decaying to two neutrinos. This background is irreducible as the final state consists of only jets and missing energy, just like the SUSY processes being searched for.

The second largest background process (making up $\sim 40\%$ of the total background) is the production of a W boson in association with jets, with the W boson decaying semi-leptonically to a lepton and a neutrino. Such an event may not be vetoed if the lepton is not reconstructed or travels in a direction that is outside the acceptance of the detector, or is a muon or electron that fails the kinematic, identification, or isolation criteria listed in Sec. 4.1. If the lepton is a tau, it may decay semi-leptonically to a muon or electron that is not vetoed for the aforementioned reasons, or it may decay hadronically resulting in a jets plus \cancel{E}_T final state. In the case of a single-prong hadronic decay, the tau background is suppressed with a veto on events containing an isolated track, as mentioned in Sec. 4.2. The veto on isolated tracks cannot capture three-prong decays, however, as the tracks are usually not isolated and are instead reconstructed as a jet.

The third largest background process (constituting $\sim 5\%$ of the signal region background) is the production of top quark-antiquark pairs ($t\bar{t}$ + jets). This background is characterised by b-jets and a larger number of jets in the final state compared to the other two dominant backgrounds. Each top quark decays to a bottom quark and W boson, and each W boson can decay hadronically or semi-leptonically. The dominant decay mode in the signal region is the one in which one of the W bosons decays hadronically and the other decays semi-leptonically, resulting in a lepton that is then ‘lost’ in the same way as for the $W(\rightarrow \ell\nu) + \text{jets}$ background described previously. The decay mode in which both W bosons decay hadronically is negligible because there is no significant amount of missing energy in the final state. The decay mode in which both W bosons decay semi-leptonically is also negligible because of the low probability of losing both leptons.

Additional, residual standard model background processes include the production of a single top quark (in association with a b quark, light quark, or W boson), the production of vector boson pairs (WW, WZ, ZZ), $t\bar{t}$ production in association with a vector boson, $Z(\rightarrow \ell\ell) + \text{jets}$ production, and $\gamma + \text{jets}$ production.

4.3.2. QCD processes

At a hadron collider such as the LHC, the most abundant process is that of QCD multijet production, having a cross section that is several orders of magnitude larger than other standard model processes. The final state consists of two or more jets, and there is no intrinsic missing energy (except in the case of heavy flavour QCD, as discussed below). However, issues with the detector or inaccuracies in the reconstruction can cause the event to appear unbalanced in transverse momentum, thereby introducing fake \cancel{E}_T . Although these effects are not very common, when coupled with the large QCD production cross section, the result is that QCD multijet production remains as the largest background even when requiring a reasonable amount of \cancel{E}_T such as 200 GeV. The following is a comprehensive list of the various mechanisms by which QCD processes can have a large amount of missing energy. The next section will describe a set of variables that are used to identify and suppress this type of background.

- Soft jets with transverse momentum $p_T < 40$ GeV are not included in the computation of the jet energy sums, and therefore result in an apparently unbalanced event. The resulting missing jet energy is particularly significant when there are several jets below the p_T threshold. A similar problem can occur when the jets are outside the acceptance of the detector.
- Significant over or under-measurements of jets' energies due to the tails of the resolution distribution. This includes the mismeasurement of a single jet in the event, in which case the missing transverse momentum vector is collinear (if the jet's energy is under-measured; or anti-collinear if it is over-measured) to the jet's direction, as well as the mismeasurement of two or more jets, in which case the missing momentum is not aligned with any jet. A third effect is when a jet is severely under-measured such that its measured transverse momentum is below the 40 GeV threshold.
- Detector effects, such as dead cells and hot cells in the calorimeters, can result in a large amount of fake missing energy. These effects are dealt with by the dedicated \cancel{E}_T filters described in Sec. 4.2.
- The production of bottom quarks with a subsequent semi-leptonic decay leads to genuine missing energy in the final state due to the resulting neutrino. The lepton and neutrino are typically contained within the jet cone. This means

that the lepton is not isolated and so such events are not rejected by the lepton veto. It also means that the missing transverse momentum vector is roughly collinear with the jet.

The dominant mechanism by which QCD processes can pass the baseline selections is that due to jet energy mismeasurements ($\sim 70\%$), followed by jets below threshold ($\sim 30\%$). The heavy flavour and detector effects are comparatively much smaller ($\sim 1\%$).

4.4. QCD background rejection

It is important to suppress the overwhelming QCD background so that it does not swamp any potential signal. This section describes three key variables (α_T , $\Delta\phi_{\min}^*$, and \cancel{H}_T/E_T) that effectively distinguish QCD events from events with genuine missing energy. Each variable exploits certain topological or kinematical features, and each one targets different sources of missing energy of those described in the previous section.

Events in the signal region need to satisfy certain requirements on these variables, as will be in outlined in Sec. 4.5. These thresholds are chosen such that the QCD background forms no more than $\sim 1\%$ of the total standard model background in the signal region. This choice is motivated by the difficulty in estimating this type of background accurately and precisely. The difficulty arises from the lack of precise high-order theoretical calculations on the production cross section and kinematic properties. In addition, because of the large cross section and computing limitations, the number of simulated events is much smaller than that expected by the integrated luminosity of 35.9 fb^{-1} , and so the simulated events have large weights and hence large statistical uncertainties. Therefore, if QCD processes were to form a large part of the total expected background this would significantly reduce the sensitivity of the search. A small contribution of $\sim 1\%$, even with a large uncertainty, has a negligible impact on the sensitivity.

4.4.1. The α_T variable

The α_T variable is designed to discriminate between balanced events that may contain mismeasurements and unbalanced events containing invisible particles [11]. For a dijet event it is defined as:

$$\alpha_T = \frac{E_T^{j_2}}{M_T}, \quad (4.1)$$

where $E_T^{j_2}$ is the transverse energy of the least energetic jet, and M_T is the transverse mass of the dijet system, which is given in general for a number of jets by:

$$M_T = \sqrt{\left(\sum_i E_T^{j_i}\right)^2 - \left|\sum_i \mathbf{p}_T^{j_i}\right|^2}, \quad (4.2)$$

where $E_T^{j_i}$ is the transverse energy of the i^{th} most energetic jet, and $\mathbf{p}_T^{j_i} = (p_x^{j_i}, p_y^{j_i})$ is its transverse momentum vector, $p_x^{j_i}$ and $p_y^{j_i}$ being the x and y components, respectively.

To illustrate how the α_T variable works, one can assume the mass of the jets to be much smaller than their momenta (so that $E_T \approx p_T$, which is a good approximation for jets produced at the LHC), and rewrite M_T in terms of the azimuthal angle $\Delta\phi(j_1, j_2)$ between the two jets such that:

$$\alpha_T \approx \frac{E_T^{j_2}}{\sqrt{2E_T^{j_1}E_T^{j_2}(1 - \cos\Delta\phi(j_1, j_2))}}. \quad (4.3)$$

If the jets have equal and opposite transverse momenta such as in a QCD dijet event, then the azimuthal angle between them is π , their transverse energies are the same, and the value of α_T is exactly 0.5. If one of the jets' energies is mismeasured, then $E_T^{j_2} < E_T^{j_1}$ and α_T takes values less than 0.5. In an event where the jets are recoiling against a system of invisible particles, the angle between them is smaller than π and the value of α_T is generally larger than 0.5.

For events with more than two jets in the final state, the jets can be grouped into two *pseudo jets* such that the difference in transverse energy ΔE_T between the two pseudo jets is minimised, where the transverse energy of a pseudo jet is computed via the vector sum of the transverse energies of the constituent jets. This is done so

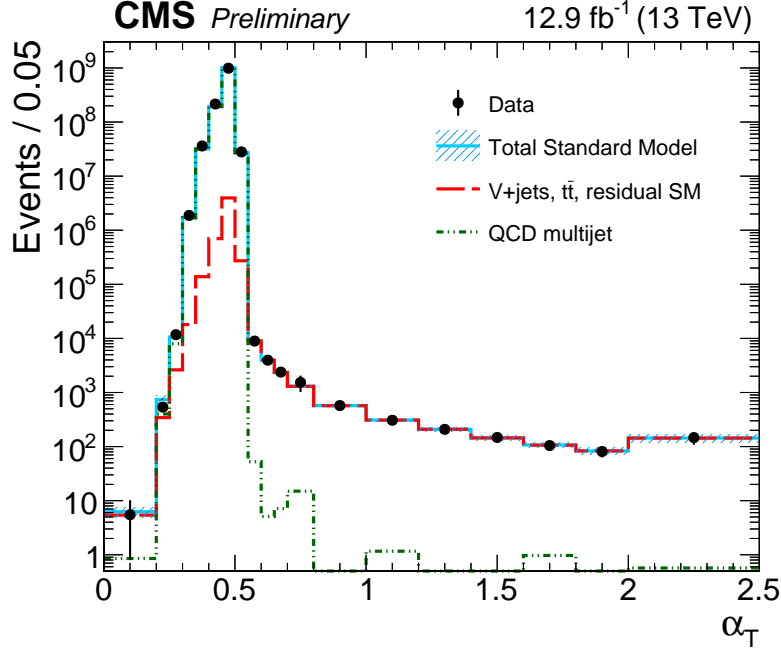


Figure 4.2.: The distribution of the α_T variable in data and simulation for events satisfying the signal region selections (Sec. 4.5) except the α_T requirement. The ability of the variable to effectively discriminate between QCD processes and processes with genuine missing energy is evidenced by the sharp edge at 0.5.

that the resulting pseudo dijet system is as close to a balanced event as possible. Since $\Delta E_T = E_T^{j_1} - E_T^{j_2}$ and $|\Sigma_i \mathbf{p}_T^{j_i}| = \cancel{E}_T$, the general form of the α_T variable can be defined as:

$$\alpha_T = \frac{\Sigma_i E_T^{j_i} - \Delta E_T}{2\sqrt{(\Sigma_i E_T^{j_i})^2 - \cancel{E}_T^2}}. \quad (4.4)$$

For balanced QCD events with no missing energy, $\Delta E_T = \cancel{E}_T = 0$ and $\alpha_T = 0.5$. If a jet in such an event is mismeasured, then $\Delta E_T \approx \cancel{E}_T$ and $\alpha_T < 0.5$. For events with genuine missing energy, $\cancel{E}_T > 0$ and $\Delta E_T = 0$, resulting in $\alpha_T > 0.5$.

The discriminating power of the α_T variable is shown in Fig. 4.2. Multijet QCD events are the dominant process in the region of $\alpha_T \leq 0.5$, while processes with genuine missing energy occupy the region of $\alpha_T > 0.5$. It is possible for QCD events to have values of α_T slightly larger than 0.5 if there is a severe mismeasurement or there are several jets below the p_T threshold.

4.4.2. The $\Delta\phi_{\min}^*$ variable

The $\Delta\phi_{\min}^*$ variable also provides powerful discrimination between events with fake missing energy and events with genuine missing energy. First it is instructive to consider the $\Delta\phi_{\min}$ variable, which is the minimum (over all jets in the event above the p_T threshold) azimuthal angle between a jet and the missing transverse jet energy vector:

$$\Delta\phi_{\min} = \min \Delta\phi \left(\vec{p}_T^{j_i}, \vec{H}_T \right). \quad (4.5)$$

If a jet's energy in the final state is under-measured, the missing energy vector is collinear with the jet direction, and so $\Delta\phi_{\min}$ is zero, whereas for processes in which the jets are recoiling against genuine missing energy, the value of $\Delta\phi_{\min}$ is non-zero.

However, if a jet's energy is over-measured, the missing energy vector points in the opposite direction to the jet and so $\Delta\phi_{\min}$ is not necessarily zero. This limitation can be overcome by comparing the jet's direction with the missing energy vector that does not consider the jet in the vector sum, $\vec{H}_T^{j_i} = \vec{H}_T + \vec{p}_T^{j_i}$. This is the definition of the $\Delta\phi_{\min}^*$ variable:

$$\Delta\phi_{\min}^* = \min \Delta\phi \left(\vec{p}_T^{j_i}, \vec{H}_T^{j_i} \right). \quad (4.6)$$

The discriminating power of the $\Delta\phi_{\min}^*$ variable is shown in Fig. 4.3. Multijet QCD events have values of $\Delta\phi_{\min}^*$ close to 0, with the distribution falling sharply beyond this, whereas processes containing genuine missing energy exhibit a longer tail up to values of π radians.

The $\Delta\phi_{\min}^*$ variable is effective at capturing QCD events that contain a single mismeasurement or a neutrino produced by a heavy quark decay that is collinear with a jet. It is less effective if a jet is severely mismeasured such that its p_T is below threshold, or if there are two or more mismeasured jets. Both of these cases result in missing momentum that is not necessarily collinear with any jet.

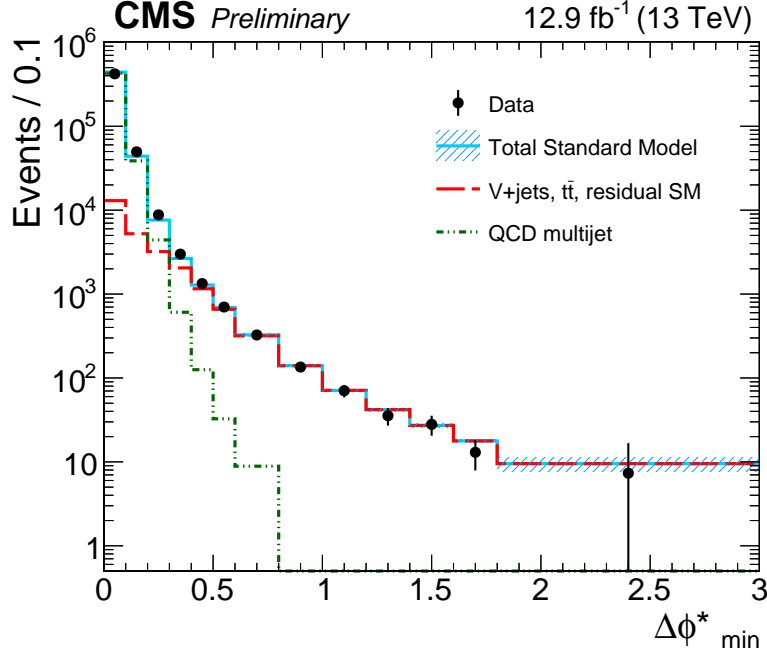


Figure 4.3.: The distribution of the $\Delta\phi_{\min}^*$ variable in data and simulation for events satisfying the signal region selections (Sec. 4.5) except the $\Delta\phi_{\min}^*$ requirement. The ability of the variable to effectively discriminate between QCD processes and processes with genuine missing energy is evidenced by the cluster of QCD events close to 0, while processes with genuine E_T take on larger values up to π radians.

4.4.3. The \cancel{H}_T/E_T variable

As mentioned previously, the α_T and $\Delta\phi_{\min}^*$ variables are not as effective at identifying QCD events in which there are several jets with transverse momentum below the 40 GeV threshold. In such events, the value of \cancel{H}_T is biased to larger values. The E_T variable, however, is computed using all PF objects in the event satisfying a much lower threshold (10 GeV for jets) and so is less susceptible to this bias and remains closer to zero. One can compare the values of \cancel{H}_T and E_T to identify these events – the ratio of \cancel{H}_T/E_T tends to be significantly larger than 1 for such events.

For processes with genuine missing energy, on the other hand, the ratio generally remains close to unity as the increase in missing energy due to threshold effects is proportionally smaller with respect to the true missing energy which is already relatively large. The distribution of the \cancel{H}_T/E_T ratio is shown in Fig. 4.4 and demonstrates the difference between the two types of backgrounds. Multijet QCD processes tend to populate the region of $\cancel{H}_T/E_T > 1.25$.

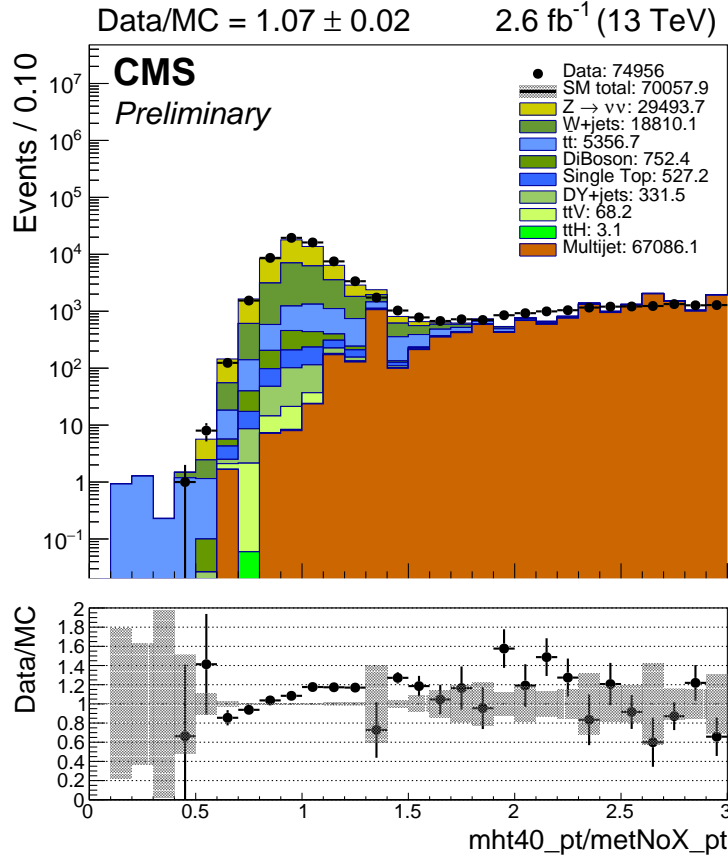


Figure 4.4.: The distribution of the m_{HT}/E_T ratio in data and simulation for events satisfying the signal region selections (Sec. 4.5) except the m_{HT}/E_T requirement. The ability of the variable to effectively discriminate between QCD processes and processes with genuine missing energy is evidenced by the population of QCD events above 1.25, while processes with genuine E_T have values more consistent with unity. [FIXME: remove ratio plot and fix axis label? Update to 36fb]

4.5. Event selection

After the baseline selections outlined in Sec. 4.2, additional selections are applied in order to suppress the QCD background in the signal region and enrich the control regions in the relevant standard model processes that need to be estimated. These are described in this section and are summarised, along with the baseline selections described in Sec. 4.2, in Tab. 4.3.

Baseline selection	
All-jet final state	At least one jet; no muons, electrons, photons or isolated tracks
\cancel{E}_T quality	No spurious \cancel{E}_T due to instrumental effects or beam halo
Jet energy and sums	$p_T^j > 100$ GeV, $H_T > 200$ GeV, $\cancel{H}_T > 200$ GeV
Jets outside acceptance	$\cancel{H}_T/\cancel{E}_T < 1.25$; no jets with $ \eta > 2.4$
Jet quality	No jets that fail identification criteria
Signal region	
$\alpha_T (>)$ (H_T GeV range)	0.65 (200-250), 0.60 (250-300), 0.55 (300-350), 0.53 (350-400), 0.52 (400-900)
$\Delta\phi_{\min}^*$	$\Delta\phi_{\min}^* > 0.5$
Control regions	
μ + jets	Baseline selection + One muon; $\min \Delta R(\mu, j_i) > 0.5$; $30 < M_T(\mu, \cancel{E}_T) < 125$ GeV
$\mu\mu$ + jets	Two muons opp. charge; $\min \Delta R(\mu_{1,2}, j_i) > 0.5$; $ M(\mu_1, \mu_2) - m_Z < 25$ GeV
Hadronic	Signal region sidebands $1.25 < \cancel{H}_T/\cancel{E}_T < 3.0$ and/or $0.2 < \Delta\phi_{\min}^* < 0.5$

Table 4.3.: Summary of selections as part of the definition of the signal and control regions.

4.5.1. Signal region

The baseline selections in the signal region are chosen to ensure a hadronic final state with significant energy and missing momentum that is characteristic of the SUSY models that are sought. As a reminder, these include minimum requirements on H_T and \cancel{H}_T , and event vetoes on non-hadronic objects and forward jets as well as spurious \cancel{E}_T sources. However, a large number of QCD events remain that contain fake missing energy (or missing energy from heavy quark decays). This background is suppressed to a very small level ($\lesssim 1\%$ of the total standard model background) by imposing certain requirements on the QCD-discriminating variables α_T , $\Delta\phi_{\min}^*$, and $\cancel{H}_T/\cancel{E}_T$ described in the previous section.

An H_T -dependent α_T requirement is used for multijet events, as summarised in Tab. 4.4. For events containing only one jet above 40 GeV, α_T is undefined and no requirement is imposed. The α_T threshold is as high as 0.65 for events with $200 < H_T < 250$ GeV, and is reduced with increasing H_T down to 0.52 for events with $400 < H_T < 900$ GeV, while no requirement at all is made for $H_T > 900$ GeV. The thresholds are a decreasing function of H_T because the expected number of QCD events falls quickly with increasing H_T . The thresholds are also chosen to ensure that events are triggered with full efficiency, as the α_T trigger thresholds

have been chosen to provide a reasonable trigger rate. The trigger strategy will be discussed in Sec. 4.7.

H_T (GeV)	200-250	250-300	300-350	350-400	400-900	>900
α_T requirement ($>$)	0.65	0.60	0.55	0.53	0.52	0

Table 4.4.: The α_T thresholds as a function of H_T for events containing at least two jets. No requirement is made on events containing only one jet.

Any QCD background events not captured by the α_T selection, in particular events with $H_T > 900$ GeV or with only one jet for which there is no α_T requirement, are suppressed by a requirement on $\Delta\phi_{\min}^*$. The threshold is chosen to be $\Delta\phi_{\min}^* > 0.5$ radians for all events, regardless of H_T and the number of jets. For monojet events, $\Delta\phi_{\min}^*$ is undefined when using only jets with $p_T > 40$ GeV, and is instead computed using jets that satisfy a lower threshold of $p_T > 25$ GeV. If there are no jets with $25 < p_T < 40$ GeV, $\Delta\phi_{\min}^*$ remains undefined and no requirement is made on monojet events. The α_T variable could also be defined similarly using jets of lower p_T , but QCD events are produced with at least two jets, so QCD monojet events (which must result from a severe mismeasurement) form a relatively smaller background and these are effectively suppressed by the $\Delta\phi_{\min}^*$ requirement alone.

Finally, in order to suppress the fake \cancel{E}_T QCD background due to several jets with a transverse momentum below the 40 GeV threshold, a requirement is made on the $\cancel{H}_T/\cancel{E}_T$ ratio of $\cancel{H}_T/\cancel{E}_T < 1.25$.

4.5.2. Control regions

Each control region is used to estimate a particular standard model background process. The estimation methods will be discussed in Secs. 4.10 and 4.11. The selections in the control regions are chosen so that they are enriched in the background processes that each is designed to estimate, while remaining kinematically as similar as possible to the signal region. For this reason, the selections are the same as in the signal region except for the inversion of certain requirements and additional purity criteria, as described in the following subsections.

In the case of the two muon control regions, the muons are not included in the computation of \cancel{E}_T (and similarly all jet-based variables) in order to mimic the

missing energy due to the neutrinos or lost lepton. The control regions are also orthogonal to the signal region (an event cannot occupy both regions, by construction) and are expected to contain very little signal. In any case, any potential signal contamination in the control regions is accounted for in the statistical model (Sec. 5.3).

μ + jets control region

The μ + jets control region is used to estimate the $W(\rightarrow \ell\nu)$ + jets and $t\bar{t}$ backgrounds (plus the residual backgrounds). The selections are chosen to identify W bosons, originating from such processes, decaying to a muon and a neutrino.

The muon veto of the signal region is inverted and instead exactly one muon (as defined in Sec. 4.1) is required. The muon is required to be separated from the closest jet by $\Delta R(\mu, \text{jet}) > 0.5$ in order to select isolated muons from prompt W decays rather than from QCD decays.

To improve the purity in W bosons, the transverse mass of the muon and missing transverse energy (which is a proxy for the neutrino) is required to be compatible with the W mass with $30 < M_T(\mu, \cancel{E}_T) < 125$ GeV. The transverse mass must be used rather than the invariant mass as the z-component of the missing momentum is unknown.

All of these criteria are effective at selecting a pure sample of $W(\rightarrow \ell\nu)$ + jets and $t\bar{t}$ events with minimal QCD contamination, and hence no requirements on α_T or $\Delta\phi_{\min}^*$ are made in this control region. This has the benefit of significantly increasing the number of events in the control region, which decreases the statistical uncertainties associated with the corresponding background estimations. Any potential issues in the background estimation arising from different α_T and $\Delta\phi_{\min}^*$ selections are accounted for as a systematic uncertainty (see Sec. 4.12.2).

$\mu\mu$ + jets control region

The $\mu\mu$ + jets control region is used to estimate the main irreducible $Z(\rightarrow \nu\nu)$ + jets background. The selections are chosen to identify Z bosons decaying to two muons. The muon veto of the signal region is again inverted and instead exactly two muons, of opposite charge, are required. Each muon is required to be separated in ΔR

from jets by the same amount as in the $\mu + \text{jets}$ control region. In order to improve the purity in Z bosons, the invariant mass of the dimuon system is required to be compatible with the mass of the Z boson, with $|M(\mu_1, \mu_2) - m_Z| < 25 \text{ GeV}$. Similarly to the $\mu + \text{jets}$ control region, no requirements on α_T and $\Delta\phi_{\min}^*$ are needed.

Hadronic control regions

Three hadronic control regions are used in the estimation of the small QCD background remaining after the full set of selections have been applied. These control regions consist of the exact same selections as the signal region, except that the $\Delta\phi_{\min}^*$ and \cancel{H}_T/E_T requirements are inverted, both individually and in conjunction, providing three control regions or “sidebands” that are enriched in QCD processes. The sidebands are capped such that $0.2 < \Delta\phi_{\min}^* < 0.5 \text{ rad}$ and $1.25 < \cancel{H}_T/E_T < 3.0$. Table 4.5 shows a summary of the selections that define these sidebands.

Table 4.5.: The definitions of the sideband regions employed in the estimation of the QCD background.

	$0.2 < \Delta\phi_{\min}^* < 0.5$	$\Delta\phi_{\min}^* > 0.5$
$1.25 < \cancel{H}_T/E_T < 3.0$	$\cancel{H}_T/E_T - \Delta\phi_{\min}^*$ sideband	\cancel{H}_T/E_T sideband
$\cancel{H}_T/E_T < 1.25$	$\Delta\phi_{\min}^*$ sideband	Signal region

4.6. Event categorisation

Events are categorised, or binned, according to four variables. This is done to improve the discrimination between signal and background processes, which tend to populate different regions of this four-parameter space. Moreover, different SUSY processes occupy different regions depending on the particular production mode and final state considered. The four variables are the number of jets n_{jet} , the number of b-tagged jets n_b , the total jet energy H_T , and the missing transverse jet energy \cancel{H}_T . The binning scheme and motivation for each discriminating variable are described in this section.

The control regions are binned identically to the signal region, with some exceptions in the \cancel{H}_T and n_b dimensions that will be explained in this section. This is done to ensure that the backgrounds are estimated (as described in Sec. 4.10) using events in the control regions of similar kinematic and topological properties. Any estimations that are not made between equivalent bins, or are made directly according to simulation, are assigned an additional systematic uncertainty.

A summary of the bins used in the signal region is provided in Tab. 4.6. In total there are 574 bins, with 254 in the signal region, 198 in the $\mu + \text{jets}$ control region, and 122 in the $\mu\mu + \text{jets}$ control region.

The hadronic control regions are categorised slightly differently, with coarser bins. These regions do not form part of the overall statistical model used to derive limits or significances, and instead are used to estimate the QCD background separately. This will be discussed in Sec. 4.11.

Categorisation by n_{jet}

First, it is convenient to define the topology of a final state in terms of the momenta of the two most energetic jets. As mentioned in Sec. 4.2, the leading jet is required to have a transverse momentum larger than 100 GeV. If the sub-leading jet also has $p_T > 100$ GeV, the event is categorised as *symmetric*. If it has $40 < p_T < 100$ GeV, the event is labelled *asymmetric*. If it has $p_T < 40$ GeV or if there are no additional jets in the final state, it is categorised as a *monojet* event.

The symmetric category captures many of the SUSY production scenarios in which the mass difference with respect to the LSP is large and the final state contains several highly energetic jets. In the case of a small mass difference, little kinetic energy is available for the decay products and so the acceptance for these models, which relies more on ISR and FSR, is provided by the asymmetric and monojet categories. These categories are also useful at capturing models of long-lived supersymmetry in which the decays occur outside of the detector, as the identification of these events relies on the initial state radiation.

Events are categorised according to the number of jets in the final state and the jet topology. The seven categories employed are $n_{\text{jet}} = 1, \geq 2a, 3, 4, 5, \geq 6$, where the a denotes an asymmetric topology.

n_{jet}	n_b	H_T (GeV)				
		200-250, 250-300, 300-350, 350-400	400-500, 500-600	600-750, 750-900	900-1050, 1050-1200	>1200
1	0	200	200	200	200	–
	1	200	200	200	–	–
$\geq 2a$	0	200	200,400	200,400,600	200,900	–
	1	200	200,400	200,400,600	200,900	–
	2	200	200,400	200,400,600	200,900	–
	≥ 3	200	200,400	200,400,600	–	–
2	0	200	200,400	200,400,600	200,400,600,900	200,400,600,900
	1	200	200,400	200,400,600	200,400,600,900	200,400,600,900
	2	200	200,400	200,400,600	–	–
3	0	200	200,400	200,400,600	200,400,600,900	200,400,600,900
	1	200	200,400	200,400,600	200,400,600,900	200,400,600,900
	2	200	200,400	200,400,600	200,400,600,900	200,400,600,900
	3	200	200,400	200,400,600	–	–
4	0	–	200,400	200,400,600	200,400,600,900	200,400,600,900
	1	–	200,400	200,400,600	200,400,600,900	200,400,600,900
	2	–	200,400	200,400,600	200,400,600,900	200,400,600,900
	≥ 3	–	200,400	200,400,600	200,400,600,900	–
5	0	–	200,400	200,400,600	200,400,600	200,400,600,900
	1	–	200,400	200,400,600	200,400,600	200,400,600,900
	2	–	200,400	200,400,600	200,400,600	200,400,600,900
	3	–	200,400	200,400,600	200,400,600	–
	≥ 4	–	200,400	–	–	–
≥ 6	0	–	200	200,400	200,400,600	200,400,600,900
	1	–	200	200,400	200,400,600	200,400,600,900
	2	–	200	200,400	200,400,600	200,400,600,900
	3	–	200	200,400	200,400,600	200,400,600,900
	≥ 4	–	200	–	–	–

Table 4.6.: Summary of all bins in the signal region. The listed numbers correspond to the lower boundaries of the \cancel{H}_T bins in each $(n_{\text{jet}}, n_b, H_T)$ bin; the final number in the list is always an open bin. A single-element list is equivalent to no binning in \cancel{H}_T . A dash means a particular $(n_{\text{jet}}, n_b, H_T)$ bin is not used, and so the previous H_T bin (if applicable) is an open bin. The muon control regions are binned identically, except that they are not binned in \cancel{H}_T , and the largest n_b category in the $\mu\mu$ + jets control region is ≥ 1 .

Categorisation by H_T

The H_T variable also provides a measure of the mass scale of a BSM physics process and the corresponding hadronic activity in the event. Events are categorised by H_T as follows: four bins of width 50 GeV in the range 200-400 GeV, two bins of

width 100 GeV in the range 400-600 GeV, four bins of width 150 GeV in the range 600-1200 GeV, and a final open bin $H_T > 1200$ GeV. To maintain a manageable number of bins, these 11 bins are aggregated in the signal region to just 5: 200-400, 400-600, 600-900, 900-1200, and ≥ 1200 GeV.

The exact H_T binning scheme depends on n_{jet} and is included in Tab. 4.6. Because of the $p_T > 40$ GeV threshold on jets, certain low H_T bins at high n_{jet} are restricted or non-physical and are therefore not considered. High H_T bins at high n_{jet} can be statistically limited and are merged from above so that the corresponding bin in the control region is well populated and the statistical uncertainty on the estimated background is not too large.

Categorisation by n_b

The number of b-tagged jets is an effective discriminator for SUSY models that involved the production of heavy quarks. The standard model background containing b-tagged jets is relatively smaller, and mainly comes from $t\bar{t}$ production, as well as some contribution from $W + \text{jets}$ and $Z + \text{jets}$ in which a jet is mistagged. Additional sensitivity is also found for long-lived particles with lifetimes similar to that of b quarks, as their hadronic decay products can be reconstructed as b-tagged jets.

Events are categorised according to $n_b = 0, 1, 2, 3, \geq 4$. Again, the exact binning scheme depends on n_{jet} and is included in Tab. 4.6. The largest n_b bin can be at most equal to n_{jet} . Bins are also merged from above according to the number of data counts in the $\mu + \text{jets}$ control region to ensure that the backgrounds estimations do not suffer from large statistical uncertainties. As the $\mu\mu + \text{jets}$ control region is somewhat statistically limited, especially at high n_b , the largest n_b bin employed in this control region is $n_b \geq 1$.

Categorisation by H_T

The signal region is additionally categorised according to \cancel{H}_T . This helps to further separate the background and signal, as signal processes tend to have values of \cancel{H}_T closer to H_T .

Events are categorised in \cancel{H}_T using up to four bins, that are aligned with the boundaries of the H_T bins: 200-400, 400-600, 600-900, ≥ 1200 GeV. In this case, the value of \cancel{H}_T is bounded above by H_T by construction. Bins are again merged from above to ensure each bin is well populated by simulated events. For events with $n_{\text{jet}} = 1$, for which $\cancel{H}_T = H_T$, or with $200 < H_T < 400$ GeV, no binning in \cancel{H}_T is employed.

Unlike with the n_{jet} , n_b and H_T variables, events in the control regions are not binned in the \cancel{H}_T dimension. The background estimations in each \cancel{H}_T bin are taken directly from simulation instead of being derived from the control regions. This is done to avoid binning the control regions too finely, which would greatly reduce their statistical power. A validation of this method will be discussed in Sec. 4.10.2.

4.7. Trigger

As discussed previously, the aim of the search is to be as inclusive as possible to a wide range of new physics processes by having low thresholds on the amount of hadronic activity and missing energy. This is particularly important for models with a compressed mass spectrum, as well as models with long-lived particles, as these contain relatively fewer and/or softer jets in the final state. The acceptance of the search towards these BSM physics processes is therefore largely dependent on the ability of the trigger to effectively select such events.

The HL trigger thresholds are optimised to provide a maximal acceptance subject to constraints on the readout rate and the processing time. As there is often an overlap between events selected by different triggers, and the same physics objects are used by various triggers, the quantities of importance for a particular trigger are the *effective* or *exclusive* rate and processing time. These are, respectively, the rate and processing time added by that trigger to the overall HLT menu. The total available rate and processing time of the HLT are ≈ 1 kHz and ≈ 200 ms, respectively, while individual triggers are typically constrained to have an effective rate and processing time of at most a few Hz and a few milliseconds.

The triggers for this search make use of QCD-discriminating variables such as α_T to control the readout rate, and the thresholds are essentially chosen to be as low as possible while satisfying the rate constraint and ensuring a good selection efficiency

for events in the signal region. The triggers make use of Particle Flow reconstruction, which is a computationally intensive task as it involves the combination of information from various sub-detectors. To help satisfy the timing constraint, loose requirements are first made using simpler objects, such as jets reconstructed using only the calorimeters, before proceeding with the PF reconstruction and final trigger selections.

In order to reduce the readout rate, triggers may be assigned a *prescale factor* f_{ps} , which is defined such that the probability that an event which satisfies the trigger requirements is read out is $1/f_{ps}$. This means that a trigger with, say, $f_{ps} = 10$ only records approximately one in every ten events that satisfy its requirements.

Several versions of the same trigger are usually included in the HLT menu, each with slightly different thresholds that are suited for different LHC running conditions. As the instantaneous luminosity is increased throughout an LHC fill and throughout the year, the lower threshold versions become prescaled or disabled. To avoid large statistical uncertainties, only events collected by unprescaled triggers are considered in the search.

4.7.1. Signal and control region triggers

Various triggers are utilised to collect data in the signal and control regions. These are described in the following and summarised in Tab. 4.7, which shows the thresholds employed by each trigger and the amount of data collected by each one. All HL triggers employ Particle Flow reconstruction.

Three groups or families of triggers, which will be described in this section, are used to collect events in the signal region and hadronic control regions. An event that satisfies any of these triggers is selected.

The first group consists of five triggers with requirements on both H_T and α_T . These are designed to map onto the selections employed in the analysis (described in Sec. 4.5). Their thresholds on (H_T, α_T) are (200, 0.57), (250, 0.55), (300, 0.53), (350, 0.52), (400, 0.51). This set of triggers collected data for approximately the first half of the 2016 run, and were substituted by slightly higher α_T thresholds in the second half when the instantaneous luminosity reached $10^{34} \text{ cm}^{-2} \text{ s}^{-1}$. These triggers are most effective at selecting multijet events with a symmetric topology. The

HLT requirements	L1 seed requirements	HLT unscaled fraction
$H_T > 200 \wedge \alpha_T > (0.57, 0.63)$	$H_T > (240, 300) \vee \cancel{E}_T > (60, 100)$	(0.53, 0.47)
$H_T > 250 \wedge \alpha_T > (0.55, 0.58)$	$H_T > (240, 300) \vee \cancel{E}_T > (60, 100)$	(0.53, 0.47)
$H_T > 300 \wedge \alpha_T > (0.53, 0.54)$	$H_T > (240, 300) \vee \cancel{E}_T > (60, 100)$	(0.53, 0.47)
$H_T > 350 \wedge \alpha_T > (0.52, 0.53)$	$H_T > (240, 300) \vee \cancel{E}_T > (60, 100)$	(0.53, 0.47)
$H_T > 400 \wedge \alpha_T > (0.51, 0.52)$	$H_T > (240, 300) \vee \cancel{E}_T > (60, 100)$	(0.53, 0.47)
$\cancel{E}_T, \cancel{H}_T > (90, 100, 110, 120)$	$\cancel{E}_T > (60, 100)$	(0.39, 0.10, 0.49, 0.02)
$H_T > (800, 900)$	$H_T > (240, 300)$	(0.76, 0.24)
$p_T(\mu) > (22, 24)$	$p_T(\mu) > (18, 22)$	(0.80, 0.20)

Table 4.7.: List of L1 and HL triggers utilised in this search, grouped by family, indicating in parentheses their varying thresholds throughout the 2016 LHC run. All quantities related to energy and momentum are quoted in GeV units. The muon trigger is employed in the muon control regions, while all other triggers listed are employed in the signal region and hadronic control regions. The H_T - α_T triggers also have a minimum requirement of 90 GeV on the average p_T of the two leading jets, which did not change throughout run. Also provided is the fraction of the run for which a given trigger version was the lowest-threshold unscaled trigger.

requirement on α_T helps to suppress QCD events and maintain significantly lower thresholds on H_T than would be possible with a pure H_T trigger. These triggers also have a threshold of 90 GeV on the average p_T of the two most energetic jets in the event, which is necessary to maintain reasonable trigger rates. This reduces their efficiency for selecting events with an asymmetric jet topology.

The second type of trigger is one with requirements on both \cancel{E}_T and \cancel{H}_T . These are used to collect events with a monojet or asymmetric topology more effectively than the H_T - α_T triggers. The initial threshold on \cancel{E}_T and \cancel{H}_T was 90 GeV, and was raised throughout the 2016 run up to 120 GeV.

The third type of trigger is one with a requirement only on H_T . In this case the threshold was either 800 or 900 GeV. This trigger is used to collect events in the $H_T > 900$ GeV region in which there is no α_T requirement.

For both the μ + jets and $\mu\mu$ + jets control regions, events are collected using a trigger that requires at least one isolated muon with a transverse momentum larger than 22 GeV (24 GeV later in the run).

Prior to the HLT, events are filtered by the Level 1 trigger. Each HL trigger is preceded, or *seeded*, by a particular L1 trigger. The L1 seeds for the HL triggers

employed in this search consist of requirements on H_T , E_T and muon p_T , as summarised in Tab. 4.7.

4.7.2. Trigger efficiency

Accurately measuring the efficiency of the triggers is important as these affect the background estimations. Due to imperfect or a lack of trigger emulation in the simulation, the efficiencies need to be measured in data and used to correct the simulation. More details on this will be provided in Sec. 4.9.

The efficiency of a trigger is defined to be the fraction of events satisfying a set of *offline* requirements, such as those of the signal region, that are selected by that trigger. The efficiency should be ideally close to 100%. An inefficiency may arise close to the trigger threshold due to differences in the online and offline reconstruction. For instance, instead of Particle Flow reconstruction, jets in the HLT prefilter are reconstructed using solely calorimeter deposits, and jets in the L1 trigger are reconstructed using relatively coarse calorimeter information.

In order to estimate the efficiency of a trigger using data, one can measure the fraction of events collected by an alternative, *reference* trigger that satisfy the offline criteria. One possibility for a reference trigger is a pure H_T trigger with a relatively low threshold. However, pure H_T triggers are highly prescaled and result in a large statistical uncertainty on the measured efficiency. Unprescaled single electron and muon triggers are instead chosen as references. These provide a sample of events that are inclusive with respect to the variables employed in the signal region triggers.

When using lepton reference triggers to measure efficiencies, one must account for differences in the treatment of leptons in the L1T, the HLT, and offline. As muons deposit a negligible amount of energy in the calorimeters, they are not reconstructed as jets in the L1T and HLT prefilter, whereas electrons are. Offline, both electrons and muons are initially reconstructed as jets by the Particle Flow algorithm which clusters all PF candidates. These ‘fake’ jets are then removed from the event if they are close to an isolated lepton, in a process known as *cross-cleaning*. At the HLT, which also utilises PF reconstruction, cross-cleaning of muons is only employed by the E_T - H_T triggers. Cross-cleaning of electrons is not performed for any of the HL triggers. An inconsistency in the treatment of leptons and jets across

the L1, HLT and offline reconstruction chain would introduce a bias in a trigger efficiency estimate using a lepton trigger reference. For instance, a pure H_T trigger may falsely appear more efficient as the lepton would artificially enlarge the H_T of the event. In order to have a treatment that is as consistent as possible and avoid a bias in the measured trigger efficiency, cross-cleaning of offline electrons and muons is either enabled or disabled as appropriate for the particular trigger being measured. A completely unbiased estimate is not always possible, such as when measuring the H_T and $H_T\text{-}\alpha_T$ efficiencies via a muon sample. However, the triggers are almost fully efficient in the signal region phase space and any bias is covered with a conservative systematic uncertainty, as will be discussed further in Sec. 4.12.

The trigger efficiency is measured using both electron and muon reference triggers as a function of \cancel{H}_T in bins of H_T , both corresponding to quantities computed offline. The efficiency in the 2016 data taking period is shown in Fig. 4.5. The triggers have an efficiency $> 90\%$ for $\cancel{H}_T > 200$ GeV, and are practically fully efficient above 300 GeV. The discrepancy in the *turn-on* region of the efficiency curve between the muon and electron samples is attributed to differences in cross-cleaning methods, and motivates a selection of $\cancel{H}_T > 200$ GeV in the signal region. One could reduce this threshold to ~ 100 GeV to increase the acceptance of the search, but the lack of a precise knowledge of the trigger efficiency in this region would incur a bias and large uncertainty on the background expectation which would practically nullify the search's sensitivity in this region.

This section has focussed on the signal region triggers. The efficiency of the muon trigger is also measured in data and used to correct the trigger efficiency in the simulation. This will be discussed further in Sec. 4.9.

4.8. Data sets and simulation samples

This section describes the data sets in which the search for supersymmetry takes place, as well as the simulated data sets that aid in the estimation of the background and signal processes.

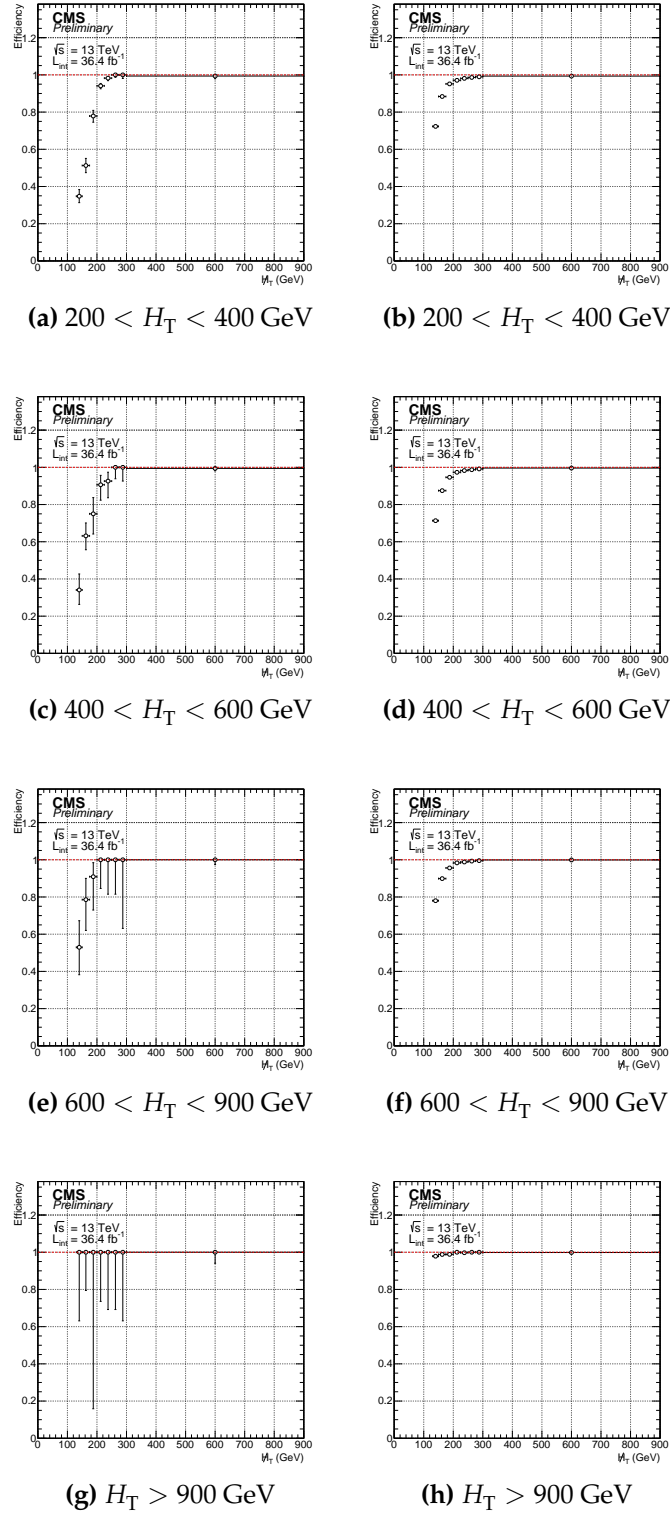


Figure 4.5.: Efficiency of the HL trigger in the signal region as a function of offline \cancel{H}_T and H_T , measured in a data sample collected by a single electron (left) and single muon (right) trigger.

4.8.1. Data sets

Between 22nd April 2016 and 27th October 2016, the LHC delivered a total integrated luminosity of 40.8 fb^{-1} of proton-proton collisions at a centre of mass energy of $\sqrt{s} = 13 \text{ TeV}$ with a proton bunch spacing of 25 ns. Of this, 37.8 fb^{-1} (93%) was recorded by the CMS detector, and 35.9 fb^{-1} (88%) was certified as containing data of good quality, meaning there were no associated detector or reconstruction issues. The amount of data delivered, recorded and certified over the year is shown in Fig. 4.6. It is the certified 35.9 fb^{-1} of data that form the basis of the search. The data sets that are analysed correspond to those collected by the triggers described in Sec. 4.7.

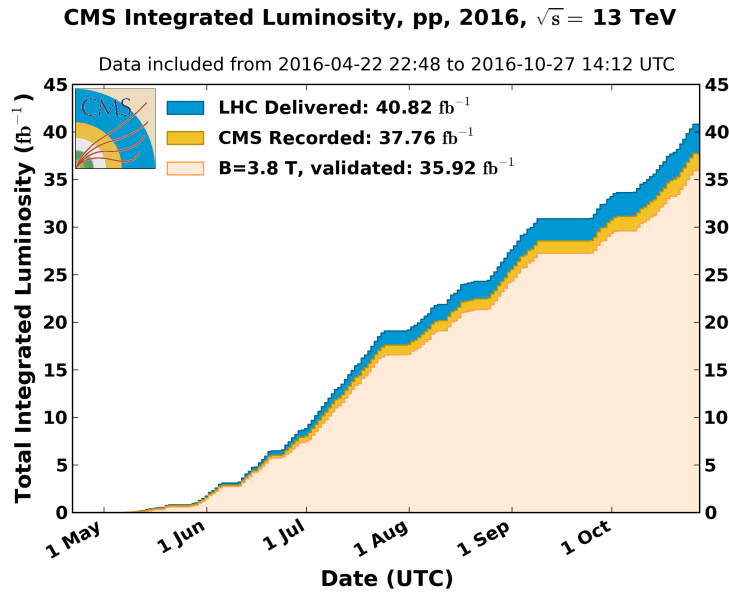


Figure 4.6.: Cumulative integrated luminosity of pp collisions at $\sqrt{s} = 13 \text{ TeV}$ delivered by the LHC, recorded by CMS, and certified as good for physics analysis per day during the year 2016 [12].

4.8.2. Simulation samples

The methods of Monte Carlo event generation, hadronisation and detector simulation were described in Sec. 3.4. The Monte Carlo generation of the main background processes (QCD, Z + jets, W + jets, $t\bar{t}$) is produced via the MADGRAPH5 [1, 13] generator framework at leading order (LO) precision. As the number of events falls exponentially with the energy scale of the event, and it is the most energetic events

that typically pass the signal region requirements, these samples are generated in various bins of \hat{H}_T , the total hadronic energy of the partons produced in the hard scattering. This improves the statistical precision of the simulation in the phase space region of interest. Single top quark production is generated at next-to-leading order (NLO) using both MADGRAPH5 and POWHEG [2] for the different production channels. The diboson background is generated with PYTHIA8 [3]. While events are generated at LO or NLO, the cross sections of most of the main background processes are computed at next-to-next-to-leading order (NNLO) precision.

The SUSY simplified models are generated with MADGRAPH5. For each model, various masses and lifetimes of the relevant particles are generated. This allows for the sensitivity of the search to be explored as a function of these variables. The model with a promptly-decaying gluino is simulated via a *fast simulation* framework which employs a simplified detector geometry and smearing of the particles' four-vectors, enabling it to perform ~ 100 times faster than a full simulation with GEANT but with comparable accuracy [14].

The formation of R-hadrons through the hadronisation of gluinos is described by PYTHIA8. The hadronisation process is assumed to yield predominantly meson-like ($\tilde{g}q\bar{q}$) and baryon-like ($\tilde{g}qqq$) states, as well as glueball-like ($\tilde{g}g$) states with probability 10%. The interaction of R-hadrons with the detector material is simulated with GEANT using the model developed in Refs. [15, 16]. However, the results presented in Chap. 5 do not include the model-dependent interactions of R-hadrons. The effect of these interactions will be discussed in Sec. 5.6.

Based on simulation, the estimated number of events of a given process with cross-section σ is given by:

$$\hat{n}_{\text{sim}} = \sigma L \frac{N_{\text{pass}}}{N_{\text{gen}}} \quad (4.7)$$

where L is the integrated luminosity, N_{gen} is the number of events generated, and N_{pass} is the number of events that pass the analysis selections.

4.9. Corrections to simulation

This section describes various ways in which the potential mismodelling of the simulation is corrected for. This usually involves observing a distribution or measuring an efficiency both in data and simulation and applying the data-to-simulation ratio as a weighting factor to each simulated event. These corrections are applied to the simulation of both background and signal processes, as relevant. There are uncertainties associated with each set of correction factors, the treatment of which is detailed in Sec. 4.12.

4.9.1. Pileup

The average number of pileup interactions per bunch crossing during the 2016 run was ~ 20 . The pileup distribution depends on the instantaneous luminosity, which varies over time, and so is not reproduced very accurately by the simulation.

Reweight factors to correct the pileup distribution in the simulation are derived as a function of the number of pileup interactions. The pileup in a given event in data is calculated from the average instantaneous luminosity measured in the corresponding luminosity section, together with the inelastic proton-proton cross section (63 mb [17]). The correction factors are given by the ratio of the pileup distributions in data and simulation. These range between ~ 0.8 -1.2 in the bulk of the distribution. This is illustrated in Fig. 4.7.

4.9.2. Jet energy

The energies of jets are corrected as described in Sec. 3.3.5. In this case, this does not involve a reweighting of the simulated events.

4.9.3. b-tagging

The efficiency for identifying jets as originating from a bottom quark tends to be overestimated in the simulation. Similarly, the probability of incorrectly b-tagging a jet that actually originated from a light flavour (u, d, s) quark or gluon is

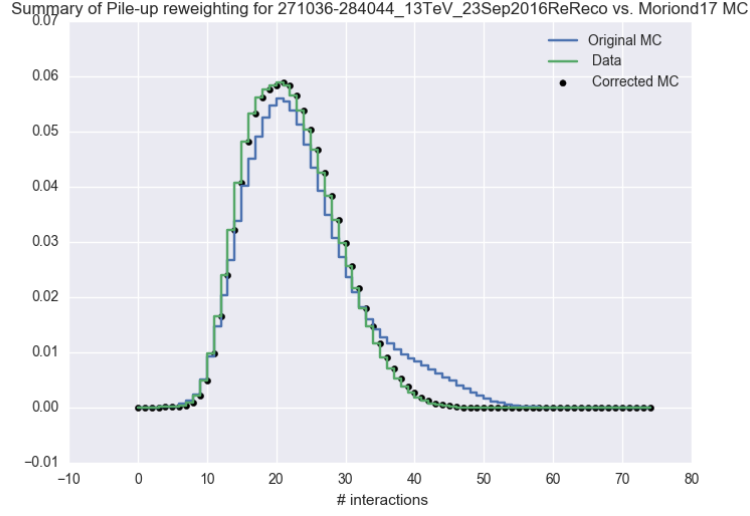


Figure 4.7.: Distribution of the number of pileup interactions in the Monte Carlo (MC) simulation and in data. The ratio of the two is used to derive correction factors that are used to weight the simulated events. The corrected simulated distribution is also shown.

underestimated. Correction factors for the b-tagging efficiency and fake rate are therefore derived, in bins of jet p_T and η , and applied to the simulation.

The b-tagging probability for a jet originating from a quark (or gluon) of flavour q with transverse momentum p_T and pseudorapidity η is estimated as:

$$\varepsilon(p_T, \eta, q) = \frac{N_{\text{b-tagged}}(p_T, \eta, q)}{N_{\text{total}}(p_T, \eta, q)}, \quad (4.8)$$

where $N_{\text{total}}(p_T, \eta, q)$ is the total number of jets of true flavour q in bin (p_T, η) and $N_{\text{b-tagged}}(p_T, \eta, q)$ is the number of such jets that are b-tagged. The flavour q is labelled as one of three types — b, c, or light (u, d, s, or gluon).

In simulated events, the true flavour of a jet is determined according to whether there are any bottom or charmed hadrons contained within the jet's cone. In data, the b-tagging efficiency is measured in a sample of $t\bar{t}$ events or jets containing a muon, and the mistagging probability is measured using jets with a negative impact parameter or negative decay length [18]. The ratio of the b-tagging probability in data and simulation provides a correction factor $f(p_T, \eta, q)$ that is used to weight the events from simulation. The correction factors are in the range ~ 0.95 –1 and ~ 1 –1.2 for bottom quarks and light partons, respectively.

While the correction factors derived in Ref. [18] are for an inclusive set of jets, the b-tagging probabilities are also measured in the signal and control regions of the search. Given these probabilities and the correction factors, for each simulated event the probability of observing the corresponding combination of tagged and non-tagged jets in data and simulation is computed as:

$$P_{\text{sim}} = \prod_{j \text{ b-tagged}} \epsilon_j \prod_{j \text{ not b-tagged}} (1 - \epsilon_j) \quad (4.9)$$

$$P_{\text{data}} = \prod_{j \text{ b-tagged}} f_j \epsilon_j \prod_{j \text{ not b-tagged}} (1 - f_j \epsilon_j) \quad (4.10)$$

where $\epsilon_j \equiv \epsilon(p_T(j), \eta(j), q(j))$ is the probability of jet j being b-tagged, as measured according to Eq. 4.8, and $f_j \equiv f(p_T(j), \eta(j), q(j))$ is the corresponding correction factor. The simulated event is then weighted by the ratio:

$$w = \frac{P_{\text{data}}}{P_{\text{sim}}}. \quad (4.11)$$

Signal models that are simulated via a fast simulation procedure are weighted according to correction factors that are derived to match the b-tagging probability in full simulation, and are then weighted again using the above procedure to match the b-tagging probability in data.

4.9.4. Lepton identification, isolation and triggering

The efficiencies of the muon trigger and the muon identification and isolation requirements described in Sec. 4.1 are corrected for in the simulated events that enter the muon control regions. A similar correction is made for muons and electrons that form part of the ‘lost lepton’ background in the signal region. These efficiencies are measured in data and simulation using the *tag-and-probe method* [19] as explained in the following.

The tag-and-probe method takes advantage of a known mass resonance to identify particles of a desired type and evaluate various efficiency measures such as the ability to reconstruct or trigger such particles. In this case the particles of interest are muons and they are identified via the Z boson resonance. First, a muon that

satisfies stringent quality criteria is selected and labelled as the *tag*. A second muon satisfying looser requirements, labelled the *probe*, is then paired with the tag if it is oppositely charged and the invariant mass of the pair is within a ~ 30 GeV window around the Z boson mass. These requirements on the tag and probe mean that they are almost certainly real muons. It is then checked whether the probe satisfies the selection whose efficiency is of interest. An estimate of the efficiency is given by the fraction of probes that pass the selection. Note that a tag satisfies the probe requirements by definition, and so a dimuon event in which both muons are tagged contains two tag and probe pairs. A tag is not considered if it is paired with more than one probe.

The tag-and-probe efficiency estimate is slightly biased to a lower value than the true efficiency. This is because in events in which there is a tag and a ‘passing’ probe that does not also satisfy the tag requirements, the tag is not counted towards the efficiency. However, the efficiency estimate is also biased higher because the method does not count events in which neither muon is a tag, as well as events in which the second muon does not even satisfy the probe requirements. Overall, the estimated efficiency is typically within $\sim 1\%$ of the true efficiency, and the bias is expected to be negligible in the data-to-simulation correction factors, as the bias largely cancels out in the ratio.

A muon is labelled as a tag if it satisfies the stringent quality criteria described in Sec. 4.1 and is also reconstructed at the trigger level and fires the muon trigger. The latter is determined by attempting to match the offline muon to an HLT muon within a cone of size $\Delta R = 0.3$ and checking whether the matched trigger object satisfies the trigger requirements. The requirements on the probe depend on the particular measurement being made. The three measurements of identification, isolation and trigger efficiency are performed sequentially such that the probe requirements for one measurement are the same as those for a passing probe in the previous measurement. This is done because the overall efficiency is given by the product of conditional probabilities:

$$\epsilon_{\text{ID,iso,trig}} = \epsilon_{\text{ID}} \epsilon_{\text{iso}|\text{ID}} \epsilon_{\text{trig}|\text{ID,iso}}. \quad (4.12)$$

When measuring the identification efficiency, the probe is taken as any reconstructed track, and the passing requirement is that it satisfies the muon quality criteria of Sec. 4.1 except for the isolation requirement. These are then the require-

ments for a probe in the isolation efficiency measurement, and the probe in this case is checked to satisfy the $I^{\text{rel}} < 0.1$ requirement. These are then the input probes for the trigger efficiency measurement, and it is checked whether they cause the muon trigger to fire.

A small amount of combinatoric and fake muon background is present when selecting tag and probe pairs. This background is subtracted and the efficiency extracted via an extended simultaneous maximum likelihood fit to the invariant mass distributions of the passing and failing probes. The two mass distributions are modelled, respectively, by the following probability densities:

$$p_{\text{pass}}(m) = \left(\frac{\varepsilon s}{\varepsilon s + b_{\text{pass}}} \right) p_{\text{pass}}^{\text{sig}}(m) + \left(\frac{b_{\text{pass}}}{\varepsilon s + b_{\text{pass}}} \right) p_{\text{pass}}^{\text{bkg}}(m) \quad (4.13)$$

$$p_{\text{fail}}(m) = \left(\frac{(1 - \varepsilon)s}{(1 - \varepsilon)s + b_{\text{fail}}} \right) p_{\text{fail}}^{\text{sig}}(m) + \left(\frac{b_{\text{fail}}}{(1 - \varepsilon)s + b_{\text{fail}}} \right) p_{\text{fail}}^{\text{bkg}}(m) \quad (4.14)$$

where ε is the efficiency parameter; s , b_{pass} and b_{fail} are the total number of events attributed to signal, background passing probes and background failing probes; and $p_{\text{pass}}^{\text{sig}}$, $p_{\text{pass}}^{\text{bkg}}$, $p_{\text{fail}}^{\text{sig}}$ and $p_{\text{fail}}^{\text{bkg}}$ are the signal and background probability densities for passing and failing probes. The signal is usually modelled by a Voigtian distribution, which is a Breit-Wigner distribution convoluted with a Gaussian distribution to account for smearing due to detector resolution, while the background is usually modelled by an exponential distribution. The extended likelihood function can then be written as:

$$\mathcal{L} = \mathcal{P}(\varepsilon s + b_{\text{pass}}) \mathcal{P}((1 - \varepsilon)s + b_{\text{fail}}) \prod_{i \text{ pass}} p_{\text{pass}}(m_i) \prod_{i \text{ fail}} p_{\text{fail}}(m_i), \quad (4.15)$$

where the products are over all corresponding probes i , and the \mathcal{P} 's are Poisson distributions for the total number of passing and failing events observed. An example of the fitting result in data is shown in Fig. 4.8.

The efficiencies and corresponding data-to-simulation corrections are derived as a function of muon p_T and η . The identification efficiency is around 97-99% and the corresponding correction factors are in the range 0.97-0.99. The efficiency of the isolation requirement varies between 90-99% and the correction factors are around 0.99-1. The trigger efficiency is measured to be approximately 90%, with correction

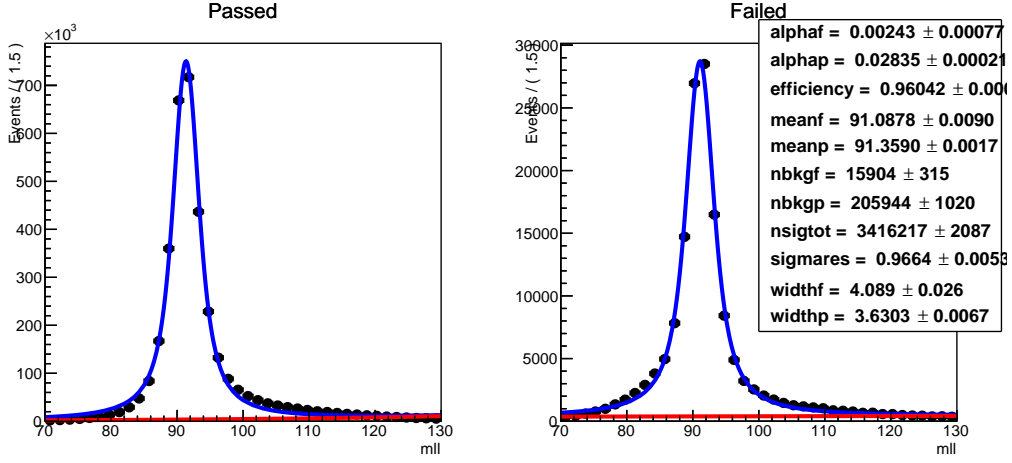


Figure 4.8.: Result of the tag-and-probe dimuon invariant mass fitting procedure to passing (left) and failing (right) probes for an example isolation efficiency measurement in data for muons with $50 < p_T < 60$ GeV. The blue (red) curves are the fitted signal (background) distributions. The fitted efficiency in this example is 96.0%.

factors of about 0.98. In the $\mu\mu + \text{jets}$ control region, the trigger efficiency is higher, as the probability to trigger on at least one muon is $\approx 1 - (1 - 0.9)(1 - 0.9) = 99\%$.

The efficiencies and correction factors are then propagated to the simulated events as follows. The expected number of events in the $\mu + \text{jets}$ control region according to the simulation, ignoring the normalisation due to integrated luminosity and cross section, is given by:

$$N_{\mu+\text{jets}} = \sum a_\mu \varepsilon_{\text{ID}}^\mu \varepsilon_{\text{iso}}^\mu \varepsilon_{\text{trig}}^\mu, \quad (4.16)$$

where the sum runs over all simulated $W(\rightarrow \ell\nu) + \text{jets}$ and $t\bar{t}$ events that contain one generator-level muon satisfy the $\mu + \text{jets}$ control region selections except those relating to the muon acceptance, identification, isolation and trigger. The acceptance term a_μ is either one if the muon satisfies the p_T and η acceptance requirements, or zero if it does not. The efficiency terms are conditional on one another as defined in Eq. 4.12, and their values depend on the muon's p_T and η . Similarly, the number of events in the $\mu\mu + \text{jets}$ control region is given by:

$$N_{\mu\mu+\text{jets}} = \sum (a_{\mu_1} a_{\mu_2}) (\varepsilon_{\text{ID}}^{\mu_1} \varepsilon_{\text{ID}}^{\mu_2}) (\varepsilon_{\text{iso}}^{\mu_1} \varepsilon_{\text{iso}}^{\mu_2}) [1 - (1 - \varepsilon_{\text{trig}}^{\mu_1})(1 - \varepsilon_{\text{trig}}^{\mu_2})], \quad (4.17)$$

where the sum is now over all simulated $Z(\rightarrow \mu\mu) + \text{jets}$ and $t\bar{t}$ events that have two generator-level muons and satisfy the $\mu\mu + \text{jets}$ control region selections except

those relating to the muon acceptance, identification, isolation and trigger. The number of lost lepton background events in the signal region is given by:

$$N_{\text{signal}} = \sum \left[(1 - a_\mu) + a_\mu(1 - \epsilon_{\text{ID}}^\mu) + a_\mu \epsilon_{\text{ID}}^\mu(1 - \epsilon_{\text{iso}}^\mu) + a_\mu \epsilon_{\text{ID}}^\mu \epsilon_{\text{iso}}^\mu(1 - \epsilon_{\text{trig}}^\mu) \right], \quad (4.18)$$

where the sum runs over all simulated $W(\rightarrow \ell\nu) + \text{jets}$ and $t\bar{t}$ events that contain one generator-level muon or electron and satisfy the signal region selections except those relating to the lepton acceptance, identification, isolation and trigger. The efficiencies in these three equations are scaled by the data-to-simulation correction factors derived from the tag-and-probe method to obtain the corrected number of leptonic standard model events in the signal and control regions.

4.9.5. Trigger

Unlike the muon triggers, the signal region triggers are not emulated in the simulation. Instead of determining data-to-simulation correction factors, the trigger efficiencies measured in data as a function of H_T and \cancel{H}_T using an electron reference sample (as described in Sec. 4.7) are themselves applied as corrections. As seen in Fig. 4.5, these can be as low as 90% at low \cancel{H}_T , but are close to unity for $\cancel{H}_T > 300$ GeV.

4.9.6. Theoretical calculation of V+jets production

As mentioned in Sec. 4.8.2, the simulation samples for the vector boson production processes, namely $Z + \text{jets}$ and $W + \text{jets}$, are generated at leading order, as this allows a larger number of events to be simulated. The samples are corrected for missing higher order terms in the matrix element calculations as a function of the boson's transverse momentum. This is done by deriving NLO QCD correction factors using MADGRAPH5, and NLO electroweak correction factors from theoretical calculations [20]. The combined NLO QCD+EW corrections range from approximately 1.4 at a boson p_T of 200 GeV to 0.9 at 800 GeV, for both the $Z + \text{jets}$ and $W + \text{jets}$ processes.

4.9.7. Initial state radiation in $t\bar{t}$ events

Simulated events of the $t\bar{t}$ background process are weighted to improve the agreement with data of the multiplicity of jets from initial state radiation. The data-to-simulation correction factors are derived as a function of the number of ISR jets in an event, and take on values between 0.92 and 0.51 for an ISR multiplicity of 1 and 6, respectively.

4.9.8. Cross-sections

Although the dominant standard model background processes are normalised using the most accurate cross section calculations available (using NLO or NNLO precision), the finite perturbative order combined with the high H_T and \cancel{E}_T selections means that the overall simulated yields of the SM processes in the search regions are not in agreement with those in data.

Corrections to the cross sections of the dominant background processes, namely $Z + \text{jets}$, $W + \text{jets}$ and $t\bar{t}$, that are appropriate for the phase space covered by the search, are derived in a sideband of the $\mu + \text{jets}$ and $\mu\mu + \text{jets}$ control regions defined by a selection of $100 < \cancel{H}_T < 200$ GeV. The two \cancel{H}_T sidebands are binned in n_{jet} , n_b and H_T identically to their control region counterparts. The procedure is done after all other corrections to the simulation samples have been applied.

As the background composition in the signal and control regions is similar, these cross section corrections have a very small effect on the background estimations as they cancel out in the simulation-based transfer factor ratios (explained in Sec. 4.10.1). However, this is not the case for some of the tests that are used to derived systematic uncertainties (which will be described in Sec. 4.12.2) and so the lack of corrections would unnecessarily inflate these uncertainties.

In order to extract the cross section correction factors, a simultaneous binned maximum likelihood fit is performed over both \cancel{H}_T sideband regions, in which the three correction parameters (one for each of the $Z + \text{jets}$, $W + \text{jets}$ and $t\bar{t}$ processes) are freely floating such that they modify the simulated yields to give the best

agreement with those in data. The likelihood function is given by:

$$\mathcal{L} = \mathcal{U}(f_W)\mathcal{U}(f_Z)\mathcal{U}(f_{t\bar{t}}) \prod_{b \text{ } (\mu + \text{jets})} \mathcal{P}\left(f_W \lambda_W^b + f_{t\bar{t}} \lambda_{t\bar{t}}^b\right) \prod_{b \text{ } (\mu\mu + \text{jets})} \mathcal{P}\left(f_Z \lambda_Z^b + f_{t\bar{t}} \lambda_{t\bar{t}}^b\right) \quad (4.19)$$

where the λ^b 's are the number of background events in an $(n_{\text{jet}}, n_b, H_T)$ bin b given by the simulation for a given standard model process, the f 's are the cross section correction factors, the \mathcal{U} 's define a uniform distribution for the correction parameters, and the \mathcal{P} 's define a Poisson distribution in each bin.

The cross section correction factors for the $Z + \text{jets}$, $W + \text{jets}$ and $t\bar{t}$ processes are mainly constrained, respectively, by the $\mu\mu + \text{jets}$ sideband, the $\mu + \text{jets}$ sideband, and a combination of the two sidebands. The values of the correction factors obtained from the fit are given in Tab. 4.8.

Table 4.8.: Cross section correction factors for the three dominant standard model background processes, along with an indication of the most constraining sideband region for each process.

SM process	Sideband region	Correction factor
$Z + \text{jets}$	$\mu\mu + \text{jets}$	$f_Z = 0.91$
$W + \text{jets}$	$\mu + \text{jets}$	$f_W = 1.06$
$t\bar{t}$	$\mu + \text{jets}, \mu\mu + \text{jets}$	$f_{t\bar{t}} = 0.93$

4.9.9. Statistical precision at large n_b

The following describes a method by which the statistical precision of the background simulation samples in the high n_b bins is improved. This is particularly useful for the $n_b \geq 3$ region, which is populated by standard model processes through the incorrect tagging of light flavour jets as b-jets, mainly $t\bar{t}$ events in which the two b-jets from the top quarks are correctly tagged and an additional jet is mistagged. As the mistagging probability is quite small, the number of such events in simulation is limited. Reducing the statistical uncertainty on the expected standard model background in the high n_b region helps to improve the sensitivity

of the search to SUSY processes involving the production of multiple heavy quarks, as well as processes containing displaced jets, as will be seen in Chap. 5.

First, the b-tagging probabilities for bottom, charm and light flavour jets ($\varepsilon_b, \varepsilon_c, \varepsilon_l$) are computed in simulation in bins of $(n_{\text{jet}}, H_T, \cancel{H}_T)$, after applying the p_T and η dependent correction weights described in Sec. 4.9.3. For a given number of jets n_q^{gen} of underlying flavour q (as determined by generator-level information), the number of such jets that are b-tagged n_q^{tag} follows a binomial distribution with probability parameter ε_q , $P(n_q^{\text{tag}}|n_q^{\text{gen}}, \varepsilon_q)$. For an event containing a particular combination of underlying jet flavours $(n_b^{\text{gen}}, n_c^{\text{gen}}, n_l^{\text{gen}})$, the probability of observing a combination of b-tagged jets $(n_b^{\text{tag}}, n_c^{\text{tag}}, n_l^{\text{tag}})$ is given by the product:

$$P(n_b^{\text{tag}}, n_c^{\text{tag}}, n_l^{\text{tag}}|n_b^{\text{gen}}, n_c^{\text{gen}}, n_l^{\text{gen}}) = P(n_b^{\text{tag}}|n_b^{\text{gen}}, \varepsilon_b) P(n_c^{\text{tag}}|n_c^{\text{gen}}, \varepsilon_c) P(n_l^{\text{tag}}|n_l^{\text{gen}}, \varepsilon_l). \quad (4.20)$$

If there are $N(n_b^{\text{gen}}, n_c^{\text{gen}}, n_l^{\text{gen}})$ simulation events of a particular process with such combination of underlying jet flavour, the number of these events that result in a combination of b-tagged jets $(n_b^{\text{tag}}, n_c^{\text{tag}}, n_l^{\text{tag}})$ follows a binomial distribution with the above probability, with an expected value of:

$$E[N(n_b^{\text{tag}}, n_c^{\text{tag}}, n_l^{\text{tag}}|n_b^{\text{gen}}, n_c^{\text{gen}}, n_l^{\text{gen}})] = N(n_b^{\text{gen}}, n_c^{\text{gen}}, n_l^{\text{gen}}) P(n_b^{\text{tag}}, n_c^{\text{tag}}, n_l^{\text{tag}}|n_b^{\text{gen}}, n_c^{\text{gen}}, n_l^{\text{gen}}). \quad (4.21)$$

The total expected number of events containing n_b b-tagged jets in a given $(n_{\text{jet}}, H_T, \cancel{H}_T)$ bin is then the sum of this expected value over all combinations of underlying jet flavours that sum to n_{jet} and all combinations of b-tagged jets that sum to n_b :

$$N(n_b) = \sum_{n_b^{\text{gen}} + n_c^{\text{gen}} + n_l^{\text{gen}} = n_{\text{jet}}} \sum_{n_b^{\text{tag}} + n_c^{\text{tag}} + n_l^{\text{tag}} = n_b} E[N(n_b^{\text{tag}}, n_c^{\text{tag}}, n_l^{\text{tag}}|n_b^{\text{gen}}, n_c^{\text{gen}}, n_l^{\text{gen}})]. \quad (4.22)$$

The strength of the method comes from a more effective utilisation of all simulated events. Each simulated event, rather than resulting in one particular $(n_b^{\text{tag}}, n_c^{\text{tag}}, n_l^{\text{tag}})$ realisation, contributes to the estimation of the yield in multiple n_b bins. The statistical uncertainties in the highest n_b bins are found to be approximately three times smaller than those obtained directly from the simulated events. As a means

of validation, it is checked that the yields estimated with this method are consistent with those obtained directly from simulation.

Throughout the remainder of the thesis, all simulation-based event yields are obtained via this method. Similarly, all references to simulated events assume the inclusion of all the corrections described in this section.

4.10. Estimation of electroweak background processes

An accurate knowledge of the expected number of standard model background events is very important when searching for new physics. Relying on simulation, even after applying the corrections discussed in the previous section, would introduce a bias in the background estimation due to imperfect modelling. A data-driven approach is therefore utilised which combines simulated events and control region data to perform a more accurate estimation.

This section describes the methods of background estimation for the processes with genuine \cancel{E}_T , which involves an estimation per $(n_{\text{jet}}, n_b, H_T)$ bin and another one for the \cancel{H}_T bins within each $(n_{\text{jet}}, n_b, H_T)$ bin. The estimation of the much smaller QCD background will be discussed in Sec. 4.11.

4.10.1. The n_{jet} , n_b and H_T dimensions

The number of background events in each $(n_{\text{jet}}, n_b, H_T)$ bin is estimated using the muon control regions. As mentioned in Sec. 4.5.2 and 4.6, these are chosen to be enriched in the background processes they are trying to estimate and are binned identically in $(n_{\text{jet}}, n_b, H_T)$ (with the exception of the n_b dimension in the $\mu\mu + \text{jets}$ sample). The $\mu\mu + \text{jets}$ control region is used to estimate the $Z(\rightarrow \nu\nu) + \text{jets}$ background, while the $\mu + \text{jets}$ control region is used to estimate the sum of the $W(\rightarrow \ell\nu) + \text{jets}$, $t\bar{t}$ and residual backgrounds, which will be collectively labelled as $W/t\bar{t}$.

The estimated number of events of a given background process in a particular $(n_{\text{jet}}, n_b, H_T)$ bin is related to the total number of events in the same bin of the corresponding control region in data $N_{\text{control}}^{\text{data}}(n_{\text{jet}}, n_b, H_T)$ and simulation $N_{\text{control}}^{\text{sim}}(n_{\text{jet}}, n_b, H_T)$ and the number of events of that background in the same bin of the signal region

in simulation $N_{\text{signal}}^{\text{sim}}(n_{\text{jet}}, n_{\text{b}}, H_{\text{T}})$ by:

$$\hat{N}_{\text{signal}}(n_{\text{jet}}, n_{\text{b}}, H_{\text{T}}) = \frac{N_{\text{signal}}^{\text{sim}}(n_{\text{jet}}, n_{\text{b}}, H_{\text{T}})}{N_{\text{control}}^{\text{sim}}(n_{\text{jet}}, n_{\text{b}}, H_{\text{T}})} N_{\text{control}}^{\text{data}}(n_{\text{jet}}, n_{\text{b}}, H_{\text{T}}). \quad (4.23)$$

A special case of this formula applies to the $Z(\rightarrow \nu\nu) + \text{jets}$ process in the $n_{\text{b}} = 1, 2, 3$ and ≥ 4 bins, which is estimated in each of these bins using the $n_{\text{b}} \geq 1$ bin in the $\mu\mu + \text{jets}$ control region.

The extrapolation from the control region to the signal region is performed via the simulation-based ratio of yields in the above equation, referred to as a *transfer factor*:

$$T(n_{\text{jet}}, n_{\text{b}}, H_{\text{T}}) = \frac{N_{\text{signal}}^{\text{sim}}(n_{\text{jet}}, n_{\text{b}}, H_{\text{T}})}{N_{\text{control}}^{\text{sim}}(n_{\text{jet}}, n_{\text{b}}, H_{\text{T}})}. \quad (4.24)$$

The transfer factor can be viewed as a way of accounting for the different branching fraction, acceptance and identification efficiency of a given process between the signal and control region. For instance, the Z boson's branching ratio between neutrinos and muons is 9, and unlike the weakly interacting neutrinos, the muons are subject to acceptance and identification requirements. The transfer factor also accounts for the different kinematic selections, namely on α_{T} and $\Delta\phi_{\text{min}}^*$, which are not used in the control regions. The transfer factors used in the estimations of the $W/\text{t}\bar{\text{t}}$ background from the $\mu + \text{jets}$ control region and the $Z(\rightarrow \nu\nu) + \text{jets}$ background from the $\mu\mu + \text{jets}$ control region are denoted as $T(\mu \rightarrow W/\text{t}\bar{\text{t}})$ and $T(\mu\mu \rightarrow Z)$, respectively.

Equivalently, the estimation in Eq. 4.23 can also be viewed as a way of correcting the number of events obtained from the simulation according to the data-to-simulation discrepancy ratio in the control region bin:

$$\hat{N}_{\text{signal}}(n_{\text{jet}}, n_{\text{b}}, H_{\text{T}}) = \frac{N_{\text{control}}^{\text{data}}(n_{\text{jet}}, n_{\text{b}}, H_{\text{T}})}{N_{\text{control}}^{\text{sim}}(n_{\text{jet}}, n_{\text{b}}, H_{\text{T}})} N_{\text{signal}}^{\text{sim}}(n_{\text{jet}}, n_{\text{b}}, H_{\text{T}}). \quad (4.25)$$

This highlights the importance of having similar kinematic requirements and background compositions, as well as a similar binning scheme, in the control and signal regions, as the discrepancy between data and simulation in a given bin of the

control region is likely to be similar to that in the corresponding bin in the signal region.

Although the $\mu\mu + \text{jets}$ control region is binned more inclusively in the n_b variable than the signal region (which for $n_b \geq 1$ is equivalent to taking the shape of the n_b distribution directly from simulation), it is checked that this does not bias the background estimation in a similar way as the validation of the \cancel{H}_T dimension, which will be discussed in the next section.

The transfer factors, and therefore the background estimates, are robust against many sources of systematic effects relating to kinematic mismodelling and theoretical uncertainties, as these cancel out in the transfer factor ratio to a large extent. Several sources of systematic uncertainty are nevertheless accounted for in the estimated backgrounds, as will be discussed in Sec. 4.12.

4.10.2. The \cancel{H}_T dimension

The transfer factor method just described is used to estimate the expected number of background events in each $(n_{\text{jet}}, n_b, H_T)$ bin, inclusive with respect to \cancel{H}_T . The method could be applied to the estimation of each $(n_{\text{jet}}, n_b, H_T, \cancel{H}_T)$ bin; however, the additional binning in the \cancel{H}_T dimension that would be required in the control regions would greatly reduce the number of events in each control region bin (the ‘curse of dimensionality’). This would cause the statistical uncertainty in the estimated background to be too large and degrade the sensitivity of the search. Instead, the number of background events in each \cancel{H}_T bin within a given $(n_{\text{jet}}, n_b, H_T)$ bin is estimated according to the \cancel{H}_T distribution obtained directly from simulation. In other words, the *shape* of the \cancel{H}_T distribution in each $(n_{\text{jet}}, n_b, H_T)$ is taken from simulation, while the *normalisation* of the distribution is obtained via the transfer factor method.

It is important to assess whether there is a potential bias in the background estimation due to the direct use of simulated events. This is done by comparing the \cancel{H}_T distributions in every $(n_{\text{jet}}, n_b, H_T)$ bin between data and simulation in the two muon control regions. Only the shapes are compared, as the normalisation is determined using the data-driven transfer factor method. If the simulation’s modelling of the \cancel{H}_T shape is reasonable, the ratio of events between data and simulation in each \cancel{H}_T bin is expected to be unity.

A linear model is fit to the data-to-simulation ratio versus \cancel{H}_T using a χ^2 minimisation procedure, and it is checked that the estimated value of the linear parameter is statistically compatible with zero. This is done for all $(n_{\text{jet}}, n_b, H_T)$ bins by computing the z-score, which is given by the value of the linear parameter divided by its uncertainty. The result of the fit for two example $(n_{\text{jet}}, n_b, H_T)$ bins is shown in Fig. 4.9. Figure 4.10 shows the distribution of the linear parameter's z-score over all $(n_{\text{jet}}, n_b, H_T)$ bins. It can be seen that the z-scores are approximately Gaussian distributed with a mean and standard deviation compatible with zero and one, respectively. Performing the background estimation in the \cancel{H}_T dimension using the distributions obtained directly from simulation is therefore considered valid.

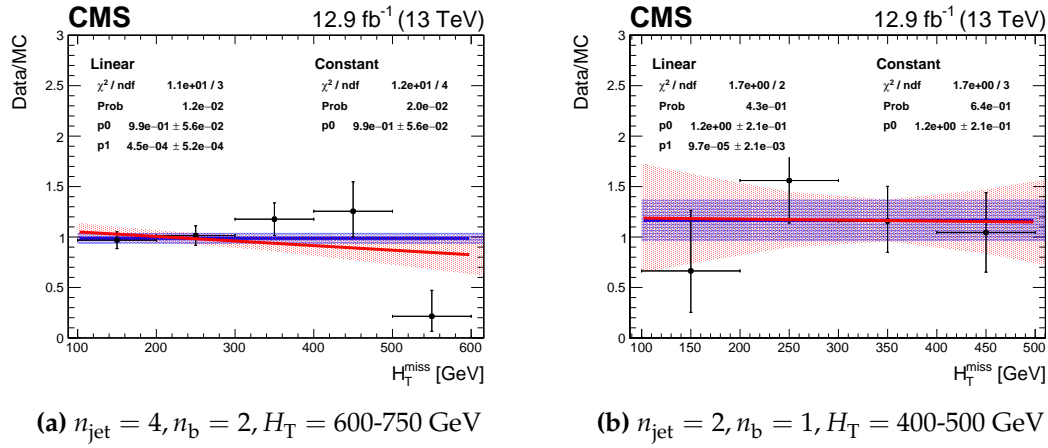


Figure 4.9.: The data-to-simulation ratio of event counts as a function of \cancel{H}_T for two example $(n_{\text{jet}}, n_b, H_T)$ categories, along with the fit of a linear (and constant) function.

The uncertainties on the linear fits are used to assign systematic uncertainties on these simulated \cancel{H}_T distributions, as will be discussed in Sec. 4.12.3.

4.11. Estimation of QCD background processes

As discussed in Sec. 4.4, the QCD background is very difficult to estimate accurately, and so a choice is made to reduce this background to a very small level by means of dedicated variables such as α_T and $\Delta\phi_{\text{min}}^*$. In this way, a large uncertainty on a small QCD contribution does not have a large negative impact on the search's sensitivity to BSM physics.

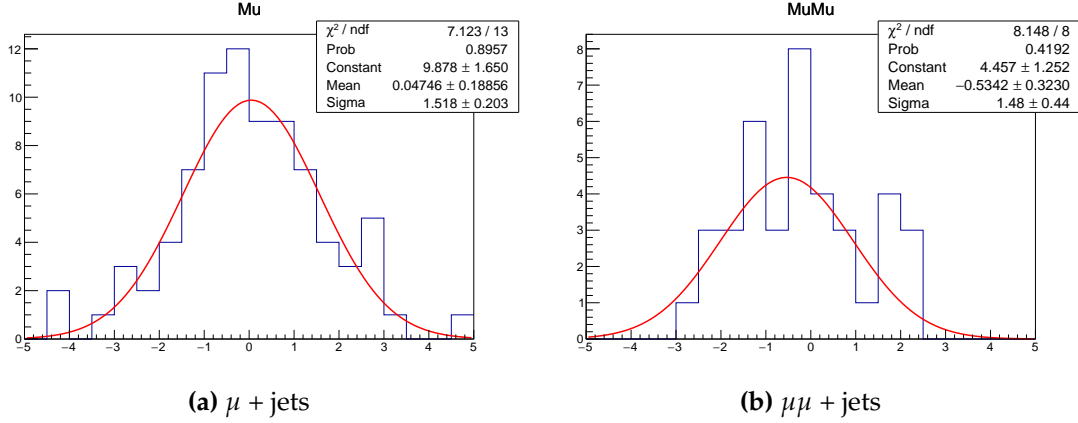


Figure 4.10.: The distribution of the z-scores of the linear parameter fitted to the H_T distributions for all $(n_{\text{jet}}, n_b, H_T)$ categories in both the $\mu + \text{jets}$ and $\mu\mu + \text{jets}$ control regions. A fitted Gaussian distribution is overlaid.

The residual QCD background is estimated in a data-driven way using the hadronic control regions, which are enriched in QCD events, in a similar way as the electroweak background processes. The three hadronic control regions consist of three signal region sidebands with respect to the H_T/E_T and $\Delta\phi_{\text{min}}^*$ variables, as well as a ‘double sideband’ in which the requirements on both H_T/E_T and $\Delta\phi_{\text{min}}^*$ are inverted. These were summarised in Sec. 4.5.2. The estimated QCD yields are checked to be consistent between the three sidebands, and the final estimate is taken as the average of all three weighted by their uncertainties.

The QCD background estimation is performed in a similar way as the electroweak background estimation, namely via the transfer factor method described in Sec. 4.10. In this case, because of the statistical limitation of the QCD simulation samples, only the normalisation per (n_{jet}, H_T) bin, rather than per $(n_{\text{jet}}, n_b, H_T)$ bin, is estimated from the control regions. The (n_b, H_T) dimension is treated differently, as will be discussed later in this section. Analogously to Eq. 4.23, the transfer factor equation is given by:

$$\hat{N}_{\text{signal}}(n_{\text{jet}}, H_T) = \frac{N_{\text{signal}}^{\text{sim}}(n_{\text{jet}}, H_T)}{N_{\text{control}}^{\text{sim}}(n_{\text{jet}}, H_T)} \hat{N}_{\text{control}}^{\text{data}}(n_{\text{jet}}, H_T). \quad (4.26)$$

where $N_{\text{signal}}^{\text{sim}}(n_{\text{jet}}, H_T)$ and $N_{\text{control}}^{\text{sim}}(n_{\text{jet}}, H_T)$ are the number of simulated QCD events in bin (n_{jet}, H_T) in the signal region and sideband, and $\hat{N}_{\text{control}}^{\text{data}}(n_{\text{jet}}, H_T)$ is the estimated number of QCD events in the same sideband bin in data. There is a non-

negligible contribution from electroweak processes in the sideband, and so instead of using the total number of events in the hadronic control region (as in Eq. 4.23), only the number of events from QCD processes is used. This is done by estimating the electroweak background in the hadronic sideband via sidebands of the two muon control regions, in exactly the same way as the electroweak background estimation is performed in the signal region via the muon control regions (Sec. 4.10), accounting for the systematic uncertainties that will be discussed in Sec. 4.12. This is subtracted from the total number of events observed in the hadronic sideband to give an estimate of the number of QCD events $\hat{N}_{\text{control}}^{\text{data}}(n_{\text{jet}}, H_T)$.

The results of the QCD background estimation procedure is shown in Fig. 4.11. It can be seen that the number of QCD events in each (n_{jet}, H_T) bin of the signal region is estimated to be very small, and the contribution is less than 1% of the total background composition in most bins of the signal region.

Within each (n_{jet}, H_T) bin, the shape of the distribution of events across n_b and \cancel{H}_T is taken directly from the simulation of the electroweak processes. This is chosen instead of the QCD simulation as the statistical power of the electroweak simulation is much larger. It is checked that the electroweak (n_b, \cancel{H}_T) distribution is consistent with the QCD distribution within uncertainties.

4.12. Uncertainties on background estimation

The electroweak background estimation procedure is subject to both statistical and systematic uncertainties. This section describes the various sources of systematic uncertainty and the methods used to estimate the size of these uncertainties and their effect on the background estimates. The uncertainties are then incorporated into the statistical model employed to determine the sensitivity of the search to BSM physics, as will be explained in Sec. 5.3.

The systematic uncertainties on the electroweak background estimates are broadly encoded in one of two ways – as uncertainties on the transfer factors which determine the number of events in each $(n_{\text{jet}}, n_b, H_T)$ bin, and uncertainties on how these events are distributed across the corresponding \cancel{H}_T bins.

The systematic uncertainties on the transfer factors are determined in two ways. The first concerns theoretical and experimental sources of uncertainty on the correc-

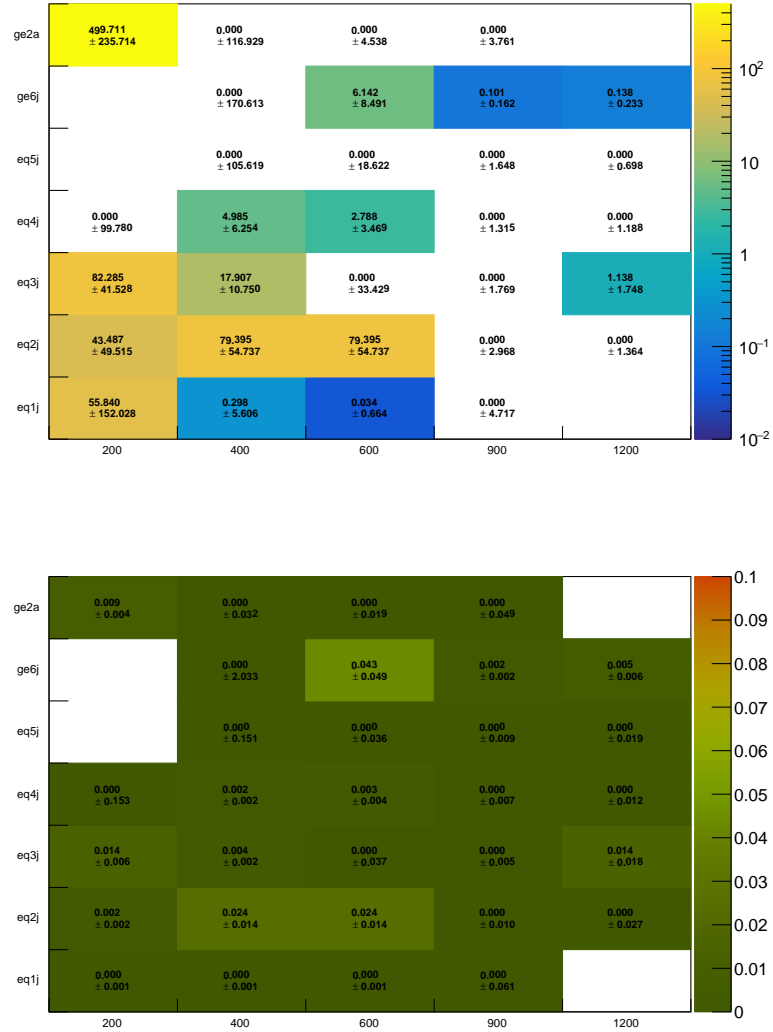


Figure 4.11.: The estimated number of QCD events in each (n_{jet}, H_T) bin of the signal region (top), and the corresponding ratio of expected QCD and electroweak events (bottom).

tions described in Sec. 4.9 that are applied to the simulation. The second concerns potential sources of bias that may arise in the background estimation due to different selections in the signal and control regions.

All of these uncertainties are discussed in the following sub-sections. They are summarised, along with representative sizes in Tab. 4.9.

Source of uncertainty	Uncertainty on transfer factor (%)	
	$T(\mu \rightarrow W/t\bar{t})$	$T(\mu\mu \rightarrow Z)$
Simulation variations		
Pileup	0.6-3.8	2.3-2.8
Jet energy scale	3.4-5.5	5.3-8.0
b-tagging (heavy quark)	0.4-0.6	0.3-0.6
b-tagging (light quark)	0.1-1.4	0.2-1.8
Lepton selection	5	2
Trigger	0.0-3.1	0.0-2.0
ISR	0.8-1.1	0.5-1.0
QCD+EW NLO	0.5-5.4	2.2-14.0
Cross section (W + jets)	0.2-1.4	—
Cross section ($t\bar{t}$)	0.0-1.0	0.0-0.8
Closure tests		
α_T extrapolation	2.7-7.6	3.3-9.4
$\Delta\phi_{\min}^*$ extrapolation	2.1-20.0	2.7-22.0
W^+/W^- extrapolation	1.2-6.6	—

Table 4.9.: Summary of systematic uncertainties on the $T(\mu \rightarrow W/t\bar{t})$ and $T(\mu\mu \rightarrow Z)$ transfer factors, derived from variations of the data-to-simulation correction factors (Sec. 4.12.1) and data-driven closure tests (Sec. 4.12.2). The quoted ranges correspond to the $\pm 1\sigma$ quantiles of the transfer factor changes across all (n_{jet}, n_b, H_T) bins.

4.12.1. Uncertainties derived from variations in simulation

The corrections to the simulation described in Sec. 4.9 have uncertainties associated with them based on the procedures in which they are derived. The effect of these uncertainties is considered both on the transfer factors, which provide the expected normalisation of the backgrounds in each (n_{jet}, n_b, H_T) bin, and the modelling of the \cancel{H}_T distribution within each of these bins. This section focusses on the transfer factors, while the effect on the \cancel{H}_T shape is discussed in Sec. 4.12.3.

In order to determine systematic uncertainties on the transfer factors, the correction factors are varied in turn from their nominal values by one standard deviation up and down, according to their associated uncertainties. The number of simulated events in the signal and control regions is then re-computed under both variations, and the resulting changes in the transfer factors are taken as systematic uncertainties

on the transfer factors. This is done for both the $T(\mu \rightarrow W/\text{t}\bar{\text{t}})$ and $T(\mu\mu \rightarrow Z)$ transfer factors, in every $(n_{\text{jet}}, n_b, H_T)$ bin.

An example of this procedure is shown in Fig. 4.12, which shows the relative change of the transfer factors under variations of the pileup corrections. The effect on the transfer factors due to the other sources of systematic uncertainty is shown in App. A.1. The uncertainties associated with each set of simulation corrections will be discussed further in this section.

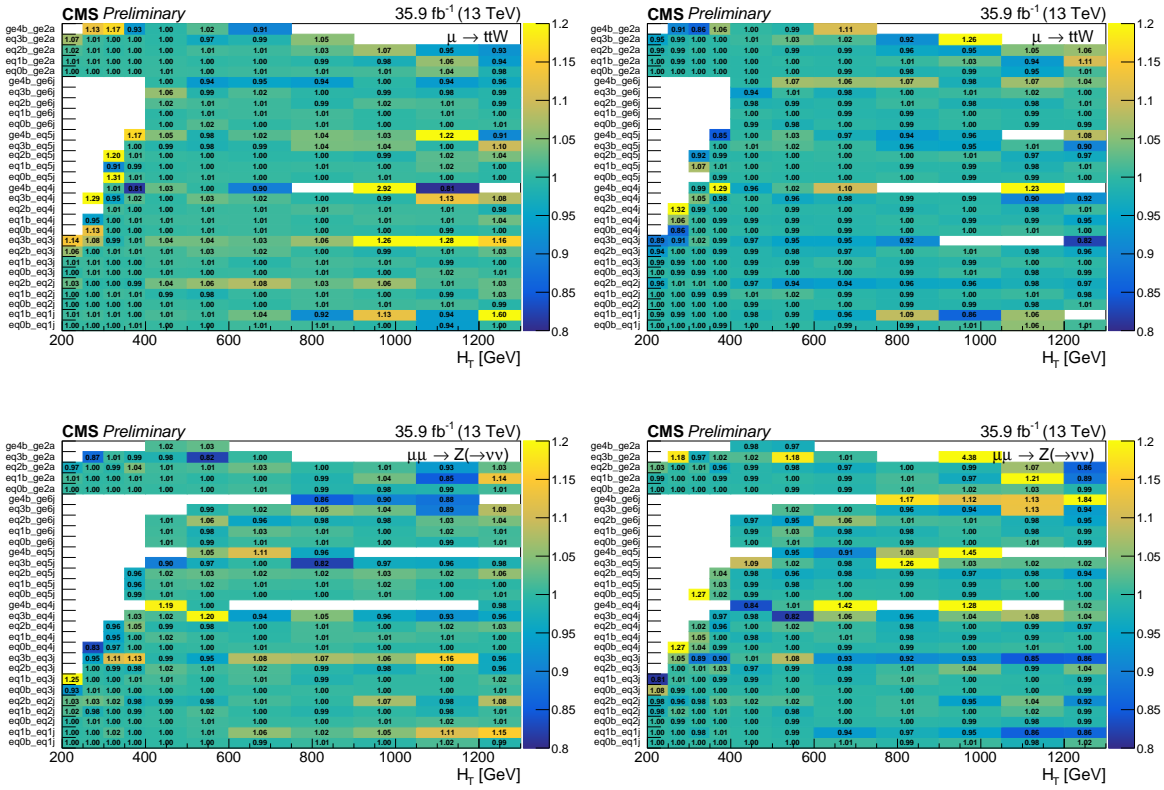


Figure 4.12.: The ratio of the $T(\mu \rightarrow W/\text{t}\bar{\text{t}})$ (top) and $T(\mu\mu \rightarrow Z)$ (bottom) transfer factors in each $(n_{\text{jet}}, n_b, H_T)$ bin when varying the pileup correction factors by $+1\sigma$ (left) and -1σ (right) with respect to their nominal values.

The effect on the transfer factors is usually small, at the level of a few percent change in their value. This is because the kinematics and background composition in equivalent bins of the control and signal region are similar, and so the change of the simulation yields under each variation is also similar, which leads to an almost complete cancellation in the ratio of the transfer factor. The changes can be larger than 10% in certain bins of the search's parameter space that are statistically more limited.

Pileup

Events in the simulation are weighted to correct the pileup distribution as described in Sec. 4.9.1. The measured inelastic proton-proton cross section of 63 mb has an associated uncertainty of 5%. The pileup distribution in data is therefore also constructed using a cross section of 66.15 mb and 59.85 mb, and the pileup weights are re-derived for both variations.

The resulting changes in the transfer factors are typically in the range 0.5 - 4% across the $(n_{\text{jet}}, n_b, H_T)$ bins. This is shown in Fig. A.1

Jet energy scale

The energies of jets are corrected as a function of their transverse momentum and pseudorapidity as described in Secs. 3.3.5 and 4.9.2.

When varying the jet energy corrections in simulation by 1σ up and down, the values of the $T(\mu \rightarrow W/t\bar{t})$ and $T(\mu\mu \rightarrow Z)$ transfer factors are seen to change by approximately 3 - 8% across the $(n_{\text{jet}}, n_b, H_T)$ bins. This is shown in Fig. A.2.

b-tagging

Events in the simulation are weighted to correct for differences in the b-tagging efficiency and mistagging probability with respect to data, as described in Sec. 4.9.3. The measurements of the tagging probabilities for bottom and charm quarks are correlated, and so their uncertainties are varied in conjunction. The uncertainties on the correction factors for light flavour quarks are considered separately.

The changes in the values of the transfer factors under variations of the uncertainties on both the heavy and light flavour b-tagging probabilities are shown in Figs. A.3 and A.4. These are typically quite small, between 0 - 2%.

Lepton identification, isolation and triggering

The efficiencies of the identification, isolation and trigger requirements for muons and electrons are corrected using the tag-and-probe method discussed in Sec. 4.9.4.

The uncertainties associated with these correction factors are varied by $\pm 1\sigma$ in both the signal and control regions and the transfer factors are recomputed.

The changes of the transfer factors are found to be approximately 2% for $T(\mu\mu \rightarrow Z)$ and 5% for $T(\mu \rightarrow W/t\bar{t})$ across the $(n_{\text{jet}}, n_b, H_T)$ parameter space. The change is larger in the latter case as the lepton efficiencies have an opposite effect in the signal region and $\mu + \text{jets}$ control region. For instance, if the muon efficiency is increased, the number of events in the $\mu + \text{jets}$ control region increases while the number of $W/t\bar{t}$ events in the signal region decreases due to a more efficient vetoing of leptonic events. On the other hand, while the yields in the $\mu\mu + \text{jets}$ control region increase, the numerator of the $T(\mu\mu \rightarrow Z)$ transfer factor is unaffected as the lepton efficiency is irrelevant for the $Z(\rightarrow \nu\nu) + \text{jets}$ process.

Trigger

As mentioned in Sec. 4.9.5, simulated events in the signal region are corrected to account for the efficiency of the combined suite of $H_T - \alpha_T$, $E_T - \cancel{H}_T$, and pure H_T triggers. The nominal values of the correction factors are taken from the efficiencies measured with the electron reference sample. The differences with respect to the efficiencies measured with the muon reference sample are assigned as systematic uncertainties on the correction factors.

The differences are around 5% in the turn-on region ($\cancel{H}_T \approx 200$ GeV) and are practically zero in the efficiency plateau ($\cancel{H}_T > 300$ GeV). As these corrections are only relevant for events in the signal region and not in the control regions, the resulting changes of the transfer factors are also in this range, as shown in Fig. A.5.

Theoretical calculation of V+jets production

The $Z + \text{jets}$ and $W + \text{jets}$ simulation samples generated at leading order are corrected for NLO effects as a function of boson p_T , as discussed in Sec. 4.9.6. These correction factors are assigned a conservative uncertainty given by the difference of the correction from unity. This is defined such that a variation of -1σ is equivalent to not applying such corrections, and a $+1\sigma$ is equivalent to applying them twice.

The effect on the transfer factors is found to be small at low values of H_T . At high H_T , they can be smaller than the equivalent transfer factors without NLO

corrections by up to $\sim 10\%$, as seen in Fig. A.6. This is due to a larger Lorentz boost that is implicitly imposed on the bosons by the $\Delta\phi_{\min}^* > 0.5$ requirement in the signal region compared to the control regions in which such requirement is not made. Thus, because the NLO correction factors are decreasing with boson p_T , events in the signal region are typically subjected to slightly smaller corrections.

Initial state radiation in $t\bar{t}$ events

Uncertainties in the correction derived to improve the distribution of the number of ISR jets, described in Sec. 4.9.7, are also considered. The correction factors are assigned an uncertainty given by half the difference of the correction from unity.

Although the uncertainties on the correction factors are relatively large, the effect on the transfer factors is small, at the level of 1%, as shown in Fig. A.7. This is expected as the signal and control regions are categorised identically in the number of jets, which leads to a cancellation in the transfer factors.

Cross sections

The cross sections of the main standard model background processes are corrected according to the \cancel{H}_T sideband method described in Sec. 4.9.8. Given a similar background composition between the signal and control regions, these are expected to have a small effect on the transfer factors. The $T(\mu \rightarrow W/t\bar{t})$ transfer factors are potentially most sensitive to uncertainties in the cross sections in bins in which there is a mixture of $W(\rightarrow \ell\nu) + \text{jets}$ and $t\bar{t}$ events, as the relative composition of each process may be different in the signal and control regions due to different kinematic selections ($\alpha_T, \Delta\phi_{\min}^*, M_T$). It is checked whether the transfer factors are indeed sensitive to this by varying the $W + \text{jets}$ and $t\bar{t}$ cross sections in turn by twice their uncertainties as measured by the CMS experiment. The changes in the transfer factors are then assigned as systematic uncertainties on their values.

The variations on the $T(\mu \rightarrow W/t\bar{t})$ transfer factors is shown in Figs. A.8 and A.9 as a function of $(n_{\text{jet}}, n_b, H_T)$. The changes are found to be relatively small, with values between 0-2%.

4.12.2. Uncertainties derived from data-driven closure tests

Further sources of systematic uncertainty on the transfer factors are considered in addition to those related to the data-to-simulation correction factors described in the previous section. The transfer factors may be biased as a result of different kinematic selections in the signal and control regions, as well as slightly different background compositions. The transfer factors are probed for potential bias via a series of *closure tests*, in which a control (sub-)region is used to estimate the number of events in another control (sub-)region rather than the signal region.

In an analogous way to the signal region background estimation (Eq. 4.23), the number of observed events in a control sub-sample A is used to estimate the number of events in a control sub-sample B via a transfer factor involving the corresponding event yields in simulation:

$$\hat{N}_B = \frac{N_B^{\text{sim}}}{N_A^{\text{sim}}} N_A^{\text{data}}. \quad (4.27)$$

The estimated number of events is then compared to the observed number of events in control sub-region B, and the level of closure (or rather, non-closure) is measured by the quantity:

$$C(A \rightarrow B) = \frac{N_B^{\text{data}} - \hat{N}_B}{\hat{N}_B}. \quad (4.28)$$

The deviation of this quantity from zero, with its uncertainty added in quadrature, is then assigned as a systematic uncertainty on the relevant transfer factor. The closure tests are performed, in turn, as a function of H_T and n_{jet} . The various closure tests employed to probe different sources of potential bias are discussed in this section.

To avoid double counting the uncertainties due to the simulation correction factors and thereby inflating the systematic uncertainties derived from the closure tests, the estimation in Eq. 4.27 is performed via a maximum likelihood fit, similar to the one that will be discussed in Sec. 5.3, in which the data-to-simulation correction factor uncertainties are included.

Extrapolation in the α_T and $\Delta\phi_{\min}^*$ requirements

Unlike in the signal region, no requirements are made on the α_T and $\Delta\phi_{\min}^*$ variables on events in the muon control regions. A mismodelling of these variables in the simulation may therefore introduce a bias in the transfer factors.

To test this, closure tests are performed in which events in the $\mu + \text{jets}$ control region with values of α_T ($\Delta\phi_{\min}^*$) below a certain threshold are used to estimate the number of events in the $\mu + \text{jets}$ control region with values of α_T ($\Delta\phi_{\min}^*$) larger than the same threshold. The thresholds are chosen according to the $\Delta\phi_{\min}^*$ and H_T -dependent selections mentioned in Sec. 4.5. The test is performed in the $\mu + \text{jets}$ control region as it is statistically more powerful than the $\mu\mu + \text{jets}$ control region.

The results of these closure tests are shown in Fig. 4.13. The resulting systematic uncertainties are found to be in the range $\sim 3\text{--}10\%$. These uncertainties are assigned to both the $T(\mu \rightarrow W/t\bar{t})$ and $T(\mu\mu \rightarrow Z)$ transfer factors. To avoid double counting the α_T and $\Delta\phi_{\min}^*$ uncertainties as the variables are somewhat correlated, the systematic uncertainties are taken from the α_T closure test for the $H_T < 900$ GeV bins and from the $\Delta\phi_{\min}^*$ closure test for the $H_T > 900$ GeV bin.

Extrapolation in the W^+/W^- proportion

W bosons produced at a proton-proton collider are predominantly left-handed, with a polarisation fraction of up to 70% at large transverse momenta [21]. Owing to both the left-handed nature of the weak interaction and angular momentum conservation, this means that a leptonic W^+ decay results in a neutrino travelling in the same direction as the W boson and a lepton travelling in the opposite direction. In a W^- decay, the directions of the (anti-)neutrino and lepton are reversed. The neutrino (lepton) therefore has a larger Lorentz boost in a W^+ (W^-) decay than in a W^- (W^+) decay. As the acceptance of the $\mu + \text{jets}$ control region to W events relies more on the muon p_T , while the signal region relies more on the missing energy, this leads to a larger W^+/W^- fraction in the signal region than in the $\mu + \text{jets}$ control region.

To test whether this introduces a bias in the $T(\mu \rightarrow W/t\bar{t})$ transfer factor, a closure test is performed within the $\mu + \text{jets}$ control region in which a sample of W^+ events is used to estimate the number of W^- events. The results of this closure test are

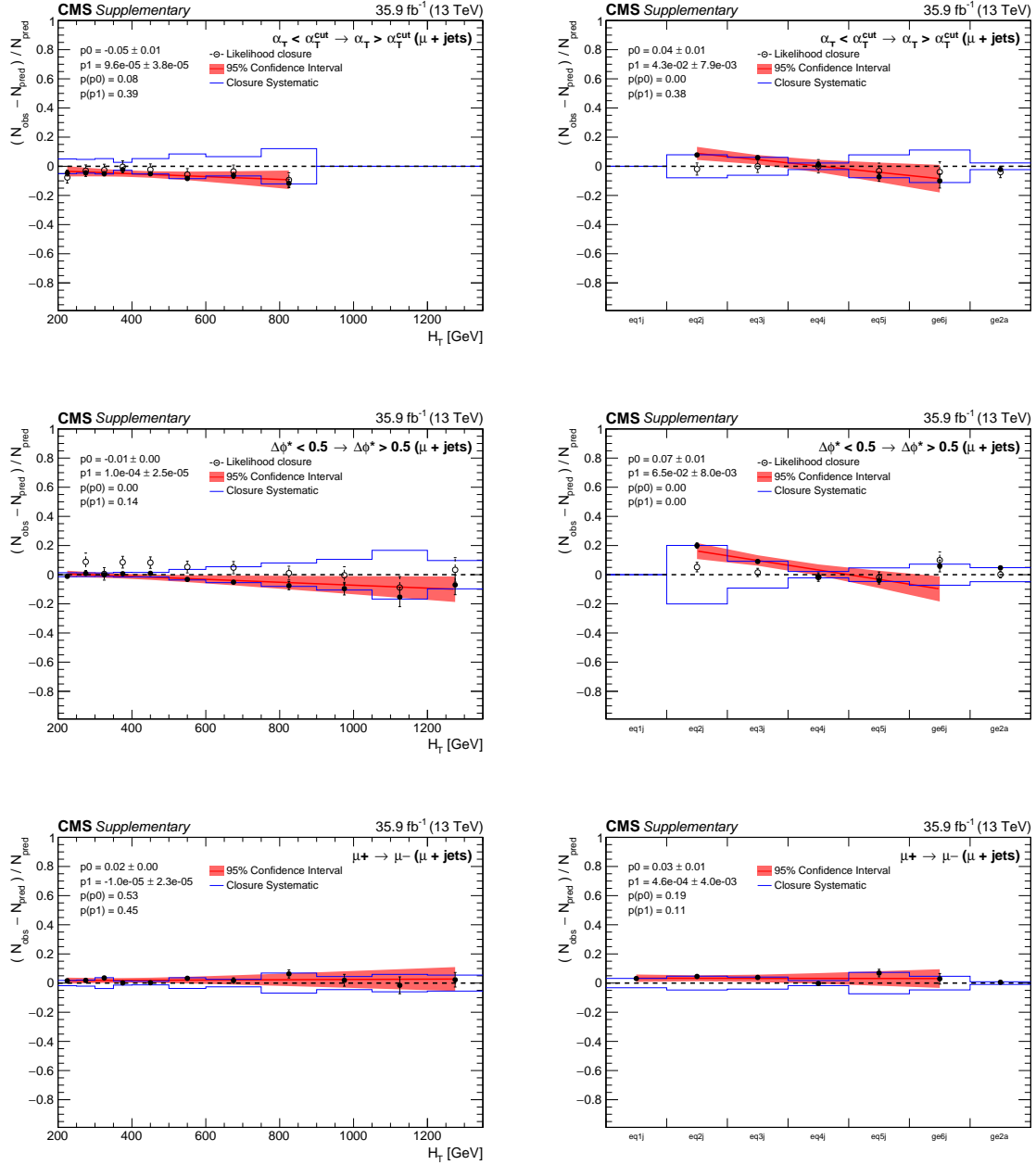


Figure 4.13.: Closure tests relating to extrapolations in α_T (top), $\Delta\phi_{\text{min}}^*$ (middle), and W boson polarisation (bottom), as a function of H_T (left) and n_{jet} (right). The level of closure obtained via a maximum likelihood method is indicated by the open circles. The blue lines represent the resulting systematic uncertainties that are assigned to the relevant transfer factors. A linear fit is also shown.

shown in Fig. 4.13. The level of closure and the resulting systematic uncertainties assigned to the $T(\mu \rightarrow W/t\bar{t})$ transfer factor are around $\sim 1\text{-}5\%$.

4.12.3. Uncertainties on the \cancel{H}_T distribution

The expected distribution of electroweak background events in the \cancel{H}_T variable is taken directly from the simulation, as described in Sec. 4.10.2. This was validated by checking that the ratio of the normalised distribution between data and simulation in the muon control regions is statistically compatible with unity. Specifically, the best-fit value of a linear parameter is checked to be consistent with zero across all $(n_{\text{jet}}, n_b, H_T)$ bins in each of the $\mu + \text{jets}$ and $\mu\mu + \text{jets}$ control regions.

A systematic uncertainty is assigned to the \cancel{H}_T distribution obtained from simulation, also referred to as the nominal \cancel{H}_T distribution or shape, to account for uncertainties in the simulation modelling. The value of the fitted linear parameter, together with its uncertainty added in quadrature, is used to vary the nominal \cancel{H}_T shape and derive two alternative distributions. These are then encoded in the statistical model of the search as $\pm 1\sigma$ systematic uncertainties, as will be described in Sec. 5.3. The uncertainties derived from the $\mu + \text{jets}$ control region are assigned to the \cancel{H}_T distribution of the $W/t\bar{t}$ background process, while those derived from the $\mu\mu + \text{jets}$ control region are assigned to the $Z(\rightarrow \nu\nu) + \text{jets}$ process.

The alternative \cancel{H}_T shapes typically result in an uncertainty on the number of background events in the final \cancel{H}_T bin within each $(n_{\text{jet}}, n_b, H_T)$ category that is in the range 5-20%.

In addition to the uncertainties derived from the linear fit to the data-to-simulation ratio, all of the sources of systematic uncertainty associated with the simulation correction factors described in Sec. 4.9 and applied to the transfer factors in Sec. 4.12.1 are also considered for the \cancel{H}_T modelling. This is done by varying each uncertainty in turn by $\pm 1\sigma$ and deriving further alternative \cancel{H}_T distributions (two for each source of uncertainty). In general, these uncertainties are sub-dominant compared to those derived from the linear fit.

Chapter 5.

Results and interpretation

In this chapter, the kinematic properties of the simplified models of long-lived gluino production with final states consisting of (displaced) jets and missing energy are presented. The statistical model used to perform the background estimation and analyse the observed 35.9 fb^{-1} of data is discussed. No significant discrepancy is found between the data and the standard model expectation. Upper limits are placed at a 95% confidence level on the cross sections of long-lived SUSY models.

5.1. Characterisation of long-lived gluino models

The expected binned event yields for six representative simplified models of Split SUSY are shown in Fig. 5.1, along with the expected standard model background (as determined using the method described in Sec. 5.4). An aggregated version of the nominal binning scheme (Sec. 4.6) is used for ease of presentation. The example models consist of a short ($c\tau = 1 \mu\text{m}$), medium ($c\tau = 1 \text{ mm}$) and long ($c\tau = 100 \text{ m}$) lifetime gluino, with both a compressed ($m_{\tilde{g}} - m_{\tilde{\chi}_1^0} = 100 \text{ GeV}$) and uncompressed mass spectrum.

For models with a compressed mass spectrum, the displaced jets originating from the decay of the gluino are produced with relatively low transverse momenta and tend to be below the 40 GeV threshold. The acceptance for these models relies on jets from initial state radiation. The events therefore populate the low n_{jet} and low H_T region of the parameter space of the search. This behaviour is independent of the lifetime of the gluino.

For models with an uncompressed mass spectrum, the displaced jets from the gluino decay are hard enough to be observed. Models with a promptly decaying gluino (given the detector's resolution, a decay length of $1\ \mu\text{m}$ is considered prompt-like) populate the higher n_{jet} and H_{T} categories. The jet reconstruction efficiency decreases as the decay length of the gluino increases. For decays occurring within the tracker ($10\ \text{m} \lesssim c\tau \lesssim 1\ \text{m}$) fewer hits are available for the reconstruction. Decays occurring within the calorimeters ($1\ \text{m} \lesssim c\tau \lesssim 10\ \text{m}$) result in jets containing no charged tracks, and may therefore result in the event being vetoed by the jet quality criteria described in Sec. 4.2. Jets produced within the muon chambers and outside the detector ($c\tau \gtrsim 10\ \text{m}$) cannot be reconstructed. With increasing lifetime, the behaviour of the uncompressed models therefore tends towards that of the compressed models. Finally, displaced jets in uncompressed models with $c\tau \sim 1\ \text{mm}$ exhibit similar characteristics as bottom quark jets, and are often tagged by the b-tagging algorithm. These events therefore populate the high n_{b} categories, with potentially up to four b-tagged jets.

5.2. Uncertainties on signal model simulation

The expected number of signal events is estimated using simulation. The various data-to-simulation correction factors discussed in Sec. 4.9 are applied. The uncertainties in each $(n_{\text{jet}}, n_{\text{b}}, H_{\text{T}}, \cancel{H}_{\text{T}})$ bin are derived by varying the corrections within their uncertainties and recomputing the simulated yields, analogously to the uncertainties on the background processes (Sec. 4.12.3). This includes uncertainties due to the corrections on the jet energy, pileup distribution, b-tagging efficiency, trigger efficiency, and ISR distribution. The integrated luminosity of $35.9\ \text{fb}^{-1}$ is measured with an uncertainty of 2.5% [22] which results in an additional uncertainty on the overall number of signal events. The statical uncertainties due the limited number of simulated events is also considered. Additional sources of uncertainty related to displaced jets are discussed in the remainder of this section. A summary of all sources of uncertainty and their typical sizes is shown in Tab. 5.1 for various representative simplified models of long-lived gluino production.

The requirement of $f_{\text{CH}} < 0.1$ on the most energetic jet of the event, discussed in Sec. 4.2, reduces the selection efficiency for models with $1\ \text{m} \lesssim c\tau \lesssim 10\ \text{m}$ to $\sim 30\%$. This is because of the lack of reconstructed charged particle tracks in the displaced

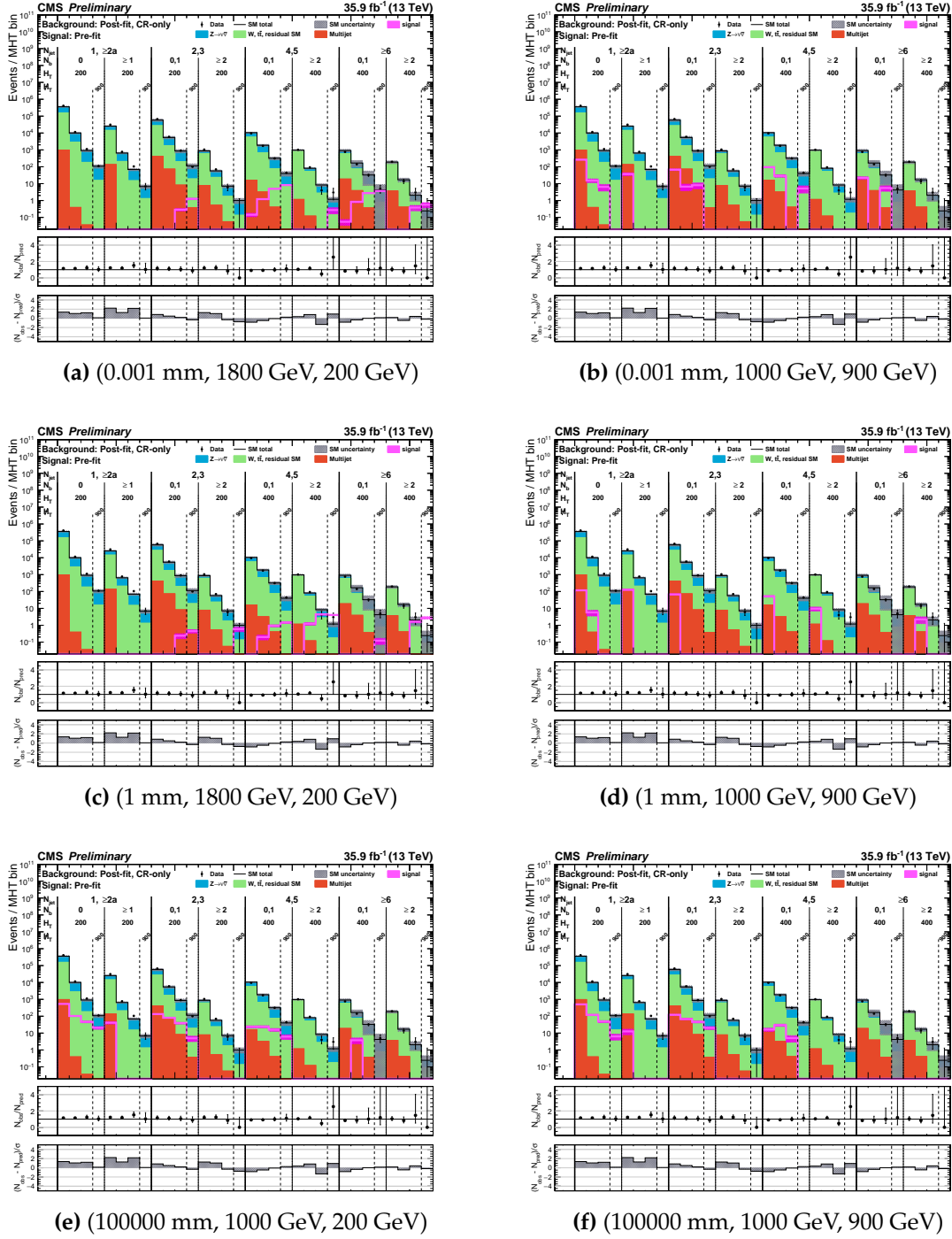


Figure 5.1.: Expected signal events for Split SUSY simplified models with a range of values of $(c\tau, m_{\tilde{g}}, m_{\tilde{\chi}_1^0})$, overlaid on the expected standard model background counts, using an aggregated binning scheme.

jets that are produced inside the calorimeters. For the same reason, the veto on events containing a jet that fails the identification requirements (which includes a

Source of uncertainty	$c\tau = 1 \mu\text{m}$		$c\tau = 1 \text{ mm}$		$c\tau = 10 \text{ m}$	
	(1800,200)	(1000,900)	(1800,200)	(1000,900)	(1000,200)	(1000,900)
Pileup	1-3	1-3	2-4	1-4	1-5	1-5
Jet energy scale	3-9	4-14	3-9	4-17	4-9	2-12
b-tagging	0-1	0-1	17-59	10-41	0-1	0-1
Trigger	3-4	0-2	2-4	0-2	0-4	0-1
ISR	3-5	2-10	2-5	2-9	2-14	3-14
Luminosity	2.6	2.6	2.6	2.6	2.6	2.6
Stat.	8-20	15-21	11-20	17-26	16-22	14-26

Table 5.1.: Summary of uncertainties (%) on the simplified long-lived gluino models for various values of $(m_{\tilde{g}}, m_{\tilde{\chi}_1^0})$ [GeV]. The quoted ranges correspond to the $\pm 1\sigma$ quantiles of the yield changes across all $(n_{\text{jet}}, n_b, H_T, \cancel{H}_T)$ bins.

minimum requirement on the charged component of jets), has a selection efficiency of $\sim 10\%$ for these models. Below and above this range in $c\tau$ the efficiencies of the jet identification and f_{CH} requirements are close to 100%. To account for a potential mismodelling of the simulation in the variables used for jet identification, the efficiency of these event selections are computed as a function of the decay lengths and pseudorapidities of the long-lived gluinos, and the sizes of the inefficiencies are propagated as a systematic uncertainty on the expected signal counts.

Jet identification requirements are also present in the trigger logic. The inefficiency of the trigger is measured to be at most 2% for events with gluinos decaying within the calorimeter region. This is applied as a correction to the simulation, as a function of decay length and pseudorapidity, and an appropriate systematic uncertainty is assigned.

As seen in the previous section, jets with a displacement of $\sim 1 \text{ mm}$ can be tagged by the b-tagging algorithm. This is because they have similar displacements as b-quarks. The b-tagging efficiency for displaced jets is measured as a function of the displacement d with respect to the primary vertex, in bins of p_T and η , and compared to the efficiency for standard model quarks. An example of this is shown in Fig. 5.2. Three regions are identified as $d < 0.1 \text{ mm}$ (small displacements), $d > 10 \text{ mm}$ (large displacements), and $0.1 < d < 10 \text{ mm}$ (“b-like” displacements). In the $0.1 < d < 10 \text{ mm}$ region, the b-tagging efficiency for displaced jets is approximately 60%, almost comparable to that for b-quarks ($\sim 80\%$). The nominal b-tagging correction factors and uncertainties (described in Sec. 4.9.3) are applied in the simulation to jets with this range of displacements, together with an additional

uncertainty of size 20-50% to cover differences in the efficiencies with respect to jets originating from b-quarks. For displacements of $d < 0.1$ mm and $d > 10$ mm, the efficiency falls to 1-5%, similar to that of light quarks. A conservative 100% uncertainty on the efficiency is taken in these regions.

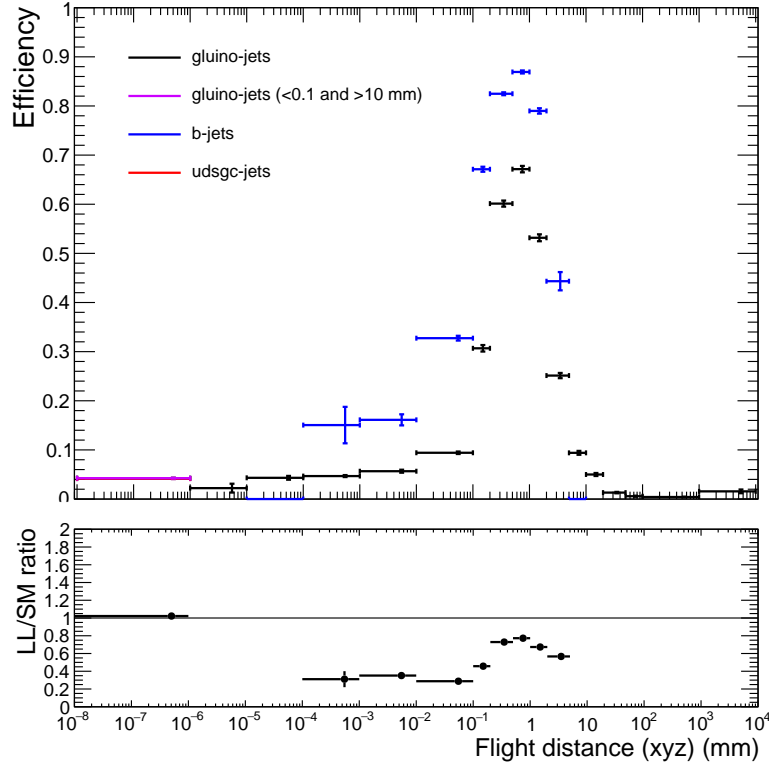


Figure 5.2.: Efficiency of the b-tagging algorithm for displaced jets originating from long-lived gluinos, compared to standard model bottom and light quarks, for jets with $100 < p_T < 140$ and $0 < |\eta| < 0.5$.

5.3. Statistical model

In order to perform a statistical analysis of the results obtained, a likelihood function is used to model the background and signal events across the $(n_{\text{jet}}, n_b, H_T, \cancel{H}_T)$ parameter space in the signal and control regions, accounting for all relevant uncertainties. The likelihood function is utilised to carry out the background estimation as well as to perform hypothesis tests to assess the sensitivity of the search to new physics.

The number of events in each bin of the $(n_{\text{jet}}, n_b, H_T, \cancel{H}_T)$ parameter space is modelled as a Poisson distribution, with an expected value given by that obtained from simulation, multiplied by *modifier* terms that account for the transfer factors and relevant uncertainties. The uncertainties are encoded as *nuisance parameters* with probability densities and correlations that will be discussed in this section.

The component of the likelihood function related to the $(n_{\text{jet}}, n_b, H_T)$ bin k in the signal region is given by:

$$\mathcal{L}_{\text{sig}}^k = \prod_j \mathcal{P} \left(n_{\text{sig}}^{k,j} \left| \sum_i (b_{Z,\text{sig}}^{i,j} r_Z^i \theta_{Z,\text{sig}}^{i,j} + b_{W,\text{sig}}^{i,j} r_W^i \theta_{W,\text{sig}}^{i,j} + b_{\text{QCD},\text{sig}}^{i,j} \theta_{\text{QCD},\text{sig}}^{i,j} + \mu_s s_{\text{sig}}^{i,j} \theta_{s,\text{sig}}^{i,j}) \right. \right), \quad (5.1)$$

where the product is over all \cancel{H}_T bins within the $(n_{\text{jet}}, n_b, H_T)$ bin, $n_{\text{sig}}^{k,j}$ is the number of events observed in data in a given $(n_{\text{jet}}, n_b, H_T, \cancel{H}_T)$ bin, the summation is over all fine $(n_{\text{jet}}, n_b, H_T)$ bins i that form part of the given coarse H_T bin (Sec. 4.6), $b_{Z,\text{sig}}^{i,j}$ and $b_{W,\text{sig}}^{i,j}$ are the number of $Z(\rightarrow \nu\nu) + \text{jets}$ and $W/\text{t}\bar{\text{t}}$ events expected based on simulation, r_Z^i and r_W^i are the control region based data-to-simulation correction ratios in the transfer factor equations (Eq. 4.25), $\theta_{Z,\text{sig}}^{i,j}$ and $\theta_{W,\text{sig}}^{i,j}$ encapsulate all relevant uncertainties related to the transfer factors (both from the data-driven closure tests and the variations in simulation), the \cancel{H}_T shape, and the limited number of simulated events, $b_{\text{QCD},\mu}^i$ is the number of QCD events estimated using the method described in Sec. 4.11 with $\theta_{\text{QCD},\text{sig}}^{i,j}$ encoding its uncertainty, $s_{\text{sig}}^{i,j}$ is the expected number of signal events based on simulation with $\theta_{s,\mu}^i$ encapsulating its uncertainties, and $\mu_s = \frac{\sigma}{\sigma_{\text{th}}}$ is a signal strength parameter that scales the signal model's cross section with respect to its theoretical value and is relevant when setting limits (Sec. 5.5).

The component of the likelihood function related to the $(n_{\text{jet}}, n_b, H_T)$ bin i in the $\mu + \text{jets}$ control region is given by:

$$\mathcal{L}_{\mu}^i = \mathcal{P} \left(n_{\mu}^i \left| b_{\mu}^i r_W^i \theta_{b,\mu}^i + b_{\text{QCD},\mu}^i + \mu_s s_{\mu}^i \theta_{s,\mu}^i \right. \right), \quad (5.2)$$

in which the small potential contributions from QCD and signal events are accounted for (based on the simulation). Similarly, the likelihood in the $\mu\mu + \text{jets}$

control region is written as:

$$\mathcal{L}_{\mu\mu}^i = \mathcal{P} \left(n_{\mu\mu}^i \left| b_{\mu\mu}^i r_Z^i \theta_{b,\mu\mu}^i + b_{\text{QCD},\mu\mu}^i + \mu_s s_{\mu\mu}^i \theta_{s,\mu\mu}^i \right. \right). \quad (5.3)$$

The correction parameters r_Z^i and r_W^i are shared between the signal region and relevant control region. These parameters are unconstrained (they are modelled by a uniform distribution) and therefore allow the background estimations to be made when maximising the likelihood function over the control regions.

Each source of uncertainty (described in Sec. 4.12) results in an uncertainty on the expected number of events of a given process in each bin of the search. The correlations of the uncertainties between bins are included in the likelihood function and, for simplicity, are chosen to be either 0 (uncorrelated) or 1 (perfectly correlated). As a simple example, a correlation of 1 between two bins, each with a (different) expected number of event counts and associated uncertainty, means that if the counts in one bin are increased by one standard deviation, the counts in the other bin also increase by one standard deviation. This is implemented in the likelihood model such that bins that are assumed to be fully correlated share the same nuisance parameter, whereas bins that are uncorrelated have independent nuisance parameters.

The nuisance parameters representing the systematic uncertainties derived from the data-driven closure tests (Sec. 4.12.2) are modelled as a log-normal distribution. As these are derived in turn as a function of n_{jet} and H_T , integrated over the other dimensions, and are statistical in nature, two sets of nuisance parameters are included that are considered to be correlated across the n_b , H_T and \cancel{H}_T (n_{jet} , n_b and \cancel{H}_T) dimensions and uncorrelated in n_{jet} (H_T).

The systematic uncertainties derived on the \cancel{H}_T shape (Sec. 4.12.3) are incorporated as $\pm 1\sigma$ alternative \cancel{H}_T distributions. The event yields in each bin of the distributions are interpolated quadratically between the alternative shapes and extrapolated linearly beyond this. This “morphing” procedure is controlled by a Gaussian nuisance parameter, and is described in Ref. [23]. Two sets of uncertainties are derived on the \cancel{H}_T distributions, by performing the linear fits described in Sec. 4.12.3 integrating over H_T and n_{jet} in turn. This results in two sets of uncertainties that are correlated in H_T and n_{jet} , respectively, and are derived for each of the $Z(\rightarrow \nu\nu) + \text{jets}$

(from the $\mu\mu + \text{jets}$ control region fit) and $W(\rightarrow \ell\nu) + \text{jets}$ (from the $\mu + \text{jets}$ control region fit) processes.

Similarly, the systematic uncertainties derived from variations of the data-to-simulation correction factors (Sec. 4.12.1) are also incorporated as alternative \mathcal{H}_T distributions in the signal region. In this case, these may also change the \mathcal{H}_T normalisation and therefore affect the transfer factors. In the control regions there is effectively no \mathcal{H}_T shape as they are not binned in this variable. Each of these uncertainties is assumed to originate from a unique underlying source, and so they are treated as being fully correlated across the full parameter space of the signal and control regions. In other words, there is only one nuisance parameter for each source of uncertainty that is shared among all bins and processes.

The statistical uncertainties due to the limited number of simulated events are modelled as a Gaussian distribution in each bin, and are uncorrelated across bins. Finally, the QCD estimate in the signal region is assigned a conservative 100% uncertainty, modelled as a log-normal distribution, that is uncorrelated across n_{jet} and H_T and correlated across n_b and \mathcal{H}_T .

The probability densities of the nuisance parameters are encoded within the likelihood function $\mathcal{L}_{\text{nuis}}$. The total likelihood for all bins in the signal and control regions and their uncertainties is then given by the product:

$$\mathcal{L} = \mathcal{L}_{\text{nuis}} \prod_k \mathcal{L}_{\text{sig}}^k \prod_i \mathcal{L}_\mu^i \prod_i \mathcal{L}_{\mu\mu}^i \quad (5.4)$$

5.4. Comparison of expected background and observed data

As will be discussed in Sec. 5.5, the sensitivity of the search is assessed by comparing the values of the maximised likelihood function under the background-only hypothesis ($\mu_s = 0$) and the background-plus-signal hypothesis ($\mu_s \neq 0$). First, it is instructive to compare the observed event counts in data with those expected from the standard model. The expected standard model background is obtained by performing the maximum likelihood fit under the background-only hypothesis to the control regions only (i. e. the signal region is excluded). This is essentially equivalent to the application of the transfer factor equations (Sec. 4.10).

The results of this fit are shown in Figs. 5.3 and 5.4. These show the observed number of events in data and the expected number of $Z, W/t\bar{t}$ and QCD background events in every $(n_{\text{jet}}, n_b, H_T, \cancel{H}_T)$ bin of the signal region. The uncertainties on the background expectation include both the systematic and statistical components added in quadrature. Also shown are the ratios in each bin between the observed and expected number of events, and the z-scores (the difference between observed and expected counts, divided by the uncertainty on the expected counts). The ratios and z-scores, integrated over \cancel{H}_T , are also summarised in Fig. 5.5. The observed and expected event counts are also summarised in tabulated form in App. B.1.

Overall, no statistically significant excess is observed in the data. The z-scores are found to be centred on zero, with almost all bins having values within $\pm 2\sigma$. Similarly, the ratios of observed and expected counts are consistent with unity.

A likelihood fit is also performed under the background-only hypothesis to the full control and signal region parameter space. The results of this are shown in App B.2. Again, the binned observed number of events is found to be consistent, within uncertainties, with those expected from the standard model. The best fit values of the nuisance parameters are shown in App. B.3 and can be seen to be within their $\pm 1\sigma$ values.

5.5. Procedure for setting limits on signal models

Given the good agreement between the observed data and the standard model expectation, with no significant excess above the number of expected events in any bin, no evidence of new physics beyond the standard model is found. Statistical hypothesis tests are carried out in order to assess the incompatibility of the data with various models of long-lived supersymmetry. Upper bounds are placed on their cross sections at a 95% confidence level.

In the hypothesis tests, the parameter being tested is the signal strength, while all other parameters are considered to be nuisance parameters, labelled collectively as θ . For a test of a model with a signal strength of μ_s , one can use a profile likelihood ratio as a test statistic:

$$t(\mu_s) = 2 \ln \frac{\mathcal{L}(\hat{\mu}_s, \hat{\theta})}{\mathcal{L}(\mu_s, \hat{\theta}(\mu_s))} \quad (5.5)$$

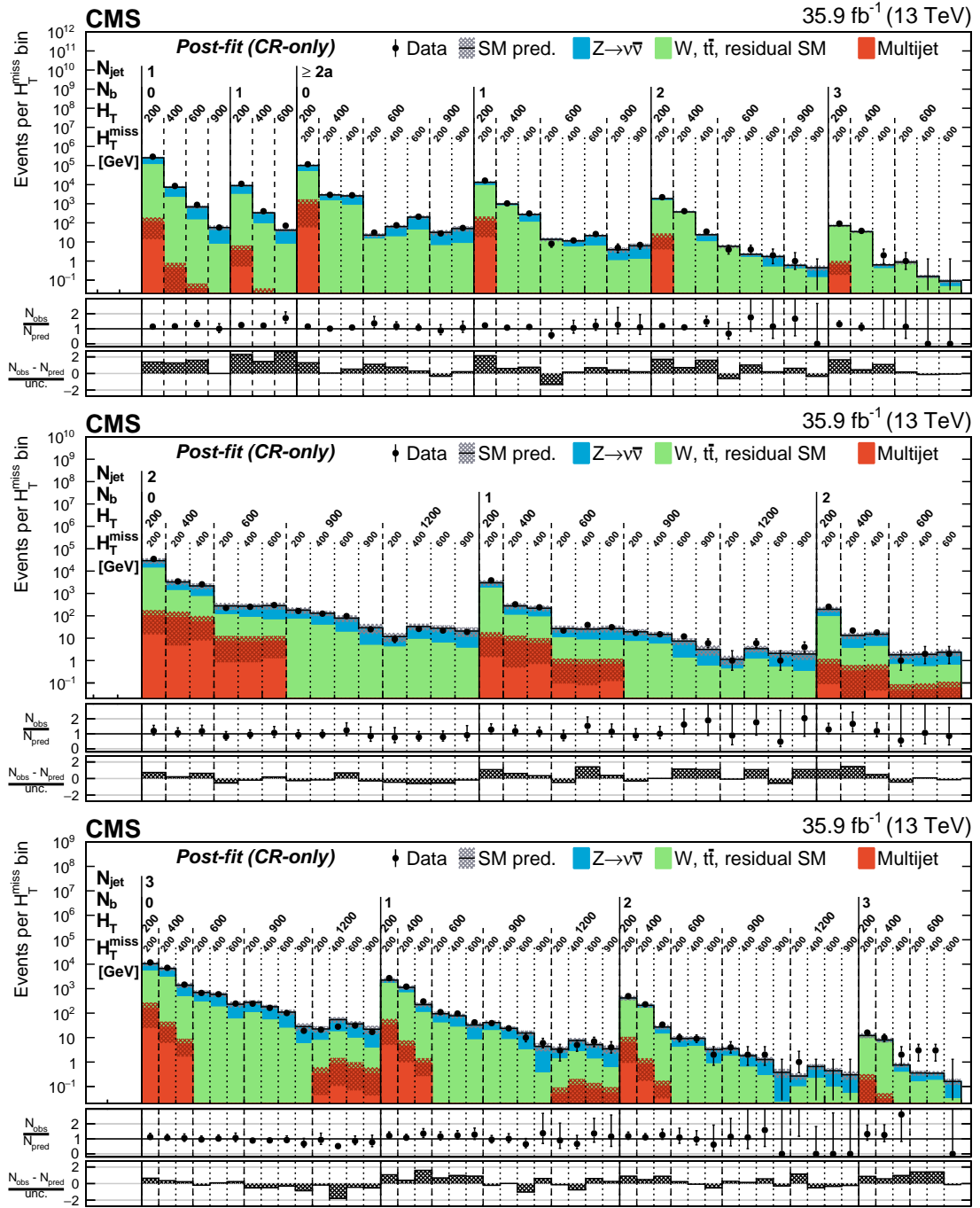
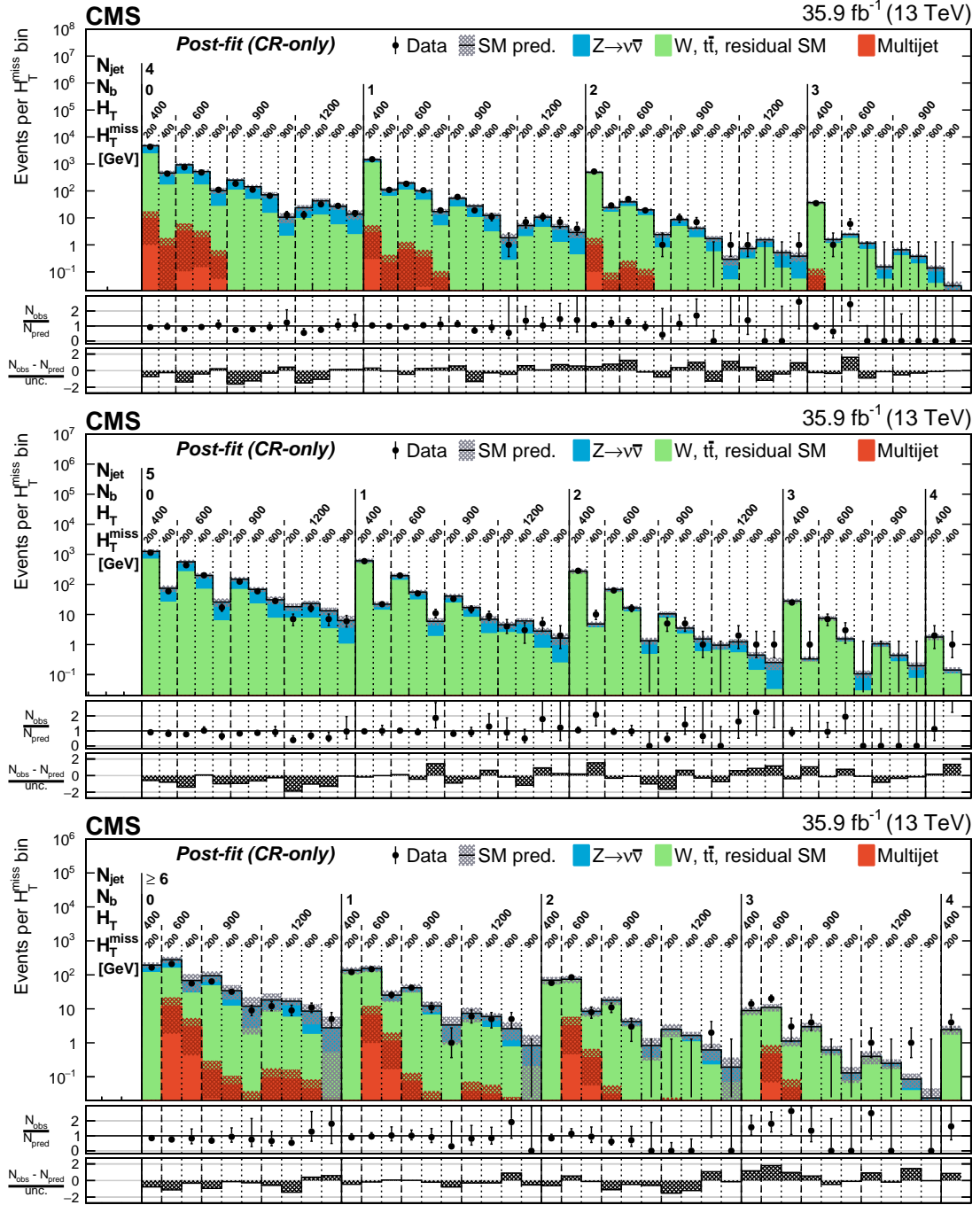


Figure 5.3.: Number of events observed (solid markers) and expected number of Z, W/ $t\bar{t}$ and QCD background events (histograms, with shaded bands representing the statistical and systematic uncertainties) in every n_b , H_T and H_T^{miss} bin of the jet categories $n_{\text{jet}} = 1, \geq 2a$ (top), $n_{\text{jet}} = 2$ (middle), and $n_{\text{jet}} = 3$ (bottom), as determined from the maximum likelihood fit to the control regions. The centre panel of each sub-figure shows the ratios of the observed and expected counts, while the lower panel shows the corresponding z-score, as defined in the text.



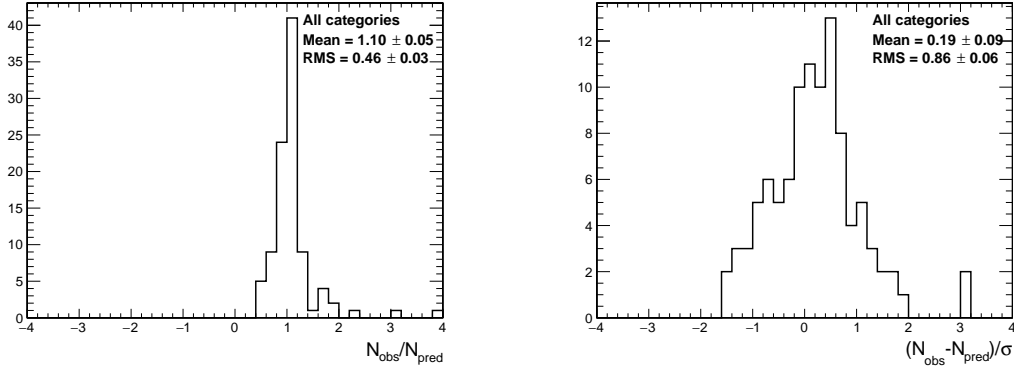


Figure 5.5.: Histograms of the ratios of the observed and expected event counts (left) and corresponding z-scores (right), as defined in the text, for all (n_{jet}, n_b, H_T) bins, as determined from the background-only maximum likelihood fit to the control regions.

where $\hat{\mu}_s$ and $\hat{\theta}$ are the global maximum likelihood values of the signal strength and nuisance parameters, and $\hat{\theta}(\mu_s)$ is the maximum likelihood value of the nuisance parameters for a fixed signal strength of μ_s . A value of $t(\mu_s) = 0$ represents a perfect agreement between the hypothesised signal strength μ_s and the observed data, while larger values of $t(\mu_s)$ represent an increasing incompatibility between μ_s and the data.

The best fit value of the signal strength is constrained to lie within $0 \leq \hat{\mu}_s \leq \mu_s$. The lower constraint is imposed so as to avoid a non-physical cross section. The upper bound is chosen so that an upward fluctuation in the signal counts such that $\hat{\mu}_s > \mu_s$ is not treated as evidence against that model. The final test statistic is then given by [24]:

$$t(\mu_s) = \begin{cases} 2 \ln \frac{\mathcal{L}(0, \hat{\theta}(0))}{\mathcal{L}(\mu_s, \hat{\theta}(\mu_s))} & \hat{\mu}_s < 0 \\ 2 \ln \frac{\mathcal{L}(\hat{\mu}_s, \hat{\theta})}{\mathcal{L}(\mu_s, \hat{\theta}(\mu_s))} & 0 \leq \hat{\mu}_s \leq \mu_s \\ 0 & \hat{\mu}_s > \mu_s \end{cases} \quad (5.6)$$

The incompatibility of a signal model with data can be assessed with the p-value:

$$\text{CL}_{b+s}(\mu_s) = \int_{t(\mu_s)_{\text{obs}}}^{\infty} f(t(\mu_s) | \mu_s) dt(\mu_s) \quad (5.7)$$

where $f(t(\mu_s)|\mu_s)$ is the probability density of the test statistic under the hypothesised signal strength μ_s , and $t(\mu_s)_{\text{obs}}$ is the value of the test statistic observed in data. In order to reject a signal model, not only is a small p-value CL_{b+s} required, but also a good compatibility with the background-only model, as determined by the probability:

$$\text{CL}_b(\mu_s) = \int_{t(\mu_s)_{\text{obs}}}^{\infty} f(t(\mu_s)|0) dt(\mu_s) \quad (5.8)$$

where $f(t(\mu_s)|0)$ is the probability density of the test statistic under the background-only model ($\mu_s = 0$). The ratio of the two probabilities is then constructed as [25,26]:

$$\text{CL}_s(\mu_s) = \frac{\text{CL}_{b+s}(\mu_s)}{\text{CL}_b(\mu_s)} \quad (5.9)$$

A particular signal strength is considered to be excluded at a 95% confidence level if the corresponding CL_s value is less than 0.05. For a given signal model, the upper limit on the signal strength $\mu_s^{95\%}$ is given by the largest value of μ_s that is excluded with $\text{CL}_s < 0.05$.

The distributions $f(t(\mu_s)|\mu_s)$ and $f(t(\mu_s)|0)$ are approximated by analytical probability functions that are derived in the limit of a large sample of events [27]. While the above procedure provides the *observed* limit on the signal strength, an *expected* limit can also be computed as the median value of $\mu_s^{95\%}$ obtained under the background-only model. The uncertainty on the expected limit is given by the appropriate quantiles of the distribution of $\mu_s^{95\%}$.

5.6. Limits on long-lived supersymmetry

Simplified models of Split SUSY are simulated with a range of gluino and LSP masses for various gluino lifetimes from 1 μm to 100 m, in addition to a promptly decaying and metastable gluino. An upper limit on the signal strength (and cross section) of each model is computed. These limits are presented in the $(m_{\tilde{g}}, m_{\tilde{\chi}_1^0})$ plane for each simulated value of $c\tau$ in Figs. 5.6 - 5.8. The excluded regions correspond to mass points with limits on their signal strength of $\mu_s^{95\%} < 1$. Both the expected and observed excluded regions are shown, with experimental uncertain-

ties and uncertainties on the theoretical cross sections indicated. The excluded mass regions for each value of $c\tau$ are summarised in Fig. 5.9.

For the model with a promptly decaying gluino, gluino and LSP masses of up to ~ 1650 GeV and ~ 900 GeV, respectively, are excluded. The excluded regions for models with gluino lifetimes of $c\tau = 1, 10, 100 \mu\text{m}$ are comparable to the prompt decay scenario. A moderate improvement in sensitivity is found for models with $c\tau = 1, 10$ mm, with maximum excluded gluino and LSP masses of 1750 GeV and 1000 GeV, respectively. This is because these signal events occupy the high n_b categories, and the amount of background is considerably smaller than in the bins with no b-tagged jets. The sensitivity is reduced for models with lifetimes larger than $c\tau > 100$ mm as the acceptance to jets from the gluino decay becomes smaller. The limiting case is that of a metastable gluino. In this case, the gluinos always decay outside of the detector and so the acceptance for these models relies entirely on ISR jets. Gluino masses up to 900 GeV are excluded, and the sensitivity is independent of the LSP mass.

The observed exclusion regions are found to be $\sim 1\text{-}2\sigma$ weaker than the expected ones for most of the models considered. This difference is due to slight upward fluctuations in the observed events across several categories in the signal region.

As mentioned in Sec. 4.8.2, the results for the Split SUSY models have been obtained assuming no interactions of the R-hadrons with the detector material. Nevertheless, the effect of matter interactions has been checked. A non-negligible fraction of R-hadrons that traverse the muon chambers are identified as muons. Similarly, charged R-hadrons that decay near the calorimeters may be reconstructed as single isolated tracks. This leads to a reduction in acceptance for models with $c\tau \gtrsim 1$ m as a consequence of the veto on events containing muons or isolated tracks. The excluded mass regions weaken by 50-200 GeV for these signal models. The change is negligible for models with $c\tau \lesssim 1$ m.

Despite being optimised for prompt decay signatures and not employing dedicated techniques for identifying long-lived particles, the search can be seen to have a good sensitivity across a wide range of lifetimes and masses. This is mainly due to the inclusive nature of the search, with low thresholds on kinematic variables such as H_T and n_{jet} , and an acceptance to jets from ISR. In particular, this search provides coverage that is complementary to dedicated searches at the LHC for models with $c\tau \lesssim 1$ cm or a metastable gluino, as well as models with a very compressed mass

spectrum. This is because dedicated techniques require a minimum decay length and a decay that occurs within the detector and within the time frame of an LHC run, as well as a sufficiently large mass difference such that the decay products can be reconstructed.

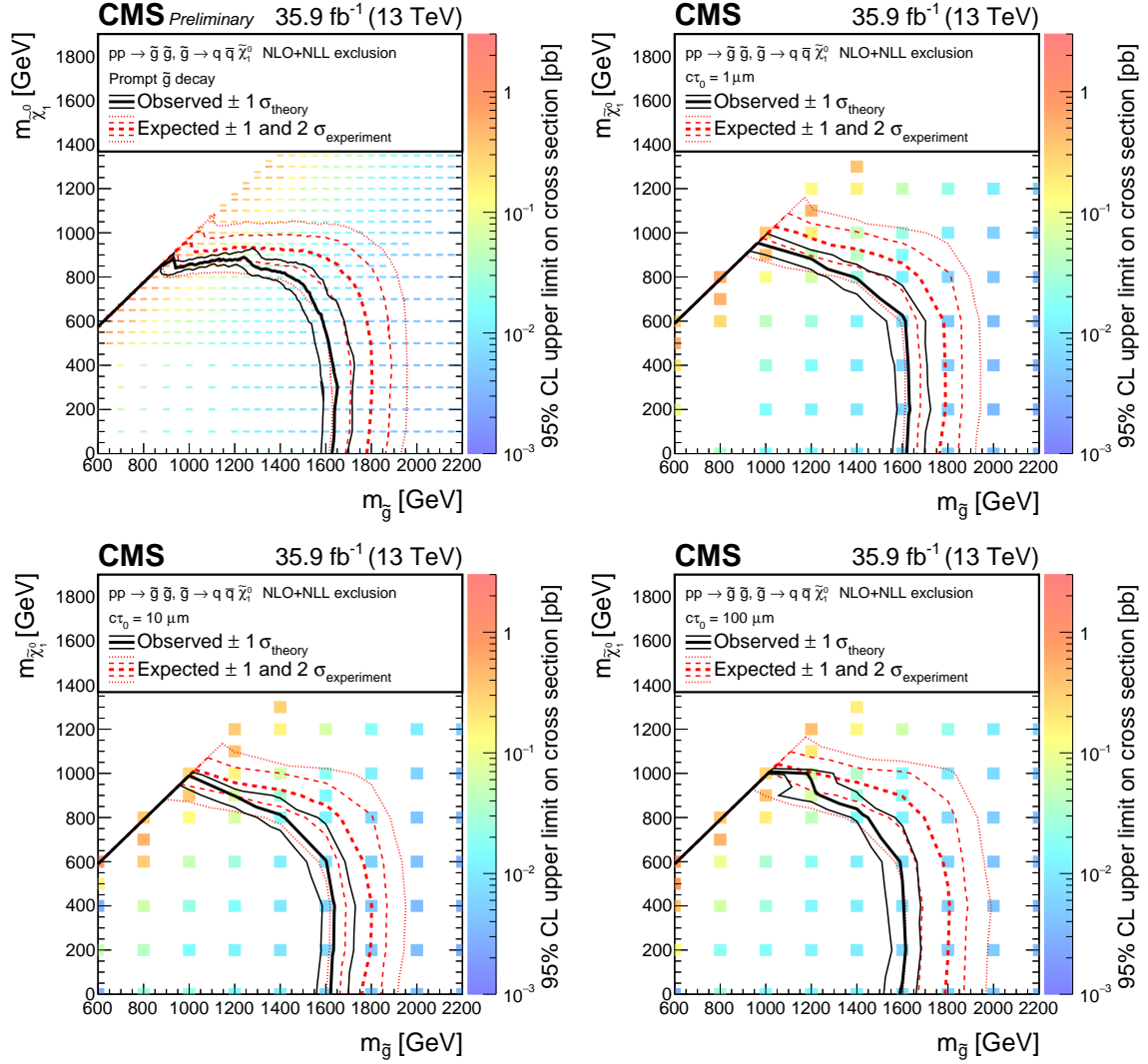


Figure 5.6.: Observed upper limit in cross section at 95% confidence level (indicated by the colour scale) as a function of the \tilde{g} and $\tilde{\chi}_1^0$ masses for the Split SUSY simplified models. Each subfigure represents a different gluino lifetime. The thick (thin) black line indicates the observed excluded region assuming the nominal ($\pm 1\sigma$ in theoretical cross section uncertainty) production cross section. The red dashed (dashed and dotted) represents the median ($\pm 1\sigma$ and $\pm 2\sigma$ in experimental uncertainty) expected excluded region.

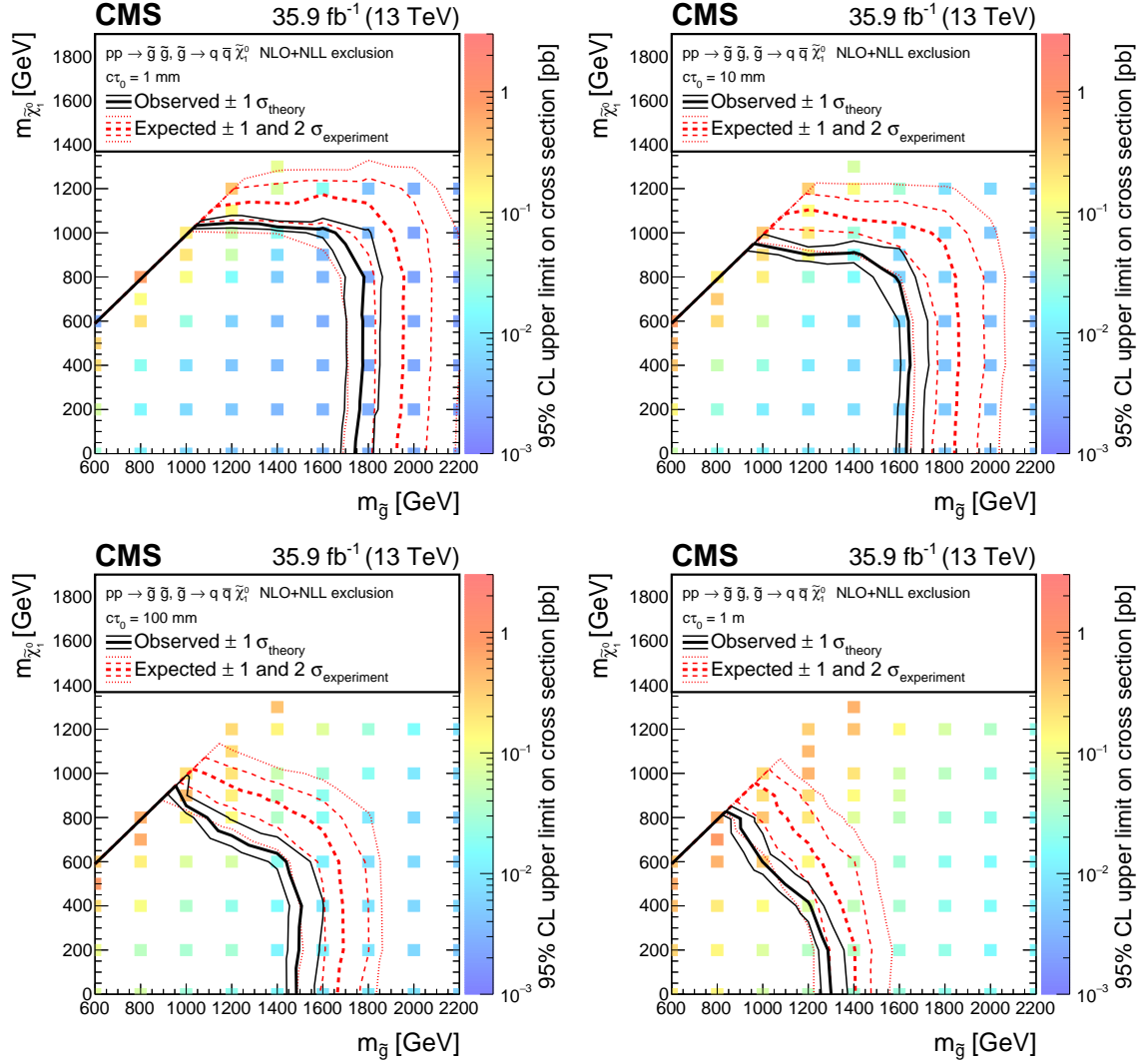


Figure 5.7.: Observed upper limit in cross section at 95% confidence level (indicated by the colour scale) as a function of the \tilde{g} and $\tilde{\chi}_1^0$ masses for the Split SUSY simplified models. Each subfigure represents a different gluino lifetime. The thick (thin) black line indicates the observed excluded region assuming the nominal ($\pm 1\sigma$ in theoretical cross section uncertainty) production cross section. The red dashed (dashed and dotted) represents the median ($\pm 1\sigma$ and $\pm 2\sigma$ in experimental uncertainty) expected excluded region.

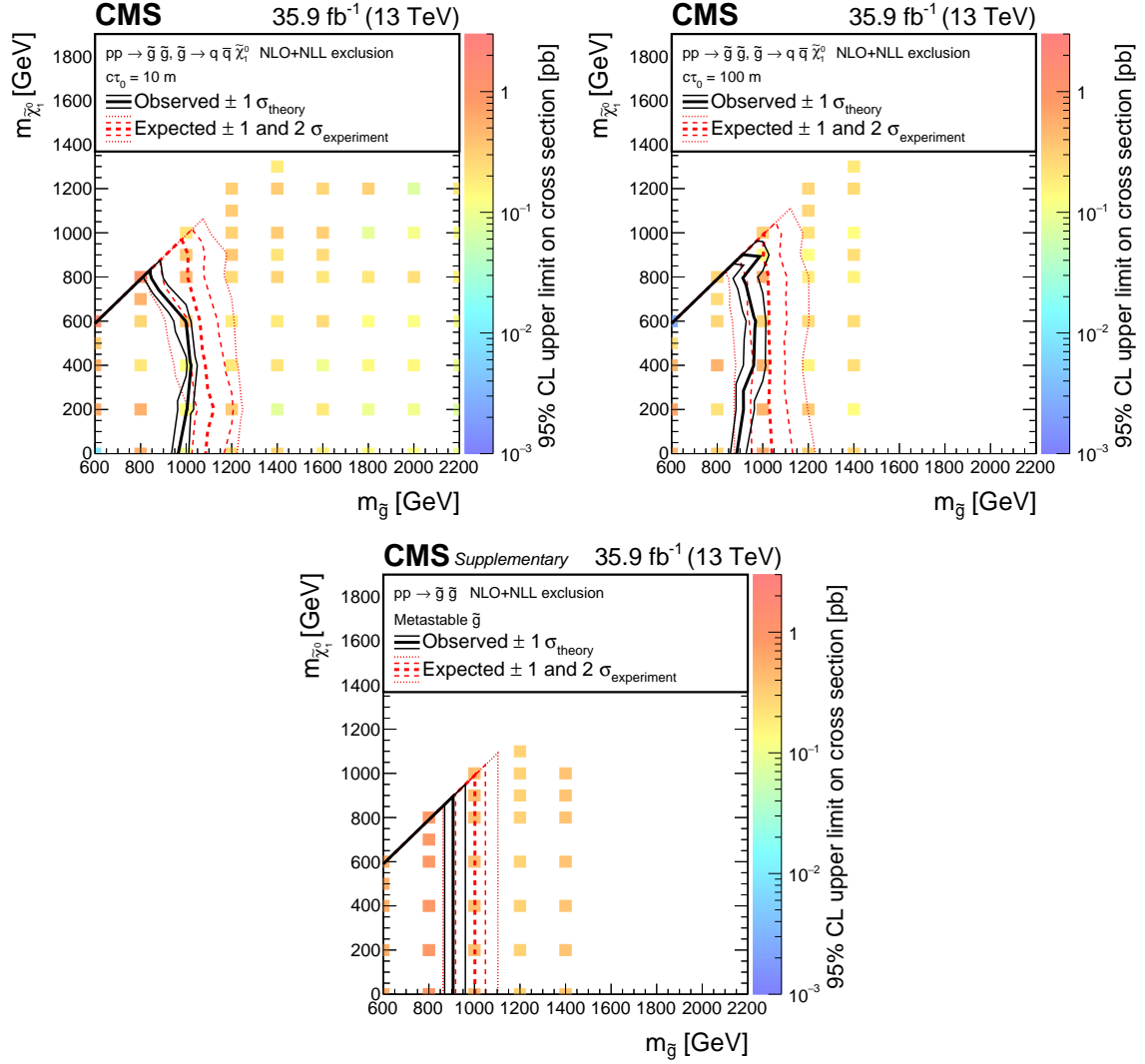


Figure 5.8.: Observed upper limit in cross section at 95% confidence level (indicated by the colour scale) as a function of the \tilde{g} and $\tilde{\chi}_1^0$ masses for the Split SUSY simplified models. Each subfigure represents a different gluino lifetime. The thick (thin) black line indicates the observed excluded region assuming the nominal ($\pm 1\sigma$ in theoretical cross section uncertainty) production cross section. The red dashed (dashed and dotted) represents the median ($\pm 1\sigma$ and $\pm 2\sigma$ in experimental uncertainty) expected excluded region.

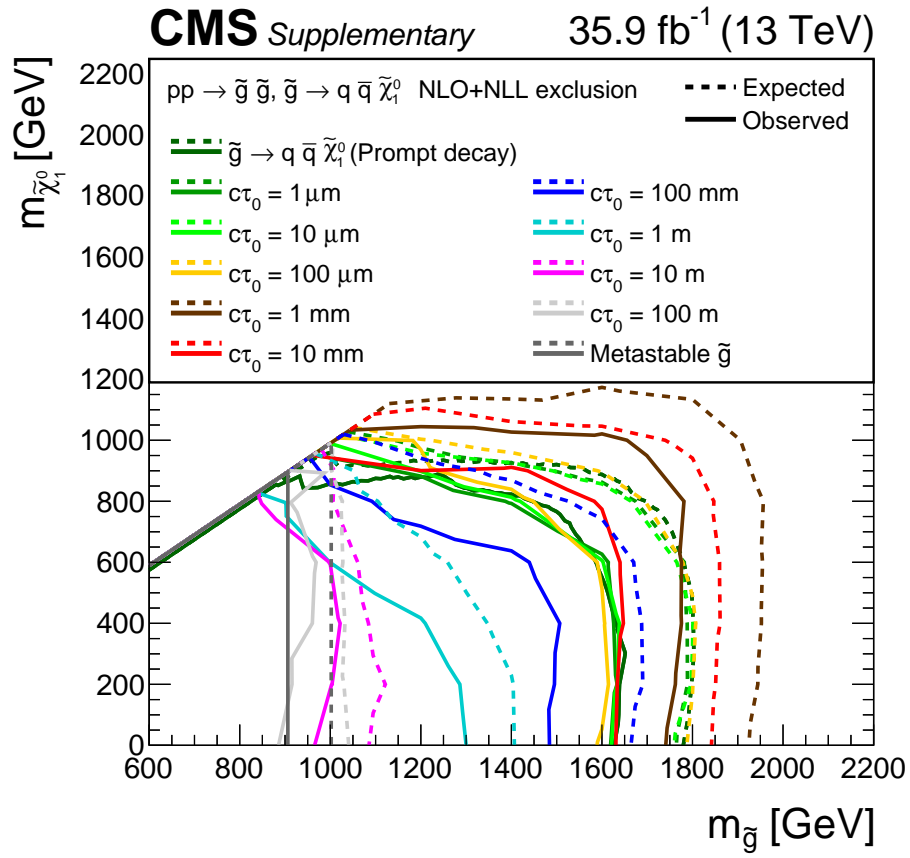


Figure 5.9.: Summary of observed and expected excluded regions at 95% confidence level as a function of the \tilde{g} and $\tilde{\chi}_1^0$ masses for various gluino lifetimes for the Split SUSY simplified models.

Chapter 6.

Conclusion

This is the conclusion.

Prompt search retains some sensitivity for long (short) gluino (DM) lifetimes (and is the most sensitive sub-cm and lifetimes beyond the detector, hence continue with prompt search in future), although clearly could be improved with a dedicated search/tagger as shown by the b-tag effects.

Appendix A.

Appendix: Search strategy

A.1. Uncertainties on transfer factors derived from variations in simulation

This appendix shows the changes of the transfer factors, which are used to assign systematic uncertainties to them, upon varying the various correction factors applied to the simulation (Sec. 4.9) by one standard deviation up and down according to their measured uncertainties. This is discussed in Sec. 4.12.1.

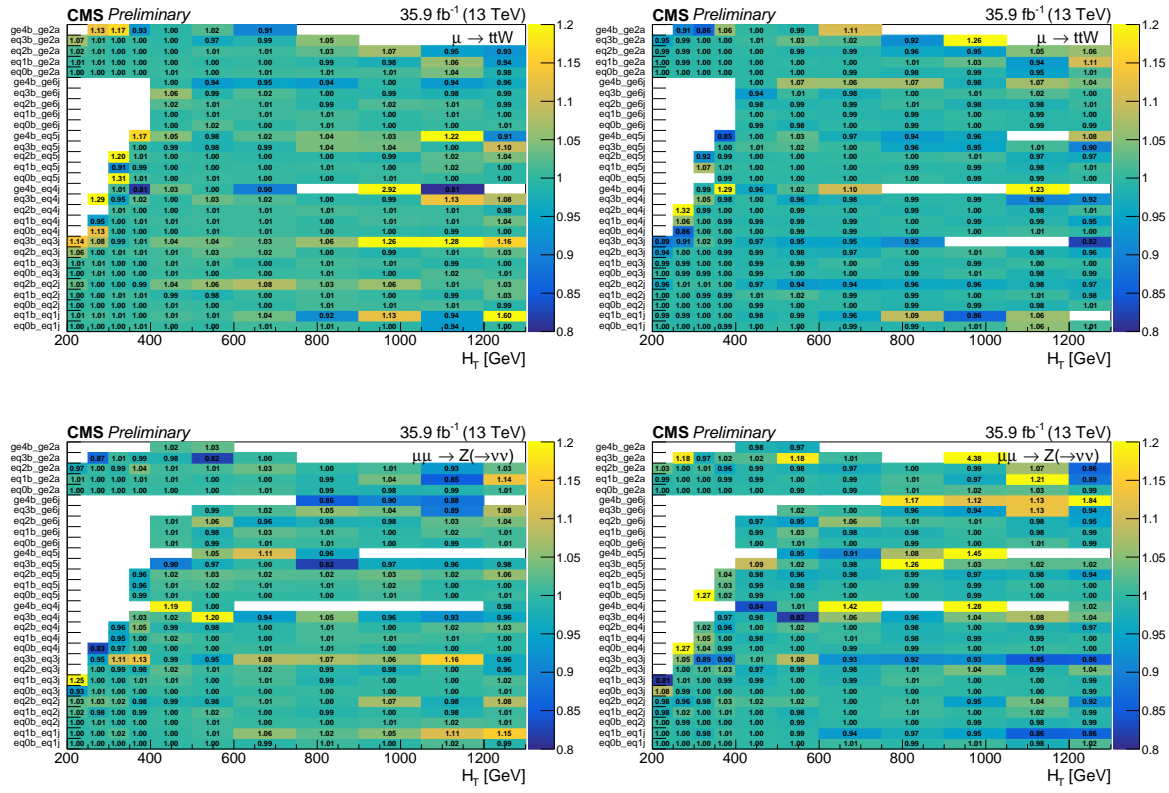


Figure A.1: The ratio of the $T(\mu \rightarrow W/t\bar{t})$ (top) and $T(\mu\mu \rightarrow Z)$ (bottom) transfer factors in each $(n_{\text{jet}}, n_b, H_T)$ bin when varying the pileup correction factors by $+1\sigma$ (left) and -1σ (right) with respect to their nominal values.

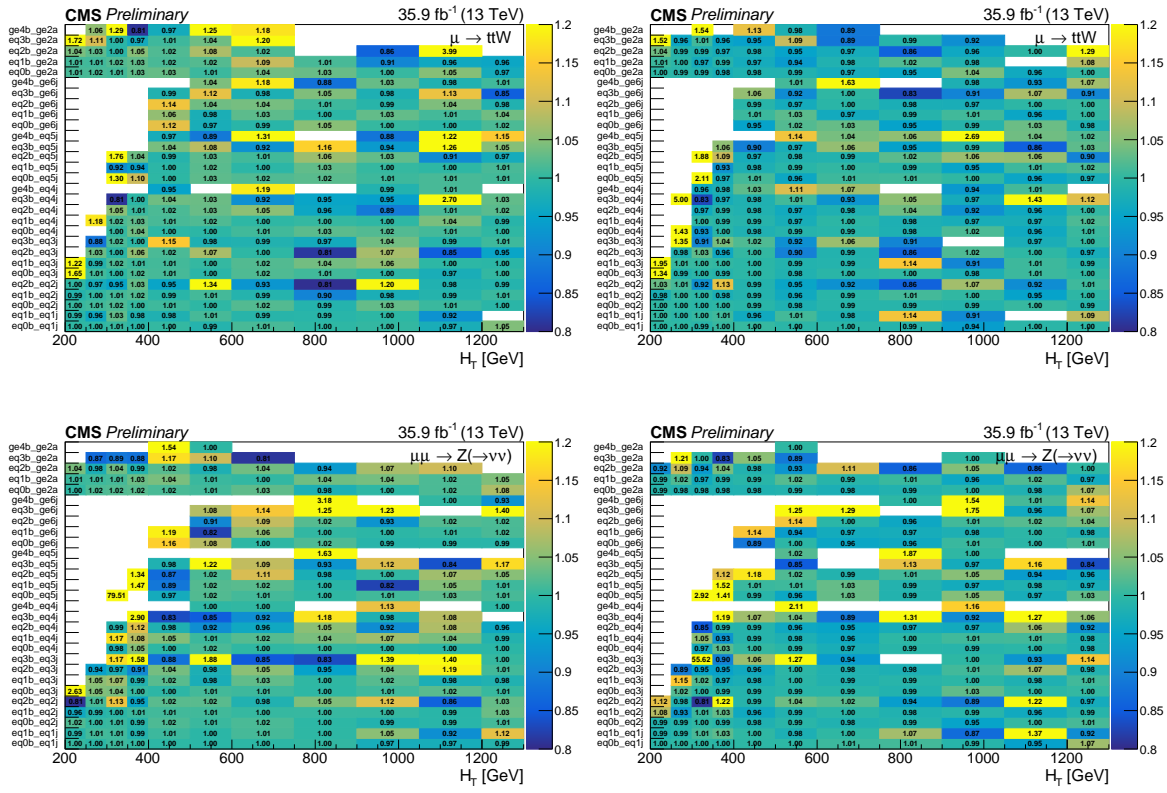


Figure A.2.: The ratio of the $T(\mu \rightarrow W/\bar{t}\bar{t})$ (top) and $T(\mu\mu \rightarrow Z)$ (bottom) transfer factors in each $(n_{\text{jet}}, n_b, H_T)$ bin when varying the jet energy correction factors by $+1\sigma$ (left) and -1σ (right) with respect to their nominal values.

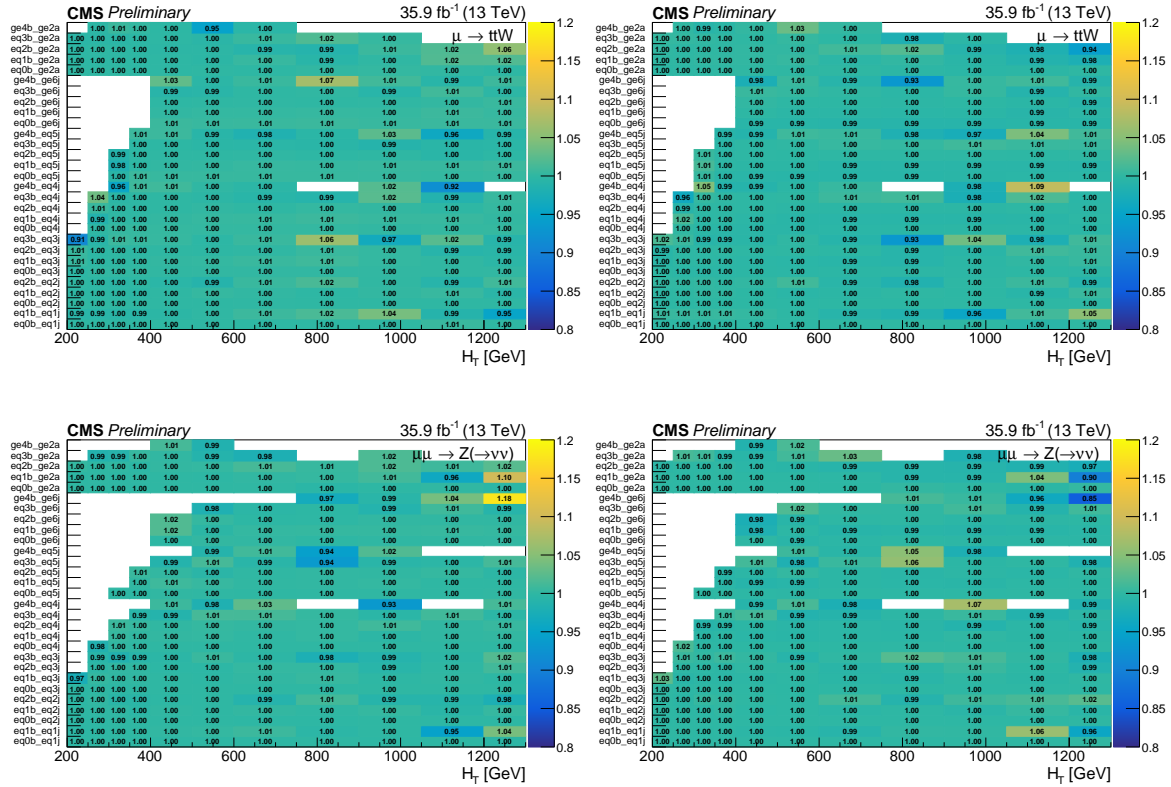


Figure A3.: The ratio of the $T(\mu \rightarrow W/\text{t}\bar{\text{t}})$ (top) and $T(\mu\mu \rightarrow Z)$ (bottom) transfer factors in each $(n_{\text{jet}}, n_b, H_T)$ bin when varying the b-tagging correction factors for bottom and charm quarks by $+1\sigma$ (left) and -1σ (right) with respect to their nominal values.

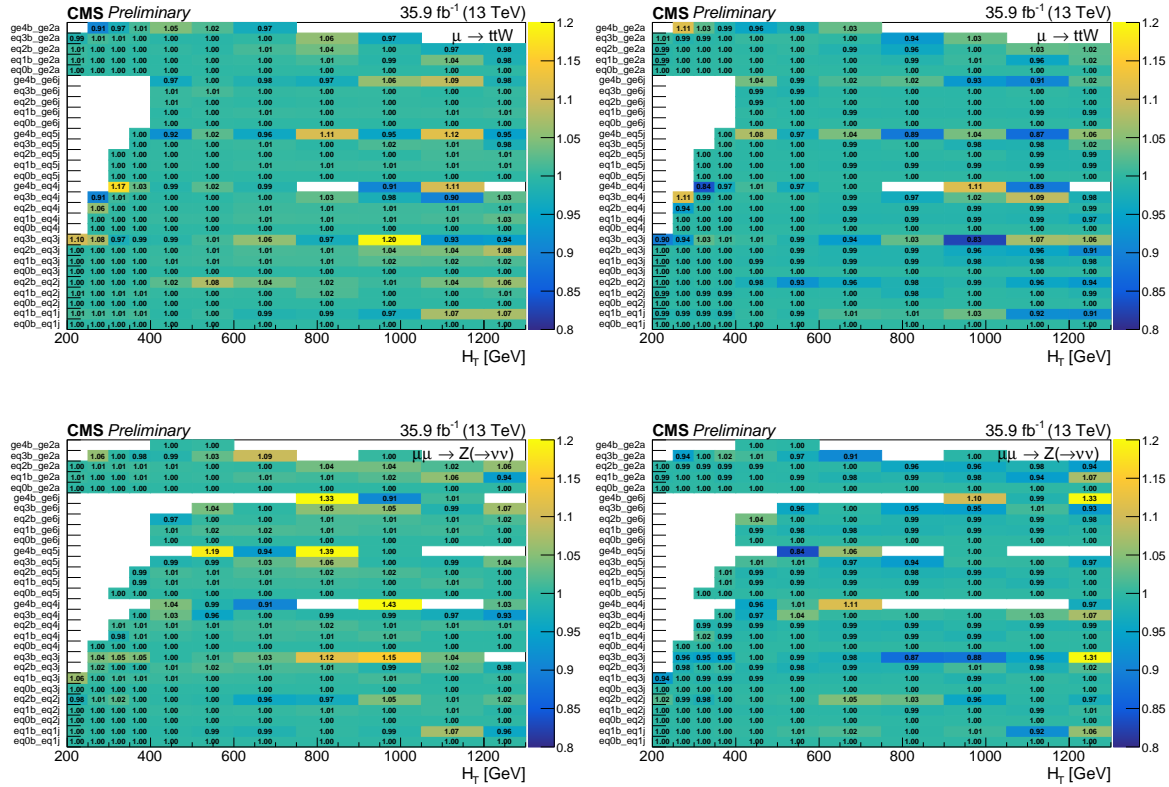


Figure A.4. The ratio of the $T(\mu \rightarrow W/\text{t}\bar{\text{t}})$ (top) and $T(\mu\mu \rightarrow Z)$ (bottom) transfer factors in each $(n_{\text{jet}}, n_b, H_T)$ bin when varying the b-tagging correction factors for light partons (u, d, s, gluon) by $+1\sigma$ (left) and -1σ (right) with respect to their nominal values.

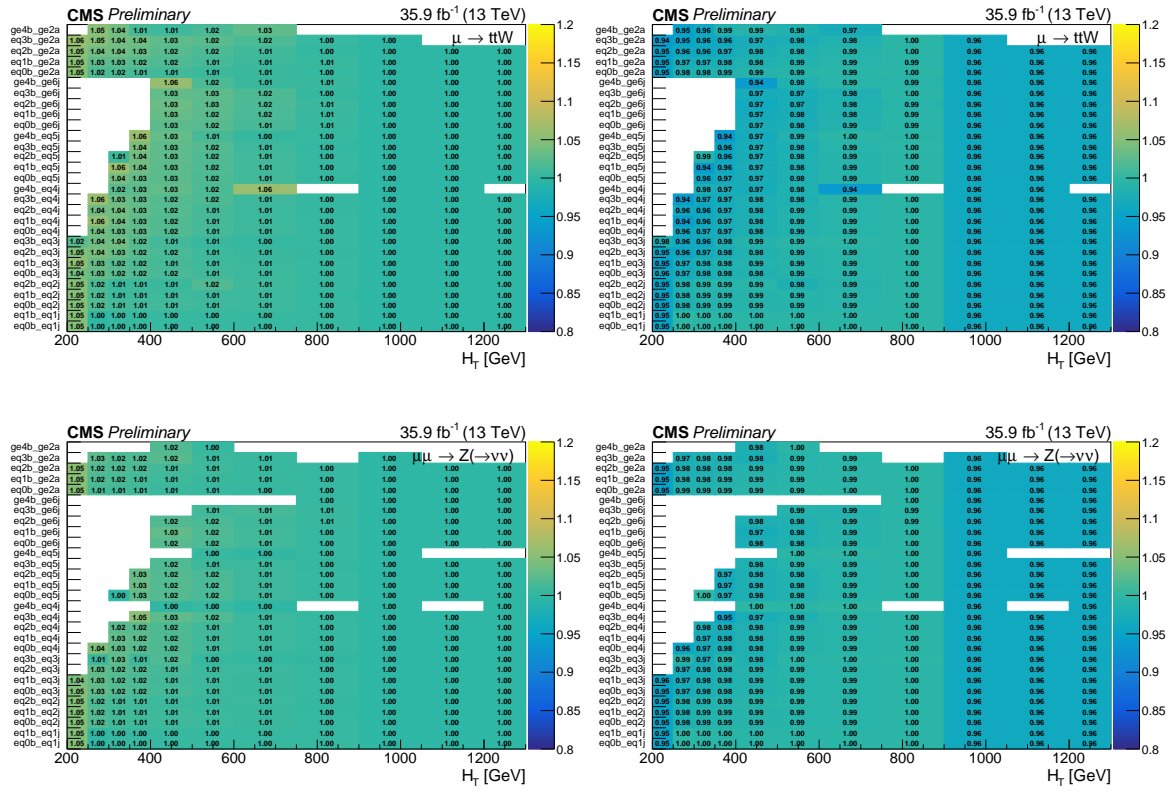


Figure A.5.: The ratio of the $T(\mu \rightarrow W/t\bar{t})$ (top) and $T(\mu\mu \rightarrow Z)$ (bottom) transfer factors in each $(n_{\text{jet}}, n_b, H_T)$ bin when varying the trigger correction factors by $+1\sigma$ (left) and -1σ (right) with respect to their nominal values.

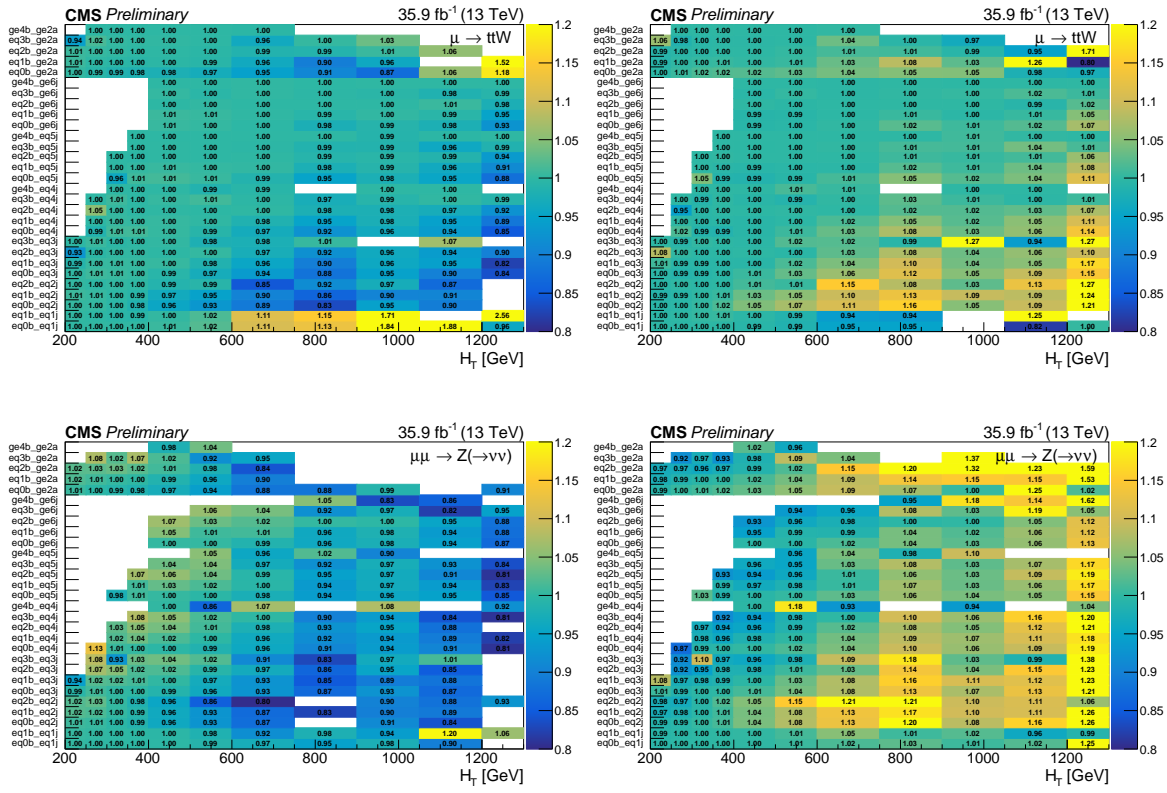


Figure A.6.: The ratio of the $T(\mu \rightarrow W/t\bar{t})$ (top) and $T(\mu\mu \rightarrow Z)$ (bottom) transfer factors in each $(n_{\text{jet}}, n_b, H_T)$ bin when varying the boson p_T dependent NLO correction factors by $+1\sigma$ (left) and -1σ (right) with respect to their nominal values.

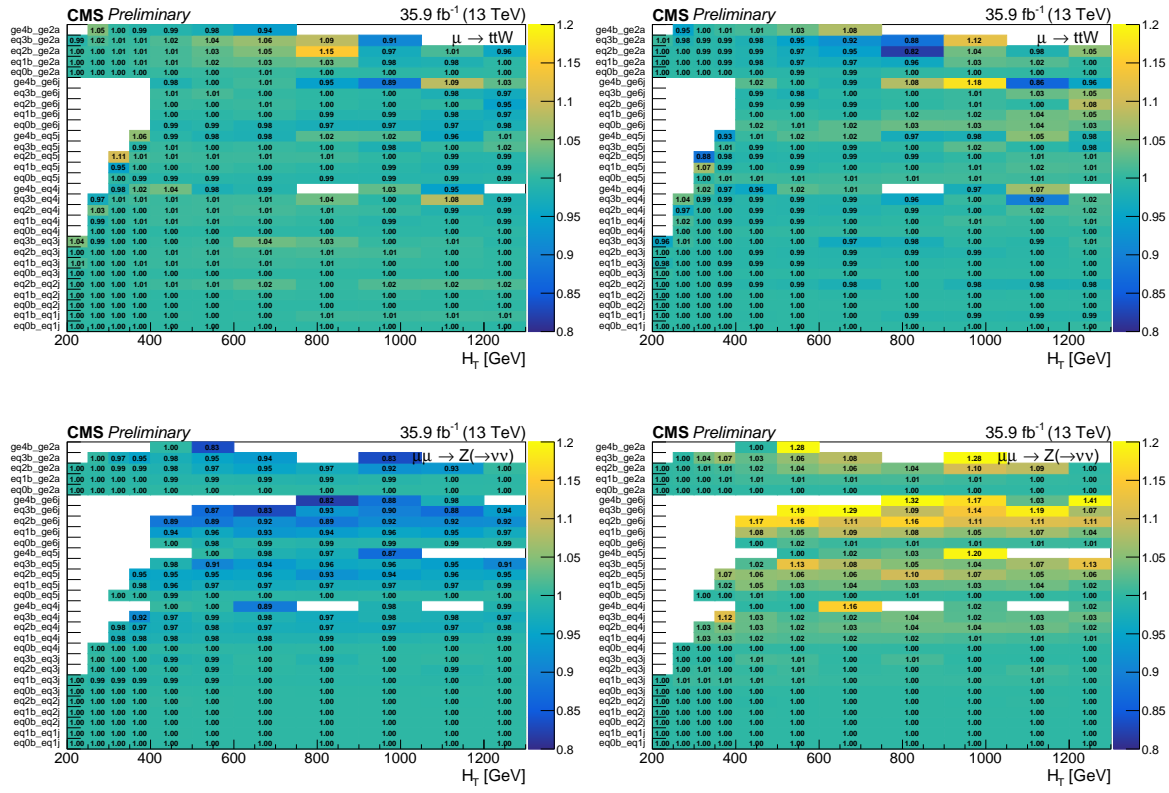


Figure A.7.: The ratio of the $T(\mu \rightarrow W/t\bar{t})$ (top) and $T(\mu\mu \rightarrow Z)$ (bottom) transfer factors in each $(n_{\text{jet}}, n_b, H_T)$ bin when varying the $t\bar{t}$ ISR correction factors by $+1\sigma$ (left) and -1σ (right) with respect to their nominal values.

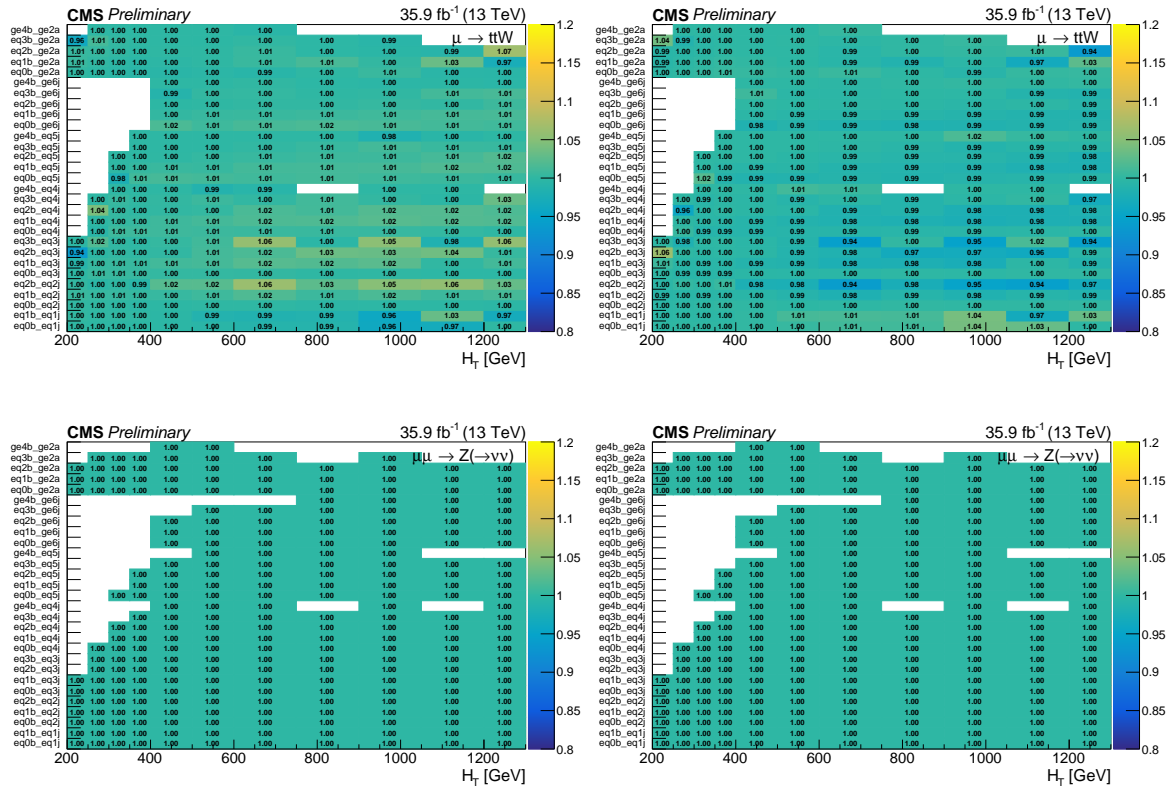


Figure A.8.: The ratio of the $T(\mu \rightarrow W/t\bar{t})$ (top) and $T(\mu\mu \rightarrow Z)$ (bottom) transfer factors in each $(n_{\text{jet}}, n_b, H_T)$ bin when varying the W cross section correction factors by $+1\sigma$ (left) and -1σ (right) with respect to their nominal values.

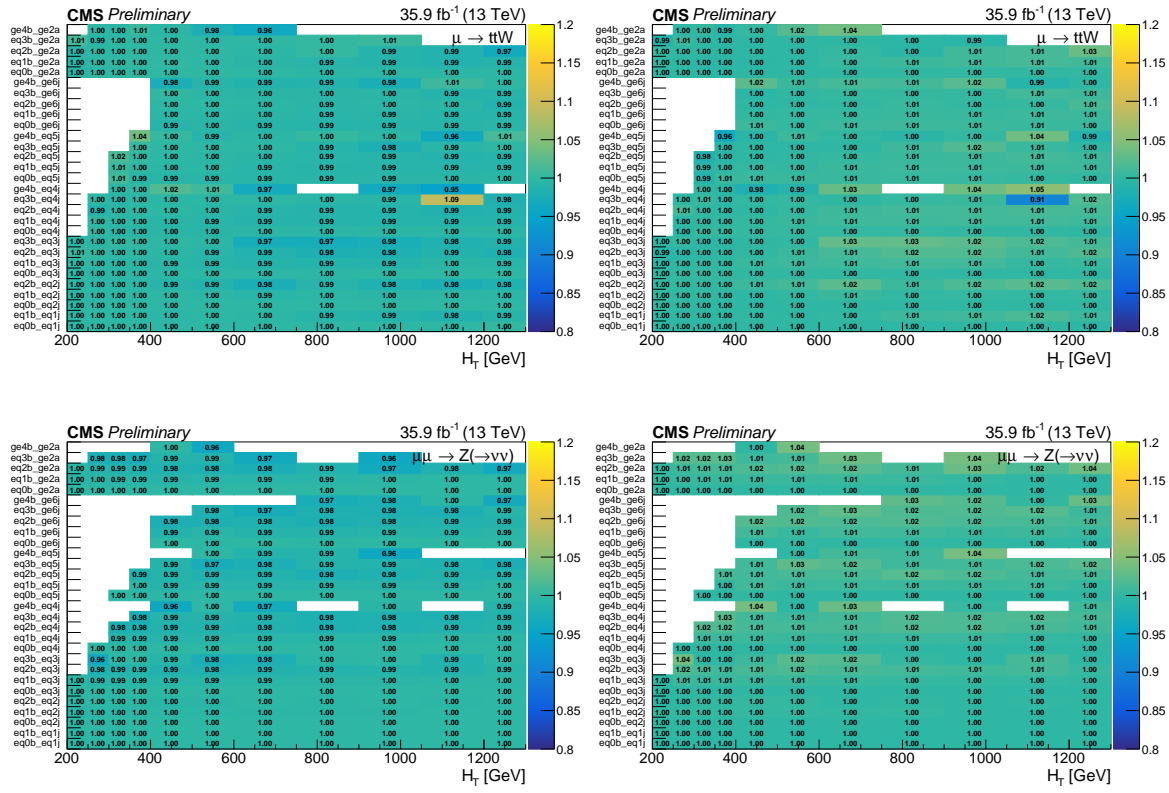


Figure A.9.: The ratio of the $T(\mu \rightarrow W/t\bar{t})$ (top) and $T(\mu\mu \rightarrow Z)$ (bottom) transfer factors in each $(n_{\text{jet}}, n_b, H_T)$ bin when varying the $t\bar{t}$ cross section correction factors by $+1\sigma$ (left) and -1σ (right) with respect to their nominal values.

Appendix B.

Appendix: Results and interpretation

B.1. Comparison of expected background and observed data

This appendix shows the results of the maximum likelihood fit to the control regions under the background-only hypothesis, as discussed in Sec. 5.4, in tabulated form.

Table B.1.: Observed data counts and background expectations from the background-only likelihood fit to the control regions, for the $n_{\text{jet}} = 1$ category. The uncertainties in the background expectations include statistical as well as systematic contributions.

n_{jet}	n_{b}	H_{T} [GeV]	Data	SM		
1	0	200 – 400	291353	254856.1	\pm	30252.2
1	0	400 – 600	8572	7342.2	\pm	610.4
1	0	600 – 900	878	680.1	\pm	206.4
1	0	900 – ∞	57	56.9	\pm	31.6
1	1	200 – 400	11072	8864.3	\pm	1044.9
1	1	400 – 600	406	334.6	\pm	32.4
1	1	600 – ∞	71	41.5	\pm	13.1

Table B.2.: Observed data counts and background expectations from the background-only likelihood fit to the control regions, for the $n_{\text{jet}} \geq 2a$ category. The uncertainties in the background expectations include statistical as well as systematic contributions.

n_{jet}	n_b	H_T [GeV]	\cancel{H}_T [GeV]	Data	SM		
$\geq 2a$	0	200 – 400	200 – ∞	116868	101411.4	\pm	14127.9
$\geq 2a$	0	400 – 600	200 – 400	2932	2909.4	\pm	396.2
$\geq 2a$	0	400 – 600	400 – ∞	2800	2582.2	\pm	345.7
$\geq 2a$	0	600 – 900	200 – 400	31	22.7	\pm	5.2
$\geq 2a$	0	600 – 900	400 – 600	75	63.8	\pm	12.3
$\geq 2a$	0	600 – 900	600 – ∞	211	198.9	\pm	62.8
$\geq 2a$	0	900 – ∞	200 – 900	28	31.8	\pm	12.5
$\geq 2a$	0	900 – ∞	900 – ∞	54	50.3	\pm	32.0
$\geq 2a$	1	200 – 400	200 – ∞	16307	13333.6	\pm	1563.7
$\geq 2a$	1	400 – 600	200 – 400	1042	969.1	\pm	129.2
$\geq 2a$	1	400 – 600	400 – ∞	310	275.8	\pm	36.0
$\geq 2a$	1	600 – 900	200 – 400	8	13.7	\pm	2.7
$\geq 2a$	1	600 – 900	400 – 600	12	11.4	\pm	1.8
$\geq 2a$	1	600 – 900	600 – ∞	26	21.5	\pm	6.4
$\geq 2a$	1	900 – ∞	200 – 900	5	3.9	\pm	1.5
$\geq 2a$	1	900 – ∞	900 – ∞	7	6.3	\pm	4.0
$\geq 2a$	2	200 – 400	200 – ∞	2200	1856.5	\pm	229.0
$\geq 2a$	2	400 – 600	200 – 400	410	373.9	\pm	52.5
$\geq 2a$	2	400 – 600	400 – ∞	35	23.9	\pm	3.4
$\geq 2a$	2	600 – 900	200 – 400	4	5.9	\pm	1.2
$\geq 2a$	2	600 – 900	400 – 600	4	2.3	\pm	0.4
$\geq 2a$	2	600 – 900	600 – ∞	2	1.7	\pm	0.5
$\geq 2a$	2	900 – ∞	200 – 900	1	0.6	\pm	0.1
$\geq 2a$	2	900 – ∞	900 – ∞	0	0.4	\pm	0.3
$\geq 2a$	3	200 – 400	200 – ∞	92	70.7	\pm	10.0
$\geq 2a$	3	400 – 600	200 – 400	38	34.4	\pm	5.4
$\geq 2a$	3	400 – 600	400 – ∞	2	0.6	\pm	0.1
$\geq 2a$	3	600 – ∞	200 – 400	1	0.9	\pm	0.2
$\geq 2a$	3	600 – ∞	400 – 600	0	0.2	\pm	0.0
$\geq 2a$	3	600 – ∞	600 – ∞	0	0.1	\pm	0.0

Table B.3.: Observed data counts and background expectations from the background-only likelihood fit to the control regions, for the $n_{\text{jet}} = 2$ category. The uncertainties in the background expectations include statistical as well as systematic contributions.

n_{jet}	n_b	H_T [GeV]	\mathcal{H}_T [GeV]	Data	SM		
2	0	200 – 400	200 – ∞	34934	29224.5	\pm	6798.6
2	0	400 – 600	200 – 400	3468	3274.3	\pm	759.7
2	0	400 – 600	400 – ∞	2568	2176.9	\pm	560.2
2	0	600 – 900	200 – 400	226	276.7	\pm	74.0
2	0	600 – 900	400 – 600	253	268.4	\pm	65.1
2	0	600 – 900	600 – ∞	303	284.6	\pm	110.9
2	0	900 – 1200	200 – 400	165	179.3	\pm	54.6
2	0	900 – 1200	400 – 600	125	130.9	\pm	34.6
2	0	900 – 1200	600 – 900	97	78.7	\pm	35.5
2	0	900 – 1200	900 – ∞	25	29.3	\pm	19.3
2	0	1200 – ∞	200 – 400	9	11.8	\pm	5.1
2	0	1200 – ∞	400 – 600	26	33.4	\pm	9.7
2	0	1200 – ∞	600 – 900	22	28.0	\pm	12.9
2	0	1200 – ∞	900 – ∞	19	20.9	\pm	16.7
2	1	200 – 400	200 – ∞	3850	3006.6	\pm	674.9
2	1	400 – 600	200 – 400	327	277.4	\pm	65.3
2	1	400 – 600	400 – ∞	240	219.3	\pm	55.1
2	1	600 – 900	200 – 400	22	26.9	\pm	7.1
2	1	600 – 900	400 – 600	39	25.5	\pm	6.3
2	1	600 – 900	600 – ∞	31	27.1	\pm	10.1
2	1	900 – 1200	200 – 400	17	19.3	\pm	5.8
2	1	900 – 1200	400 – 600	15	14.9	\pm	4.0
2	1	900 – 1200	600 – 900	12	7.4	\pm	3.3
2	1	900 – 1200	900 – ∞	6	3.2	\pm	2.1
2	1	1200 – ∞	200 – 400	1	1.1	\pm	0.5
2	1	1200 – ∞	400 – 600	6	3.4	\pm	1.0
2	1	1200 – ∞	600 – 900	1	2.1	\pm	0.9
2	1	1200 – ∞	900 – ∞	4	2.0	\pm	1.6
2	2	200 – 400	200 – ∞	254	196.1	\pm	44.4
2	2	400 – 600	200 – 400	22	13.2	\pm	3.2
2	2	400 – 600	400 – ∞	18	15.2	\pm	3.8
2	2	600 – ∞	200 – 400	1	1.8	\pm	0.5
2	2	600 – ∞	400 – 600	2	1.9	\pm	0.5
2	2	600 – ∞	600 – ∞	2	2.3	\pm	0.9

Table B.4.: Observed data counts and background expectations from the background-only likelihood fit to the control regions, for the $n_{\text{jet}} = 3$ category. The uncertainties in the background expectations include statistical as well as systematic contributions.

n_{jet}	n_b	H_T [GeV]	\mathcal{H}_T [GeV]	Data	SM		
3	0	200 – 400	200 – ∞	11815	10504.3	\pm	1860.3
3	0	400 – 600	200 – 400	7120	6666.9	\pm	1143.0
3	0	400 – 600	400 – ∞	1463	1391.0	\pm	288.2
3	0	600 – 900	200 – 400	668	698.5	\pm	132.2
3	0	600 – 900	400 – 600	593	582.0	\pm	123.5
3	0	600 – 900	600 – ∞	246	231.4	\pm	91.2
3	0	900 – 1200	200 – 400	245	275.3	\pm	47.6
3	0	900 – 1200	400 – 600	164	182.3	\pm	31.1
3	0	900 – 1200	600 – 900	101	109.8	\pm	42.1
3	0	900 – 1200	900 – ∞	19	28.2	\pm	16.4
3	0	1200 – ∞	200 – 400	21	22.5	\pm	6.5
3	0	1200 – ∞	400 – 600	28	54.2	\pm	11.0
3	0	1200 – ∞	600 – 900	31	36.1	\pm	13.3
3	0	1200 – ∞	900 – ∞	17	22.0	\pm	15.6
3	1	200 – 400	200 – ∞	2703	2242.6	\pm	400.0
3	1	400 – 600	200 – 400	1212	1125.8	\pm	197.2
3	1	400 – 600	400 – ∞	301	222.4	\pm	42.5
3	1	600 – 900	200 – 400	110	94.6	\pm	18.3
3	1	600 – 900	400 – 600	96	77.9	\pm	16.2
3	1	600 – 900	600 – ∞	42	32.7	\pm	12.4
3	1	900 – 1200	200 – 400	39	41.2	\pm	7.5
3	1	900 – 1200	400 – 600	24	23.9	\pm	4.1
3	1	900 – 1200	600 – 900	10	15.4	\pm	5.8
3	1	900 – 1200	900 – ∞	6	4.4	\pm	2.2
3	1	1200 – ∞	200 – 400	3	3.4	\pm	0.9
3	1	1200 – ∞	400 – 600	5	7.5	\pm	1.6
3	1	1200 – ∞	600 – 900	7	5.1	\pm	1.9
3	1	1200 – ∞	900 – ∞	4	3.5	\pm	2.4
3	2	200 – 400	200 – ∞	495	418.2	\pm	79.0
3	2	400 – 600	200 – 400	229	208.3	\pm	38.9
3	2	400 – 600	400 – ∞	34	27.0	\pm	5.2
3	2	600 – 900	200 – 400	10	9.1	\pm	1.8
3	2	600 – 900	400 – 600	9	9.3	\pm	1.9
3	2	600 – 900	600 – ∞	2	3.2	\pm	1.2
3	2	900 – 1200	200 – 400	4	3.5	\pm	0.7
3	2	900 – 1200	400 – 600	2	1.8	\pm	0.3
3	2	900 – 1200	600 – 900	2	1.3	\pm	0.5
3	2	900 – 1200	900 – ∞	0	0.4	\pm	0.2
3	2	1200 – ∞	200 – 400	1	0.3	\pm	0.1
3	2	1200 – ∞	400 – 600	0	0.7	\pm	0.1
3	2	1200 – ∞	600 – 900	0	0.4	\pm	0.2
3	2	1200 – ∞	900 – ∞	0	0.3	\pm	0.2
3	3	200 – 400	200 – ∞	16	12.1	\pm	2.5
3	3	400 – 600	200 – 400	10	7.9	\pm	1.6
3	3	400 – 600	400 – ∞	2	0.8	\pm	0.2
3	3	600 – ∞	200 – 400	3	0.4	\pm	0.1
3	3	600 – ∞	400 – 600	3	0.3	\pm	0.1
3	3	600 – ∞	600 – ∞	0	0.2	\pm	0.1

Table B.5.: Observed data counts and background expectations from the background-only likelihood fit to the control regions, for the $n_{\text{jet}} = 4$ category. The uncertainties in the background expectations include statistical as well as systematic contributions.

n_{jet}	n_b	H_T [GeV]	\mathcal{H}_T [GeV]	Data	SM		
4	0	400 – 600	200 – 400	4324	4749.1	\pm	621.7
4	0	400 – 600	400 – ∞	437	460.4	\pm	78.3
4	0	600 – 900	200 – 400	751	937.0	\pm	113.5
4	0	600 – 900	400 – 600	484	521.7	\pm	76.4
4	0	600 – 900	600 – ∞	110	103.7	\pm	35.1
4	0	900 – 1200	200 – 400	186	251.2	\pm	36.7
4	0	900 – 1200	400 – 600	111	142.9	\pm	20.7
4	0	900 – 1200	600 – 900	66	71.7	\pm	25.6
4	0	900 – 1200	900 – ∞	13	10.6	\pm	5.8
4	0	1200 – ∞	200 – 400	13	23.8	\pm	6.0
4	0	1200 – ∞	400 – 600	32	43.0	\pm	8.2
4	0	1200 – ∞	600 – 900	28	26.8	\pm	9.9
4	0	1200 – ∞	900 – ∞	15	13.9	\pm	9.4
4	1	400 – 600	200 – 400	1497	1444.4	\pm	191.1
4	1	400 – 600	400 – ∞	109	109.8	\pm	16.5
4	1	600 – 900	200 – 400	184	196.6	\pm	23.6
4	1	600 – 900	400 – 600	106	100.9	\pm	14.0
4	1	600 – 900	600 – ∞	19	17.2	\pm	5.5
4	1	900 – 1200	200 – 400	60	53.8	\pm	7.6
4	1	900 – 1200	400 – 600	19	27.7	\pm	4.1
4	1	900 – 1200	600 – 900	11	12.3	\pm	4.2
4	1	900 – 1200	900 – ∞	1	1.8	\pm	1.0
4	1	1200 – ∞	200 – 400	7	5.2	\pm	1.3
4	1	1200 – ∞	400 – 600	11	10.6	\pm	2.1
4	1	1200 – ∞	600 – 900	7	4.8	\pm	1.7
4	1	1200 – ∞	900 – ∞	4	2.9	\pm	1.8
4	2	400 – 600	200 – 400	524	490.0	\pm	72.7
4	2	400 – 600	400 – ∞	29	24.0	\pm	4.0
4	2	600 – 900	200 – 400	50	39.2	\pm	5.0
4	2	600 – 900	400 – 600	19	19.9	\pm	2.7
4	2	600 – 900	600 – ∞	1	2.4	\pm	0.7
4	2	900 – 1200	200 – 400	10	8.7	\pm	1.2
4	2	900 – 1200	400 – 600	7	4.1	\pm	0.7
4	2	900 – 1200	600 – 900	0	1.7	\pm	0.6
4	2	900 – 1200	900 – ∞	1	0.3	\pm	0.2
4	2	1200 – ∞	200 – 400	1	0.7	\pm	0.2
4	2	1200 – ∞	400 – 600	0	1.5	\pm	0.3
4	2	1200 – ∞	600 – 900	0	0.5	\pm	0.2
4	2	1200 – ∞	900 – ∞	1	0.4	\pm	0.2
4	3	400 – 600	200 – 400	35	36.8	\pm	6.0
4	3	400 – 600	400 – ∞	1	1.6	\pm	0.3
4	3	600 – 900	200 – 400	6	2.5	\pm	0.3
4	3	600 – 900	400 – 600	0	1.2	\pm	0.2
4	3	600 – 900	600 – ∞	0	0.2	\pm	0.0
4	3	900 – ∞	200 – 400	0	0.7	\pm	0.1
4	3	900 – ∞	400 – 600	0	0.4	\pm	0.1
4	3	900 – ∞	600 – 900	0	0.1	\pm	0.0
4	3	900 – ∞	900 – ∞	0	0.0	\pm	0.0

Table B.6.: Observed data counts and background expectations from the background-only likelihood fit to the control regions, for the $n_{\text{jet}} = 5$ category. The uncertainties in the background expectations include statistical as well as systematic contributions.

n_{jet}	n_b	H_T [GeV]	\mathcal{H}_T [GeV]	Data	SM		
5	0	400 – 600	200 – 400	1132	1250.0	±	197.6
5	0	400 – 600	400 – ∞	59	74.0	±	16.6
5	0	600 – 900	200 – 400	435	561.4	±	80.0
5	0	600 – 900	400 – 600	201	197.5	±	35.4
5	0	600 – 900	600 – ∞	17	25.9	±	9.5
5	0	900 – 1200	200 – 400	124	149.9	±	21.2
5	0	900 – 1200	400 – 600	59	68.1	±	10.1
5	0	900 – 1200	600 – ∞	28	30.7	±	11.6
5	0	1200 – ∞	200 – 400	7	18.1	±	4.7
5	0	1200 – ∞	400 – 600	16	23.1	±	4.7
5	0	1200 – ∞	600 – 900	7	13.2	±	5.2
5	0	1200 – ∞	900 – ∞	6	6.2	±	4.3
5	1	400 – 600	200 – 400	591	608.6	±	105.2
5	1	400 – 600	400 – ∞	22	22.0	±	4.5
5	1	600 – 900	200 – 400	198	194.1	±	29.9
5	1	600 – 900	400 – 600	50	55.2	±	9.2
5	1	600 – 900	600 – ∞	11	5.9	±	1.9
5	1	900 – 1200	200 – 400	33	41.0	±	5.8
5	1	900 – 1200	400 – 600	15	16.9	±	2.4
5	1	900 – 1200	600 – ∞	9	7.0	±	2.4
5	1	1200 – ∞	200 – 400	4	4.5	±	1.1
5	1	1200 – ∞	400 – 600	3	6.1	±	1.2
5	1	1200 – ∞	600 – 900	5	2.8	±	1.0
5	1	1200 – ∞	900 – ∞	2	1.6	±	1.1
5	2	400 – 600	200 – 400	284	273.9	±	51.3
5	2	400 – 600	400 – ∞	10	4.8	±	1.0
5	2	600 – 900	200 – 400	63	67.5	±	11.6
5	2	600 – 900	400 – 600	16	16.5	±	2.8
5	2	600 – 900	600 – ∞	0	1.3	±	0.4
5	2	900 – 1200	200 – 400	5	10.5	±	1.6
5	2	900 – 1200	400 – 600	5	3.5	±	0.6
5	2	900 – 1200	600 – ∞	1	1.5	±	0.5
5	2	1200 – ∞	200 – 400	0	1.0	±	0.2
5	2	1200 – ∞	400 – 600	2	1.2	±	0.2
5	2	1200 – ∞	600 – 900	1	0.4	±	0.1
5	2	1200 – ∞	900 – ∞	1	0.3	±	0.2
5	3	400 – 600	200 – 400	25	28.0	±	5.4
5	3	400 – 600	400 – ∞	1	0.3	±	0.1
5	3	600 – 900	200 – 400	7	7.5	±	1.3
5	3	600 – 900	400 – 600	3	1.5	±	0.3
5	3	600 – 900	600 – ∞	0	0.1	±	0.0
5	3	900 – ∞	200 – 400	0	1.1	±	0.2
5	3	900 – ∞	400 – 600	0	0.4	±	0.1
5	3	900 – ∞	600 – ∞	0	0.2	±	0.1
5	≥ 4	400 – ∞	200 – 400	2	1.8	±	0.4
5	≥ 4	400 – ∞	400 – ∞	1	0.1	±	0.0

Table B.7.: Observed data counts and background expectations from the background-only likelihood fit to the control regions, for the $n_{\text{jet}} \geq 6$ category. The uncertainties in the background expectations include statistical as well as systematic contributions.

n_{jet}	n_b	H_T [GeV]	\mathcal{H}_T [GeV]	Data	SM		
≥ 6	0	400 – 600	200 – ∞	164	193.7	\pm	34.3
≥ 6	0	600 – 900	200 – 400	210	278.0	\pm	54.6
≥ 6	0	600 – 900	400 – ∞	56	68.1	\pm	37.3
≥ 6	0	900 – 1200	200 – 400	64	94.4	\pm	29.3
≥ 6	0	900 – 1200	400 – 600	32	34.2	\pm	16.3
≥ 6	0	900 – 1200	600 – ∞	9	12.0	\pm	10.7
≥ 6	0	1200 – ∞	200 – 400	12	18.3	\pm	10.0
≥ 6	0	1200 – ∞	400 – 600	9	16.8	\pm	4.0
≥ 6	0	1200 – ∞	600 – 900	11	8.6	\pm	5.7
≥ 6	0	1200 – ∞	900 – ∞	5	2.8	\pm	3.3
≥ 6	1	400 – 600	200 – ∞	121	135.5	\pm	29.0
≥ 6	1	600 – 900	200 – 400	148	154.3	\pm	32.3
≥ 6	1	600 – 900	400 – ∞	26	25.3	\pm	9.8
≥ 6	1	900 – 1200	200 – 400	42	41.7	\pm	10.3
≥ 6	1	900 – 1200	400 – 600	11	12.1	\pm	4.3
≥ 6	1	900 – 1200	600 – ∞	1	3.3	\pm	2.6
≥ 6	1	1200 – ∞	200 – 400	6	7.4	\pm	3.2
≥ 6	1	1200 – ∞	400 – 600	5	5.9	\pm	1.3
≥ 6	1	1200 – ∞	600 – 900	5	2.6	\pm	1.6
≥ 6	1	1200 – ∞	900 – ∞	0	0.8	\pm	0.9
≥ 6	2	400 – 600	200 – ∞	58	69.5	\pm	16.1
≥ 6	2	600 – 900	200 – 400	85	74.4	\pm	16.9
≥ 6	2	600 – 900	400 – ∞	8	8.5	\pm	2.7
≥ 6	2	900 – 1200	200 – 400	11	17.9	\pm	4.4
≥ 6	2	900 – 1200	400 – 600	3	4.2	\pm	1.2
≥ 6	2	900 – 1200	600 – ∞	0	0.8	\pm	0.6
≥ 6	2	1200 – ∞	200 – 400	0	2.5	\pm	0.9
≥ 6	2	1200 – ∞	400 – 600	0	1.6	\pm	0.4
≥ 6	2	1200 – ∞	600 – 900	2	0.6	\pm	0.3
≥ 6	2	1200 – ∞	900 – ∞	0	0.2	\pm	0.2
≥ 6	3	400 – 600	200 – ∞	14	8.9	\pm	2.2
≥ 6	3	600 – 900	200 – 400	20	11.1	\pm	2.7
≥ 6	3	600 – 900	400 – ∞	3	1.1	\pm	0.4
≥ 6	3	900 – 1200	200 – 400	4	3.0	\pm	0.8
≥ 6	3	900 – 1200	400 – 600	0	0.6	\pm	0.2
≥ 6	3	900 – 1200	600 – ∞	0	0.1	\pm	0.1
≥ 6	3	1200 – ∞	200 – 400	1	0.4	\pm	0.1
≥ 6	3	1200 – ∞	400 – 600	0	0.2	\pm	0.1
≥ 6	3	1200 – ∞	600 – 900	1	0.1	\pm	0.0
≥ 6	3	1200 – ∞	900 – ∞	0	0.0	\pm	0.0
≥ 6	≥ 4	400 – 600	200 – ∞	4	2.5	\pm	0.7

B.2. Results under likelihood fit to signal and control regions

This appendix shows the results of the maximum likelihood fit to the signal and control regions under the background-only hypothesis. The same result under a fit to the control regions only (excluding the signal region) was shown in Sec. 5.4.

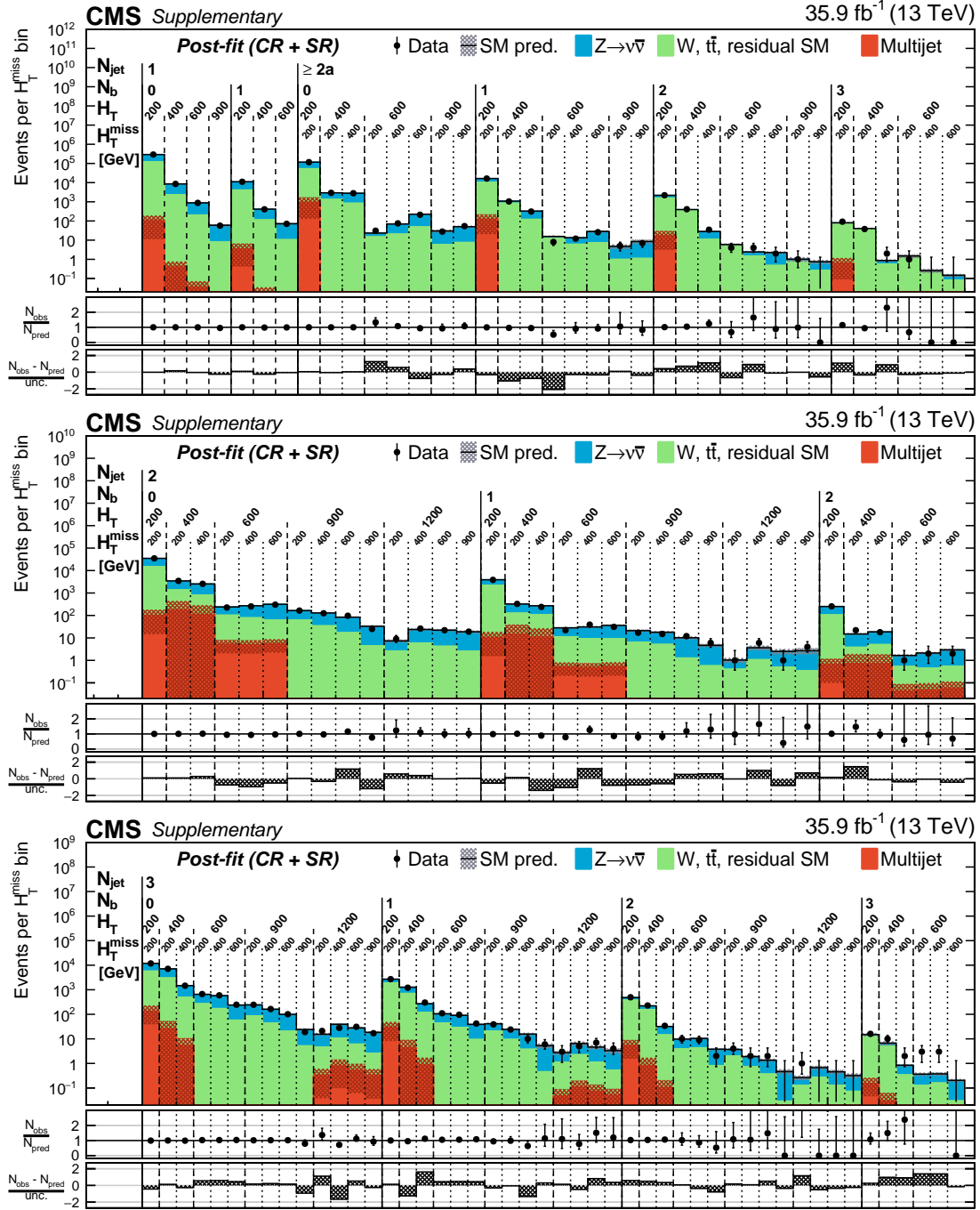


Figure B.1.: Number of events observed (solid markers) and expected number of Z , $W/t\bar{t}$ and QCD background events (histograms, with shaded bands representing the statistical and systematic uncertainties) in every n_b , H_T and H_T^{miss} bin of the jet categories $n_{\text{jet}} = 1, \geq 2a$ (top), $n_{\text{jet}} = 2$ (middle), and $n_{\text{jet}} = 3$ (bottom), as determined from the maximum likelihood fit to the signal and control regions. The centre panel of each sub-figure shows the ratios of the observed and expected counts, while the lower panel shows the corresponding z-score, as defined in the text.

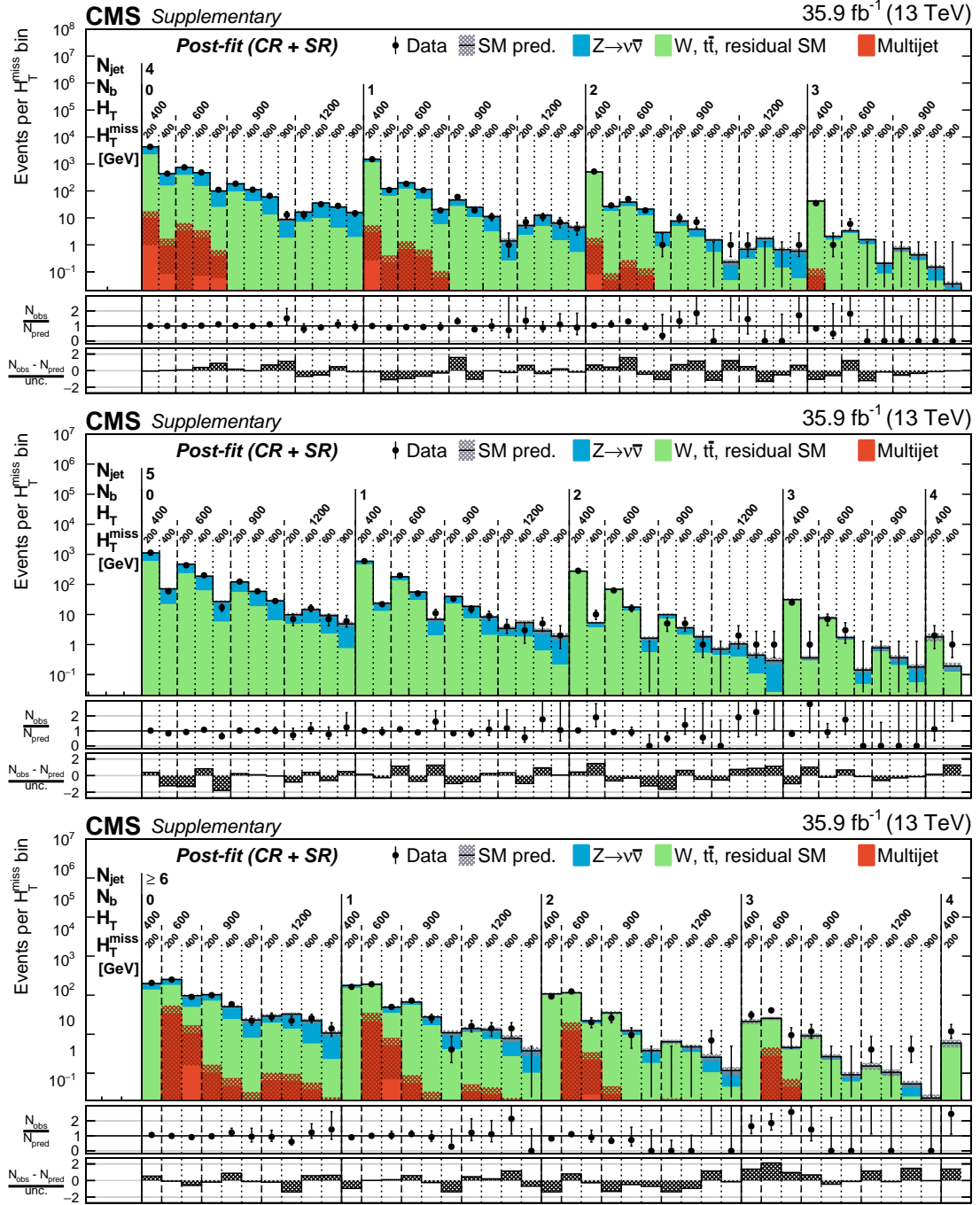


Figure B.2.: Number of events observed (solid markers) and expected number of Z , $W/t\bar{t}$ and QCD background events (histograms, with shaded bands representing the statistical and systematic uncertainties) in every n_b , H_T and H_T bin of the jet categories $n_{\text{jet}} = 4$ (top), $n_{\text{jet}} = 5$ (middle), and $n_{\text{jet}} \geq 6$ (bottom), as determined from the background-only maximum likelihood fit to the signal and control regions. The centre panel of each sub-figure shows the ratios of the observed and expected counts, while the lower panel shows the corresponding z-score, as defined in the text.

B.3. Nuisance parameters

This appendix shows the best fit values (and their uncertainties) of the nuisance parameters that encode the systematic uncertainties on the background estimates under a likelihood fit to the signal and control regions for the background-only hypothesis, as discussed in Sec. 5.4.

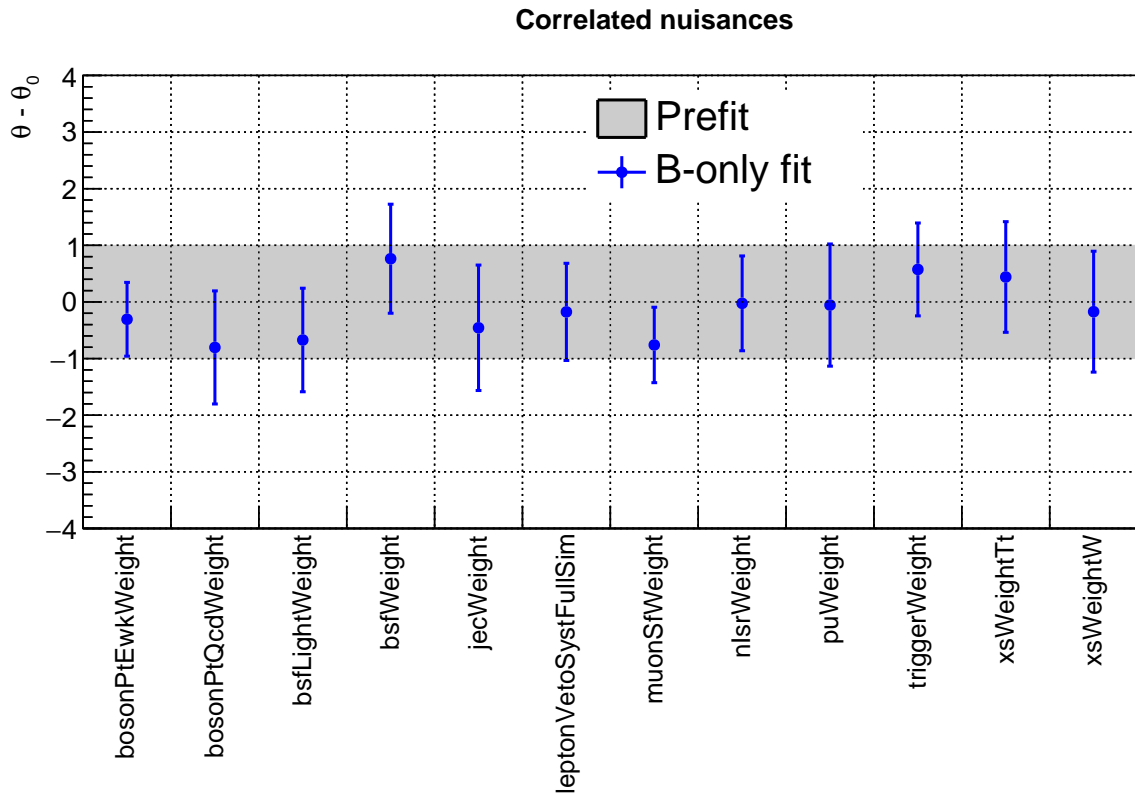


Figure B.3.: Maximum likelihood values of the nuisance parameters related to the systematic uncertainties derived from variations in the simulation correction factors, as determined from the background-only fit to the signal and control regions. From left to right: p_T dependent NLO QCD+EWK corrections; b-tagging efficiency for light and heavy quarks; jet energy scale; lepton identification, isolation and trigger; ISR jets; pileup; signal region triggers; W and $t\bar{t}$ cross sections.

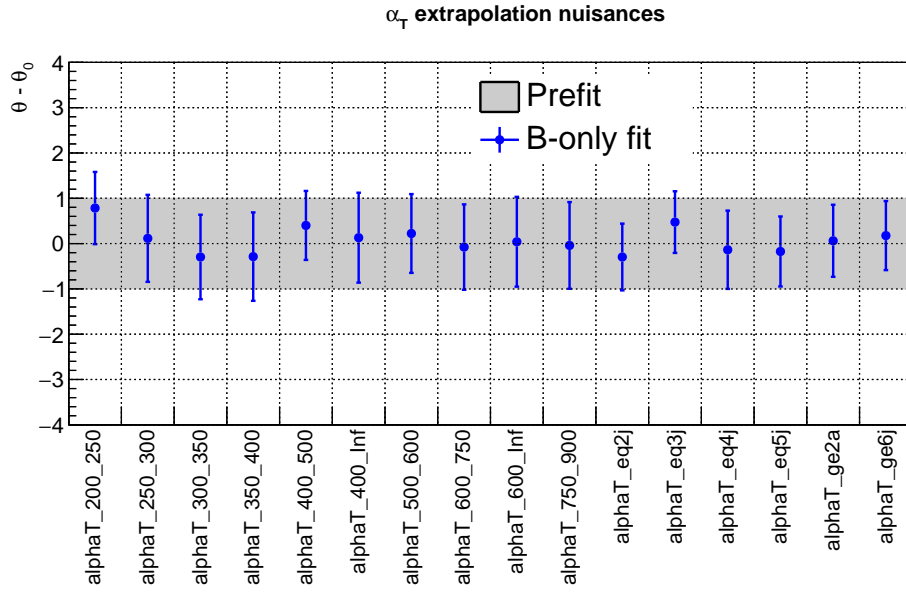


Figure B.4.: Maximum likelihood values of the nuisance parameters related to the systematic uncertainties derived from the α_T closure tests, as determined from the background-only fit to the signal and control regions.

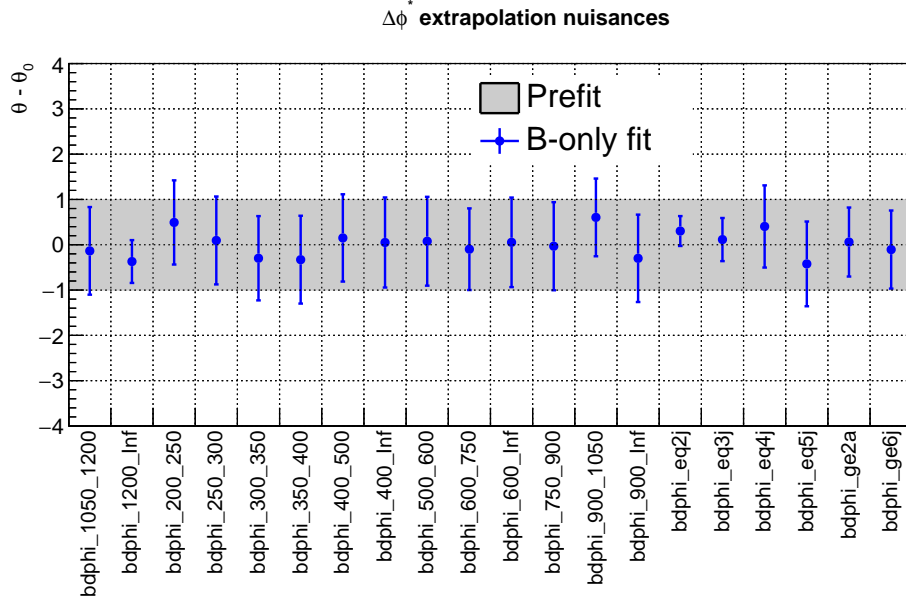


Figure B.5.: Maximum likelihood values of the nuisance parameters related to the systematic uncertainties derived from the $\Delta\phi_{\min}^*$ closure tests, as determined from the background-only fit to the signal and control regions.

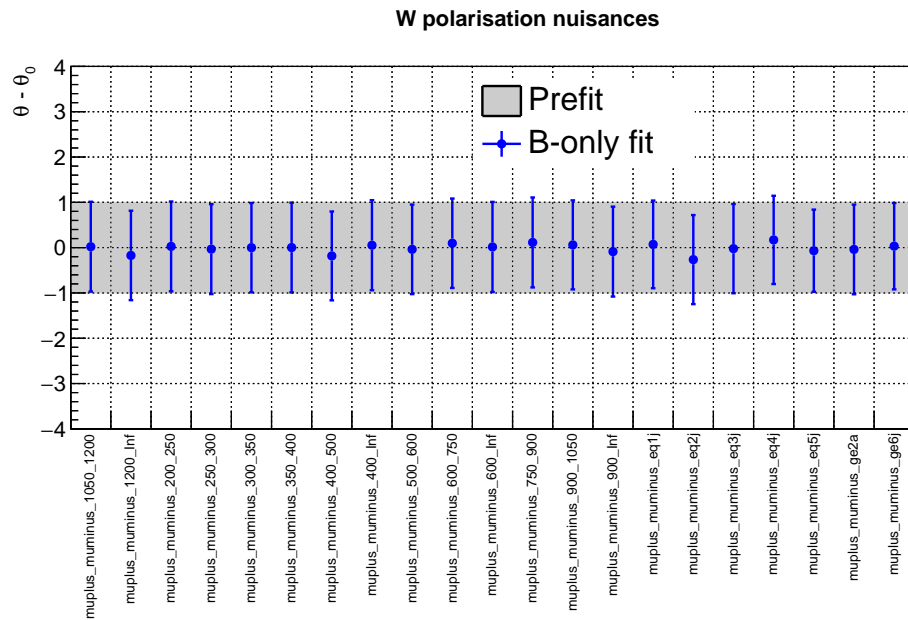


Figure B.6.: Maximum likelihood values of the nuisance parameters related to the systematic uncertainties derived from the W^+/W^- closure tests, as determined from the background-only fit to the signal and control regions.

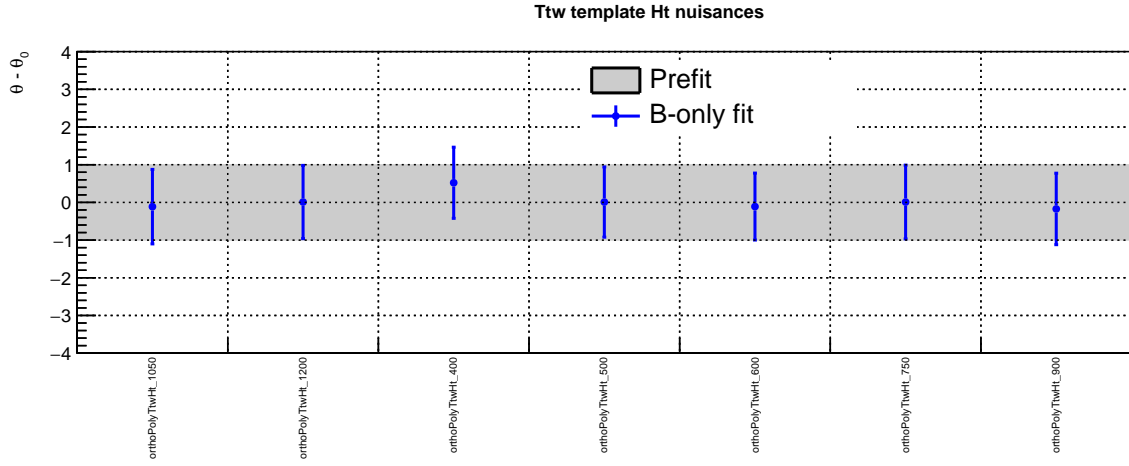


Figure B.7.: Maximum likelihood values of the nuisance parameters related to the H_T -dependent systematic uncertainties on the \mathcal{H}_T shape of the $W/t\bar{t}$ processes, as determined from the background-only fit to the signal and control regions.

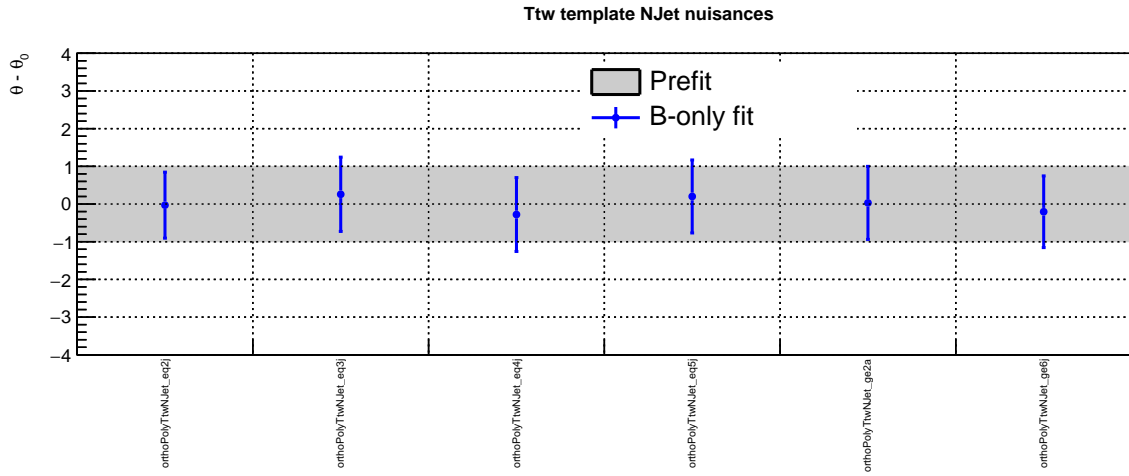


Figure B.8.: Maximum likelihood values of the nuisance parameters related to the n_{jet} -dependent systematic uncertainties on the \mathcal{H}_T shape of the $W/t\bar{t}$ processes, as determined from the background-only fit to the signal and control regions.

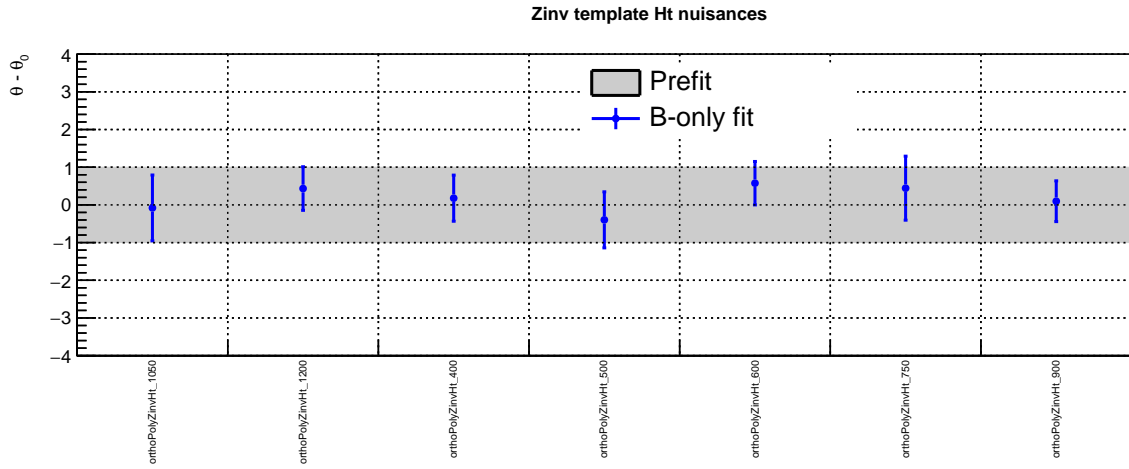


Figure B.9.: Maximum likelihood values of the nuisance parameters related to the H_T -dependent systematic uncertainties on the \cancel{H}_T shape of the $Z(\rightarrow \nu\nu) + \text{jets}$ process, as determined from the background-only fit to the signal and control regions.

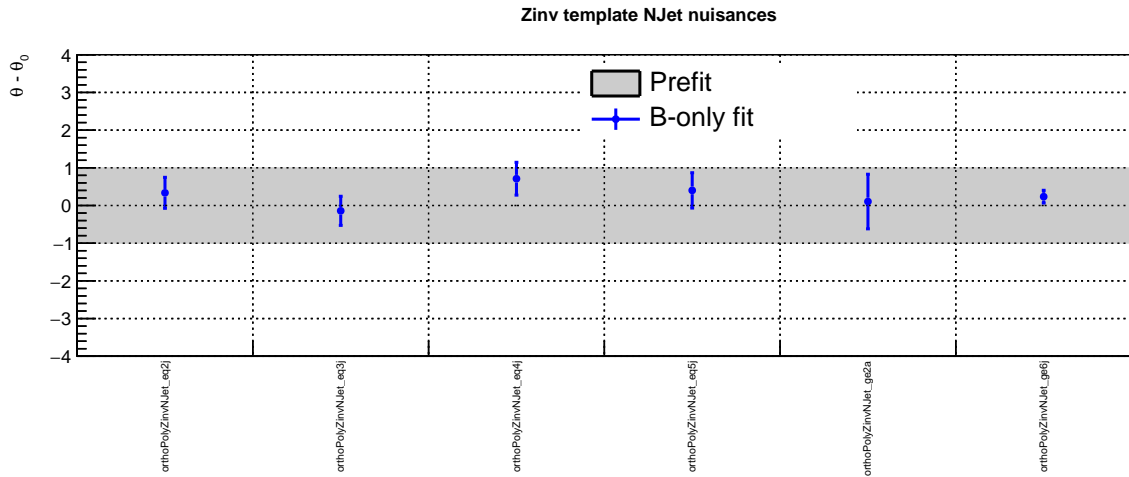


Figure B.10.: Maximum likelihood values of the nuisance parameters related to the n_{jet} -dependent systematic uncertainties on the \cancel{H}_T shape of the $Z(\rightarrow \nu\nu) + \text{jets}$ process, as determined from the background-only fit to the signal and control regions.

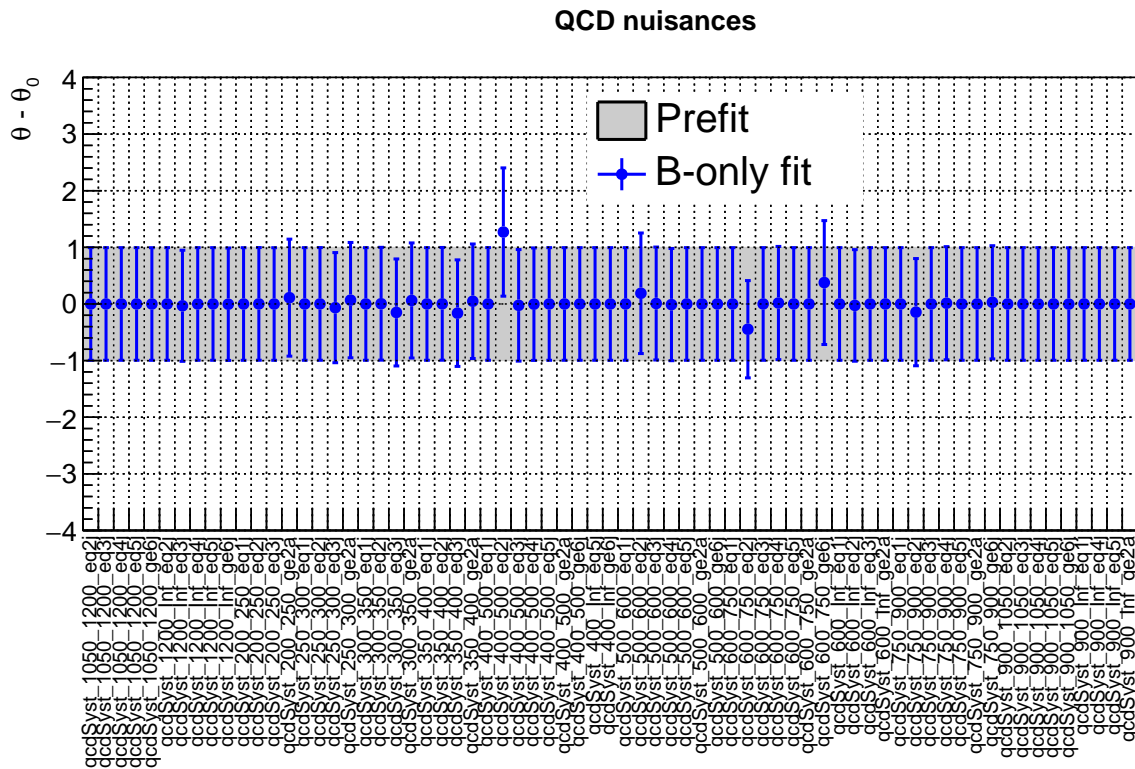


Figure B.11.: Maximum likelihood values of the nuisance parameters related to the systematic uncertainties on the QCD estimation, as determined from the background-only fit to the signal and control regions.

Bibliography

- [1] J. Alwall, M. Herquet, F. Maltoni et al., “MadGraph 5 : Going Beyond”, *JHEP* **06** (2011) 128, [doi:10.1007/JHEP06\(2011\)128](#), [arXiv:1106.0522](#).
- [2] S. Alioli, P. Nason, C. Oleari et al., “A general framework for implementing NLO calculations in shower Monte Carlo programs: the POWHEG BOX”, *JHEP* **06** (2010) 043, [doi:10.1007/JHEP06\(2010\)043](#), [arXiv:1002.2581](#).
- [3] T. Sjöstrand, S. Ask, J. R. Christiansen et al., “An Introduction to PYTHIA 8.2”, *Comput. Phys. Commun.* **191** (2015) 159–177, [doi:10.1016/j.cpc.2015.01.024](#), [arXiv:1410.3012](#).
- [4] GEANT4 Collaboration, “GEANT4: A Simulation toolkit”, *Nucl. Instrum. Meth.* **A506** (2003) 250–303, [doi:10.1016/S0168-9002\(03\)01368-8](#).
- [5] CMS Collaboration, “Search for Supersymmetry at the LHC in Events with Jets and Missing Transverse Energy”, *Phys. Rev. Lett.* **107** (2011) 221804, [doi:10.1103/PhysRevLett.107.221804](#), [arXiv:1109.2352](#).
- [6] CMS Collaboration, “Search for Supersymmetry in pp Collisions at 7 TeV in Events with Jets and Missing Transverse Energy”, *Phys. Lett.* **B698** (2011) 196–218, [doi:10.1016/j.physletb.2011.03.021](#), [arXiv:1101.1628](#).
- [7] CMS Collaboration, “Search for supersymmetry in final states with missing transverse energy and 0, 1, 2, or at least 3 b-quark jets in 7 TeV pp collisions using the variable α_T ”, *JHEP* **01** (2013) 077, [doi:10.1007/JHEP01\(2013\)077](#), [arXiv:1210.8115](#).
- [8] CMS Collaboration, “Search for supersymmetry in hadronic final states with missing transverse energy using the variables α_T and b-quark multiplicity in pp collisions at $\sqrt{s} = 8$ TeV”, *Eur. Phys. J.* **C73** (2013), no. 9, 2568, [doi:10.1140/epjc/s10052-013-2568-6](#), [arXiv:1303.2985](#).

- [9] CMS Collaboration, “A search for new phenomena in pp collisions at $\sqrt{s} = 13$ TeV in final states with missing transverse momentum and at least one jet using the α_T variable”, *Eur. Phys. J. C* **77** (2017) 294, [doi:10.1140/epjc/s10052-017-4787-8](#), [arXiv:1611.00338](#).
- [10] CMS Collaboration, “Performance of missing energy reconstruction in 13 TeV pp collision data using the CMS detector”, Technical Report CMS PAS JME-16-004, CERN, Geneva, (2016).
- [11] L. Randall and D. Tucker-Smith, “Dijet Searches for Supersymmetry at the LHC”, *Phys. Rev. Lett.* **101** (2008) 221803, [doi:10.1103/PhysRevLett.101.221803](#), [arXiv:0806.1049](#).
- [12] CMS Collaboration, “Public CMS Data Quality Information”.
- [13] J. Alwall, R. Frederix, S. Frixione et al., “The automated computation of tree-level and next-to-leading order differential cross sections, and their matching to parton shower simulations”, *JHEP* **07** (2014) 079, [doi:10.1007/JHEP07\(2014\)079](#), [arXiv:1405.0301](#).
- [14] CMS Collaboration, “The fast simulation of the CMS detector at LHC”, *J. Phys. Conf. Ser.* **331** (2011) 032049, [doi:10.1088/1742-6596/331/3/032049](#).
- [15] A. C. Kraan, “Interactions of heavy stable hadronizing particles”, *Eur. Phys. J. C* **37** (2004) 91, [doi:10.1140/epjc/s2004-01946-6](#), [arXiv:hep-ex/0404001](#).
- [16] R. Mackeprang and A. Rizzi, “Interactions of Coloured Heavy Stable Particles in Matter”, *Eur. Phys. J. C* **50** (2007) 353, [doi:10.1140/epjc/s10052-007-0252-4](#), [arXiv:hep-ph/0612161](#).
- [17] ATLAS Collaboration, “Measurement of the Inelastic Proton-Proton Cross Section at $\sqrt{s} = 13$ TeV with the ATLAS Detector at the LHC”, *Phys. Rev. Lett.* **117** (2016) 182002, [doi:10.1103/PhysRevLett.117.182002](#), [arXiv:1606.02625](#).
- [18] CMS Collaboration, “Identification of b quark jets at the CMS Experiment in the LHC Run 2”, Technical Report CMS-PAS-BTV-15-001, CERN, Geneva, (2016).
- [19] CMS Collaboration, “Generic Tag and Probe Tool for Measuring Efficiency at CMS with Early Data”, Technical Report CMS AN-2009/111, CERN, (2009).

- [20] CMS Collaboration, “Search for new physics in final states with an energetic jet or a hadronically decaying W or Z boson and transverse momentum imbalance at $\sqrt{s} = 13$ TeV”, [arXiv:1712.02345](#).
- [21] Z. Bern et al., “Left-Handed W Bosons at the LHC”, *Phys. Rev. D* **84** (2011) 034008, [doi:10.1103/PhysRevD.84.034008](#), [arXiv:1103.5445](#).
- [22] CMS Collaboration, “CMS Luminosity Measurement for the 2015 Data Taking Period”, CMS Physics Analysis Summary CMS-PAS-LUM-15-001, CERN, (2016).
- [23] J. S. Conway, “Incorporating Nuisance Parameters in Likelihoods for Multisource Spectra”, [arXiv:1103.0354](#).
- [24] ATLAS and CMS Collaborations, and LHC Higgs Combination Group, “Procedure for the LHC Higgs boson search combination in Summer 2011”, Technical Report CMS-NOTE-2011-005 ATL-PHYS-PUB-2011-11, CERN, Geneva, (2011).
- [25] T. Junk, “Confidence level computation for combining searches with small statistics”, *Nucl. Instr. Meth. A* **434** (1999) 435, [doi:10.1016/S0168-9002\(99\)00498-2](#), [arXiv:hep-ex/9902006](#).
- [26] A. L. Read, “Presentation of search results: the CL_s technique”, *J. Phys. G* **28** (2002) 2693, [doi:10.1088/0954-3899/28/10/313](#).
- [27] G. Cowan, K. Cranmer, E. Gross et al., “Asymptotic formulae for likelihood-based tests of new physics”, *Eur. Phys. J. C* **71** (2011) 1554, [doi:10.1140/epjc/s10052-011-1554-0](#), [arXiv:1007.1727](#).

List of figures

4.1. The leading jet's charged hadron energy fraction (left) and ϕ direction before (centre) and after (right) applying a requirement of $f_{\text{CH}} > 0.1$. The large excess in data at f_{CH} values close to zero and $\phi = 0$ and π is consistent with beam halo effects, and is effectively suppressed by the f_{CH} requirement.	21
4.2. The distribution of the α_{T} variable in data and simulation for events satisfying the signal region selections (Sec. 4.5) except the α_{T} requirement. The ability of the variable to effectively discriminate between QCD processes and processes with genuine missing energy is evidenced by the sharp edge at 0.5.	26
4.3. The distribution of the $\Delta\phi_{\text{min}}^*$ variable in data and simulation for events satisfying the signal region selections (Sec. 4.5) except the $\Delta\phi_{\text{min}}^*$ requirement. The ability of the variable to effectively discriminate between QCD processes and processes with genuine missing energy is evidenced by the cluster of QCD events close to 0, while processes with genuine \cancel{E}_{T} take on larger values up to π radians.	28
4.4. The distribution of the $\cancel{H}_{\text{T}}/\cancel{E}_{\text{T}}$ ratio in data and simulation for events satisfying the signal region selections (Sec. 4.5) except the $\cancel{H}_{\text{T}}/\cancel{E}_{\text{T}}$ requirement. The ability of the variable to effectively discriminate between QCD processes and processes with genuine missing energy is evidenced by the population of QCD events above 1.25, while processes with genuine \cancel{E}_{T} have values more consistent with unity. [FIXME: remove ratio plot and fix axis label? Update to 36fb]	29
4.5. Efficiency of the HL trigger in the signal region as a function of offline \cancel{H}_{T} and H_{T} , measured in a data sample collected by a single electron (left) and single muon (right) trigger.	42

- 4.6. Cumulative integrated luminosity of pp collisions at $\sqrt{s} = 13$ TeV delivered by the LHC, recorded by CMS, and certified as good for physics analysis per day during the year 2016 [12]. 43
- 4.7. Distribution of the number of pileup interactions in the Monte Carlo (MC) simulation and in data. The ratio of the two is used to derive correction factors that are used to weight the simulated events. The corrected simulated distribution is also shown. 46
- 4.8. Result of the tag-and-probe dimuon invariant mass fitting procedure to passing (left) and failing (right) probes for an example isolation efficiency measurement in data for muons with $50 < p_T < 60$ GeV. The blue (red) curves are the fitted signal (background) distributions. The fitted efficiency in this example is 96.0%. 50
- 4.9. The data-to-simulation ratio of event counts as a function of \cancel{H}_T for two example $(n_{\text{jet}}, n_b, H_T)$ categories, along with the fit of a linear (and constant) function. 58
- 4.10. The distribution of the z-scores of the linear parameter fitted to the \cancel{H}_T distributions for all $(n_{\text{jet}}, n_b, H_T)$ categories in both the $\mu + \text{jets}$ and $\mu\mu + \text{jets}$ control regions. A fitted Gaussian distribution is overlaid. 59
- 4.11. The estimated number of QCD events in each (n_{jet}, H_T) bin of the signal region (top), and the corresponding ratio of expected QCD and electroweak events (bottom). 61
- 4.12. The ratio of the $T(\mu \rightarrow W/t\bar{t})$ (top) and $T(\mu\mu \rightarrow Z)$ (bottom) transfer factors in each $(n_{\text{jet}}, n_b, H_T)$ bin when varying the pileup correction factors by $+1\sigma$ (left) and -1σ (right) with respect to their nominal values. 63
- 4.13. Closure tests relating to extrapolations in α_T (top), $\Delta\phi_{\text{min}}^*$ (middle), and W boson polarisation (bottom), as a function of H_T (left) and n_{jet} (right). The level of closure obtained via a maximum likelihood method is indicated by the open circles. The blue lines represent the resulting systematic uncertainties that are assigned to the relevant transfer factors. A linear fit is also shown. 69

- 5.1. Expected signal events for Split SUSY simplified models with a range of values of $(c\tau, m_{\tilde{g}}, m_{\tilde{\chi}_1^0})$, overlaid on the expected standard model background counts, using an aggregated binning scheme. 73
- 5.2. Efficiency of the b-tagging algorithm for displaced jets originating from long-lived gluinos, compared to standard model bottom and light quarks, for jets with $100 < p_T < 140$ and $0 < |\eta| < 0.5$ 75
- 5.3. Number of events observed (solid markers) and expected number of Z, W/t \bar{t} and QCD background events (histograms, with shaded bands representing the statistical and systematic uncertainties) in every n_b , H_T and \cancel{H}_T bin of the jet categories $n_{\text{jet}} = 1, \geq 2a$ (top), $n_{\text{jet}} = 2$ (middle), and $n_{\text{jet}} = 3$ (bottom), as determined from the maximum likelihood fit to the control regions. The centre panel of each sub-figure shows the ratios of the observed and expected counts, while the lower panel shows the corresponding z-score, as defined in the text. 80
- 5.4. Number of events observed (solid markers) and expected number of Z, W/t \bar{t} and QCD background events (histograms, with shaded bands representing the statistical and systematic uncertainties) in every n_b , H_T and \cancel{H}_T bin of the jet categories $n_{\text{jet}} = 4$ (top), $n_{\text{jet}} = 5$ (middle), and $n_{\text{jet}} \geq 6$ (bottom), as determined from the background-only maximum likelihood fit to the control regions. The centre panel of each sub-figure shows the ratios of the observed and expected counts, while the lower panel shows the corresponding z-score, as defined in the text. 81
- 5.5. Histograms of the ratios of the observed and expected event counts (left) and corresponding z-scores (right), as defined in the text, for all $(n_{\text{jet}}, n_b, H_T)$ bins, as determined from the background-only maximum likelihood fit to the control regions. 82

- 5.6. Observed upper limit in cross section at 95% confidence level (indicated by the colour scale) as a function of the \tilde{g} and $\tilde{\chi}_1^0$ masses for the Split SUSY simplified models. Each subfigure represents a different gluino lifetime. The thick (thin) black line indicates the observed excluded region assuming the nominal ($\pm 1\sigma$ in theoretical cross section uncertainty) production cross section. The red dashed (dashed and dotted) represents the median ($\pm 1\sigma$ and $\pm 2\sigma$ in experimental uncertainty) expected excluded region. 86
- 5.7. Observed upper limit in cross section at 95% confidence level (indicated by the colour scale) as a function of the \tilde{g} and $\tilde{\chi}_1^0$ masses for the Split SUSY simplified models. Each subfigure represents a different gluino lifetime. The thick (thin) black line indicates the observed excluded region assuming the nominal ($\pm 1\sigma$ in theoretical cross section uncertainty) production cross section. The red dashed (dashed and dotted) represents the median ($\pm 1\sigma$ and $\pm 2\sigma$ in experimental uncertainty) expected excluded region. 87
- 5.8. Observed upper limit in cross section at 95% confidence level (indicated by the colour scale) as a function of the \tilde{g} and $\tilde{\chi}_1^0$ masses for the Split SUSY simplified models. Each subfigure represents a different gluino lifetime. The thick (thin) black line indicates the observed excluded region assuming the nominal ($\pm 1\sigma$ in theoretical cross section uncertainty) production cross section. The red dashed (dashed and dotted) represents the median ($\pm 1\sigma$ and $\pm 2\sigma$ in experimental uncertainty) expected excluded region. 88
- 5.9. Summary of observed and expected excluded regions at 95% confidence level as a function of the \tilde{g} and $\tilde{\chi}_1^0$ masses for various gluino lifetimes for the Split SUSY simplified models. 89
- A.1. The ratio of the $T(\mu \rightarrow W/t\bar{t})$ (top) and $T(\mu\mu \rightarrow Z)$ (bottom) transfer factors in each (n_{jet}, n_b, H_T) bin when varying the pileup correction factors by $+1\sigma$ (left) and -1σ (right) with respect to their nominal values. 92

A.2. The ratio of the $T(\mu \rightarrow W/t\bar{t})$ (top) and $T(\mu\mu \rightarrow Z)$ (bottom) transfer factors in each $(n_{\text{jet}}, n_b, H_T)$ bin when varying the jet energy correction factors by $+1\sigma$ (left) and -1σ (right) with respect to their nominal values.	93
A.3. The ratio of the $T(\mu \rightarrow W/t\bar{t})$ (top) and $T(\mu\mu \rightarrow Z)$ (bottom) transfer factors in each $(n_{\text{jet}}, n_b, H_T)$ bin when varying the b-tagging correction factors for bottom and charm quarks by $+1\sigma$ (left) and -1σ (right) with respect to their nominal values.	94
A.4. The ratio of the $T(\mu \rightarrow W/t\bar{t})$ (top) and $T(\mu\mu \rightarrow Z)$ (bottom) transfer factors in each $(n_{\text{jet}}, n_b, H_T)$ bin when varying the b-tagging correction factors for light partons (u, d, s, gluon) by $+1\sigma$ (left) and -1σ (right) with respect to their nominal values.	95
A.5. The ratio of the $T(\mu \rightarrow W/t\bar{t})$ (top) and $T(\mu\mu \rightarrow Z)$ (bottom) transfer factors in each $(n_{\text{jet}}, n_b, H_T)$ bin when varying the trigger correction factors by $+1\sigma$ (left) and -1σ (right) with respect to their nominal values.	96
A.6. The ratio of the $T(\mu \rightarrow W/t\bar{t})$ (top) and $T(\mu\mu \rightarrow Z)$ (bottom) transfer factors in each $(n_{\text{jet}}, n_b, H_T)$ bin when varying the boson p_T dependent NLO correction factors by $+1\sigma$ (left) and -1σ (right) with respect to their nominal values.	97
A.7. The ratio of the $T(\mu \rightarrow W/t\bar{t})$ (top) and $T(\mu\mu \rightarrow Z)$ (bottom) transfer factors in each $(n_{\text{jet}}, n_b, H_T)$ bin when varying the $t\bar{t}$ ISR correction factors by $+1\sigma$ (left) and -1σ (right) with respect to their nominal values.	98
A.8. The ratio of the $T(\mu \rightarrow W/t\bar{t})$ (top) and $T(\mu\mu \rightarrow Z)$ (bottom) transfer factors in each $(n_{\text{jet}}, n_b, H_T)$ bin when varying the W cross section correction factors by $+1\sigma$ (left) and -1σ (right) with respect to their nominal values.	99
A.9. The ratio of the $T(\mu \rightarrow W/t\bar{t})$ (top) and $T(\mu\mu \rightarrow Z)$ (bottom) transfer factors in each $(n_{\text{jet}}, n_b, H_T)$ bin when varying the $t\bar{t}$ cross section correction factors by $+1\sigma$ (left) and -1σ (right) with respect to their nominal values.	100

- B.1. Number of events observed (solid markers) and expected number of Z, W/ $t\bar{t}$ and QCD background events (histograms, with shaded bands representing the statistical and systematic uncertainties) in every n_b , H_T and \cancel{H}_T bin of the jet categories $n_{\text{jet}} = 1, \geq 2a$ (top), $n_{\text{jet}} = 2$ (middle), and $n_{\text{jet}} = 3$ (bottom), as determined from the maximum likelihood fit to the signal and control regions. The centre panel of each sub-figure shows the ratios of the observed and expected counts, while the lower panel shows the corresponding z-score, as defined in the text. 110
- B.2. Number of events observed (solid markers) and expected number of Z, W/ $t\bar{t}$ and QCD background events (histograms, with shaded bands representing the statistical and systematic uncertainties) in every n_b , H_T and \cancel{H}_T bin of the jet categories $n_{\text{jet}} = 4$ (top), $n_{\text{jet}} = 5$ (middle), and $n_{\text{jet}} \geq 6$ (bottom), as determined from the background-only maximum likelihood fit to the signal and control regions. The centre panel of each sub-figure shows the ratios of the observed and expected counts, while the lower panel shows the corresponding z-score, as defined in the text. 111
- B.3. Maximum likelihood values of the nuisance parameters related to the systematic uncertainties derived from variations in the simulation correction factors, as determined from the background-only fit to the signal and control regions. From left to right: p_T dependent NLO QCD+EWK corrections; b-tagging efficiency for light and heavy quarks; jet energy scale; lepton identification, isolation and trigger; ISR jets; pileup; signal region triggers; W and $t\bar{t}$ cross sections. . . . 112
- B.4. Maximum likelihood values of the nuisance parameters related to the systematic uncertainties derived from the α_T closure tests, as determined from the background-only fit to the signal and control regions. 113
- B.5. Maximum likelihood values of the nuisance parameters related to the systematic uncertainties derived from the $\Delta\phi_{\text{min}}^*$ closure tests, as determined from the background-only fit to the signal and control regions. 113

B.6. Maximum likelihood values of the nuisance parameters related to the systematic uncertainties derived from the W^+/W^- closure tests, as determined from the background-only fit to the signal and control regions.	114
B.7. Maximum likelihood values of the nuisance parameters related to the H_T -dependent systematic uncertainties on the \cancel{H}_T shape of the $W/t\bar{t}$ processes, as determined from the background-only fit to the signal and control regions.	115
B.8. Maximum likelihood values of the nuisance parameters related to the n_{jet} -dependent systematic uncertainties on the \cancel{H}_T shape of the $W/t\bar{t}$ processes, as determined from the background-only fit to the signal and control regions.	115
B.9. Maximum likelihood values of the nuisance parameters related to the H_T -dependent systematic uncertainties on the \cancel{H}_T shape of the $Z(\rightarrow \nu\nu) + \text{jets}$ process, as determined from the background-only fit to the signal and control regions.	116
B.10. Maximum likelihood values of the nuisance parameters related to the n_{jet} -dependent systematic uncertainties on the \cancel{H}_T shape of the $Z(\rightarrow \nu\nu) + \text{jets}$ process, as determined from the background-only fit to the signal and control regions.	116
B.11. Maximum likelihood values of the nuisance parameters related to the systematic uncertainties on the QCD estimation, as determined from the background-only fit to the signal and control regions.	117

List of tables

4.1. The p_T and η thresholds for physics objects that are used to either select events or veto them.	16
4.2. Quality requirements imposed on the constituents of jets.	17
4.3. Summary of selections as part of the definition of the signal and control regions.	30
4.4. The α_T thresholds as a function of H_T for events containing at least two jets. No requirement is made on events containing only one jet.	31
4.5. The definitions of the sideband regions employed in the estimation of the QCD background.	33
4.6. Summary of all bins in the signal region. The listed numbers correspond to the lower boundaries of the \cancel{H}_T bins in each $(n_{\text{jet}}, n_b, H_T)$ bin; the final number in the list is always an open bin. A single-element list is equivalent to no binning in \cancel{H}_T . A dash means a particular $(n_{\text{jet}}, n_b, H_T)$ bin is not used, and so the previous H_T bin (if applicable) is an open bin. The muon control regions are binned identically, except that they are not binned in \cancel{H}_T , and the largest n_b category in the $\mu\mu + \text{jets}$ control region is ≥ 1	35

4.7. List of L1 and HL triggers utilised in this search, grouped by family, indicating in parentheses their varying thresholds throughout the 2016 LHC run. All quantities related to energy and momentum are quoted in GeV units. The muon trigger is employed in the muon control regions, while all other triggers listed are employed in the signal region and hadronic control regions. The H_T - α_T triggers also have a minimum requirement of 90 GeV on the average p_T of the two leading jets, which did not change throughout run. Also provided is the fraction of the run for which a given trigger version was the lowest-threshold unprescaled trigger.	39
4.8. Cross section correction factors for the three dominant standard model background processes, along with an indication of the most constraining sideband region for each process.	53
4.9. Summary of systematic uncertainties on the $T(\mu \rightarrow W/t\bar{t})$ and $T(\mu\mu \rightarrow Z)$ transfer factors, derived from variations of the data-to-simulation correction factors (Sec. 4.12.1) and data-driven closure tests (Sec. 4.12.2). The quoted ranges correspond to the $\pm 1\sigma$ quantiles of the transfer factor changes across all $(n_{\text{jet}}, n_b, H_T)$ bins.	62
5.1. Summary of uncertainties (%) on the simplified long-lived gluino models for various values of $(m_{\tilde{g}}, m_{\tilde{\chi}_1^0})$ [GeV]. The quoted ranges correspond to the $\pm 1\sigma$ quantiles of the yield changes across all $(n_{\text{jet}}, n_b, H_T, \cancel{H}_T)$ bins.	74
B.1. Observed data counts and background expectations from the background-only likelihood fit to the control regions, for the $n_{\text{jet}} = 1$ category. The uncertainties in the background expectations include statistical as well as systematic contributions.	102
B.2. Observed data counts and background expectations from the background-only likelihood fit to the control regions, for the $n_{\text{jet}} \geq 2a$ category. The uncertainties in the background expectations include statistical as well as systematic contributions.	103

B.3. Observed data counts and background expectations from the background-only likelihood fit to the control regions, for the $n_{\text{jet}} = 2$ category. The uncertainties in the background expectations include statistical as well as systematic contributions.	104
B.4. Observed data counts and background expectations from the background-only likelihood fit to the control regions, for the $n_{\text{jet}} = 3$ category. The uncertainties in the background expectations include statistical as well as systematic contributions.	105
B.5. Observed data counts and background expectations from the background-only likelihood fit to the control regions, for the $n_{\text{jet}} = 4$ category. The uncertainties in the background expectations include statistical as well as systematic contributions.	106
B.6. Observed data counts and background expectations from the background-only likelihood fit to the control regions, for the $n_{\text{jet}} = 5$ category. The uncertainties in the background expectations include statistical as well as systematic contributions.	107
B.7. Observed data counts and background expectations from the background-only likelihood fit to the control regions, for the $n_{\text{jet}} \geq 6$ category. The uncertainties in the background expectations include statistical as well as systematic contributions.	108